MAGNETIC FIELD AMPLIFICATION BY FLUID DYNAMOS
DYNAMO MODELS OF THE SOLAR CYCLE

About these Lecture Notes

These lecture notes are meant to describe, in more detail and with full references to the technical literature, the material covered in my two Lectures presented (unfortunately remotely) at the Università dell'Aquila's International School of Space Science, as part of the April 2022 program entitled "The different spatio-temporal scales of solar magnetism".

My lectures aim to cover the physical processes of magnetic field amplification by dynamo action in electrically conducting fluids, and dynamo models of the solar cycle. These accompanying notes are **not** meant as a comprehensive coverage of these topics, but rather as a form of "record" of my two lectures.

I have assembled these notes from three primary sources: (1) Lecture notes written for the 39$^{\text{th}}$ Saas Fee Advanced Course, held in Les Diablerets, Switzerland, and published in book form by Springer on behalf of the Swiss Astronomical Society (Charbonneau, 2013); (2) The 2020 version of my review article *Solar cycle models*, published in *Living Reviews in Solar Physics* (Charbonneau, 2020)); (3) Drafts of three chapters written for a book currently in preparation, tentatively entitled *Our Variable Sun* and to be published by Cambridge University Press, co-authored with my colleagues Ilya Usoskin and Gennady Kovaltsov (both at University of Oulu, Finland), Sami Solanki and Natalia Krivova (both at the Max-Planck-Institut für Sonnensystemforschung in Göttingen, Germany).

Animations presented during my Lectures are available for download here:

`www.astro.umontreal.ca/~paulchar/ISSS22/ISSS.html`

Finally, I wish to express my thanks to Profs. Francesca Zuccarello and Luis Bellot Rubio for their invitation to contribute to this exciting program.

Paul Charbonneau
Département de Physique
Université de Montréal, Canada
6 April 2022

Table of Content

Chapter 1

Magnetic field amplification by fluid dynamos

Astrophysical dynamo theory is an immense topic, which is the subject of numerous recent and not-so-recent monographs (e.g., Moffatt, 1978; Parker, 1979; Krause and Rädler, 1980; Rüdiger and Hollerbach, 2004; Charbonneau, 2013; Moffatt and Dormy, 2019), as well as a number of extensive review articles (e.g. Ossendrijver, 2003; Brandenburg and Subramanian, 2005; Charbonneau, 2014). This first lecture aims at establishing the basic physical principles underlying magnetic field amplification by (astrophysical) fluid dynamos. The design and behavior of specific solar cycle models will be dealt with in my second Lecture.

1.1 Magnetohydrodynamics

At the microscopic level, solar plasma is made up of an electrically neutral mixture of electrically-charged constituents: electrons, Hydrogen and Helium nucleii, and small quantities of heavier ions. In the solar interior up to the photosphere, the number densities and thermal speeds are high enough for collision frequencies to largely exceed any other relevant plasma frequencies. Under such physical conditions, at the macroscopic level the interaction of fluid flows and magnetic fields is well-described by the magnetohydrodynamical approximation.

MHD approximation

What follows is only a brief introduction to magnetohydrodynamics (hereafter MHD) in the solar context. More detailed presentations can be found in a number of textbooks, e.g., Choudhuri (1998), Davidson (2001), Goedbloed and Poedts (2004), and Priest (2014).

1.1.1 The MHD induction equation

Our starting point towards magnetohydrodynamics is Maxwell's equations, and more specifically Faraday's Law:

Faraday's Law

$$\frac{\partial \mathbf{B}}{\partial t} = -\nabla \times \mathbf{E} \ , \tag{1.1}$$

where $\mathbf{E}$ [$\mathrm{V\,m^{-1}}$] and $\mathbf{B}$ [T] are the electric and magnetic fields, respectively (SI units are used throughout; $1\,\mathrm{T} \equiv 10^4$ Gauss). In a collisionally-dominated plasma flowing at speed $\mathbf{u}$ at the macroscopic scale, Ohm's Law is expected to hold in a reference frame co-moving with the flow:

Ohm's Law

$$\mathbf{J}' = \sigma \mathbf{E}' \ , \tag{1.2}$$

where $\mathbf{J}$ [$\mathrm{A\,m^{-2}}$] is the electric current density, primed quantities denote measures made in the comoving frame, and σ [siemens per meter, $\equiv \mathrm{Ohm^{-1}\,m^{-1}}$, $\equiv \mathrm{C^2 s^{-1} m^{-3} kg^{-1}}$] is the electrical conductivity, typically quite large for solar plasma. For a non-relativistic fluid flow $\mathbf{u}$, Lorentz transformation to the rest frame reduces to $\mathbf{J}' = \mathbf{J}$ and $\mathbf{E}' = \mathbf{E} + \mathbf{u} \times \mathbf{B}$. Substituting in Ohm's Law then yields an expression for the rest frame electric field:

Generalized Ohm's Law

$$\mathbf{E} = \mathbf{J}/\sigma - \mathbf{u} \times \mathbf{B} \ . \tag{1.3}$$

Excluding externally imposed rapid variations of $\mathbf{E}$, Ampère's law holds in its pre-Maxwellian form:

Ampère's Law

$$\nabla \times \mathbf{B} = \mu_0 \mathbf{J} \ , \tag{1.4}$$

where $\mu_0 = 4\pi \times 10^{-7}\,\mathrm{N\,A^{-2}}$ is the magnetic permeability. Using this expression to substitute for $\mathbf{J}$ in Eq. (1.3), and inserting the resulting expression for $\mathbf{E}$ on the RHS of Eq. (1.1) leads to the *MHD induction equation*:

$$\frac{\partial \mathbf{B}}{\partial t} = \nabla \times (\mathbf{u} \times \mathbf{B} - \eta \nabla \times \mathbf{B}) \ , \tag{1.5}$$

where $\eta = (\mu_0 \sigma)^{-1}$ [$\mathrm{m^2\,s^{-1}}$] is the *magnetic diffusivity*. The first term on the RHS expresses induction by the flow of electrically charged constituents across the magnetic field, and the second Ohmic dissipation of the current systems supporting that same magnetic field, as per Eq. (1.4). The MHD induction equation is the mathematical and physical cornerstone of magnetic field generation in electrically conducting fluids, i.e., *fluid dynamos*.

Magnetic diffusivity

Fluid dynamo

Because the magnetic field is solenoidal (i.e., $\nabla \cdot \mathbf{B} = 0$), it can be expressed in terms of a magnetic vector potential $\mathbf{A}$ via $\mathbf{B} = \nabla \times \mathbf{A}$. Substituting into the MHD induction equation (1.5), the later can be "uncurled" into:

Magnetic vector potential

Poloidal/toroidal

$$\frac{\partial \mathbf{A}}{\partial t} = \mathbf{u} \times (\nabla \times \mathbf{A}) - \eta \nabla^2 \mathbf{A} \ , \tag{1.6}$$

under the Coulomb gauge $\nabla \cdot \mathbf{A} = 0$. This is a useful alternate formulation of the induction equation, which is often used in the dynamo context. In particular, working in spherical polar coordinates (r, θ, ϕ), it will prove convenient to express an axisymmetric ($\partial/\partial\phi = 0$) magnetic field as the sum of poloidal and toroidal components as the following mixed representation:

$$\mathbf{B} = \underbrace{\nabla \times (A_\phi \hat{\mathbf{e}}_\phi)}_{\text{poloidal}} + \underbrace{B_\phi \hat{\mathbf{e}}_\phi)}_{\text{toroidal}} \tag{1.7}$$

with the field's symmetry axis coinciding with the polar axis of the coordinate system.

The electrical current density required to sustain the sun's large-scale magnetic field is actually quite low. Consider a dipole of (surface) strength $B = 10^{-3}\,\mathrm{T}$ ($\equiv 10\,\mathrm{G}$) imbedded in a sun-like sphere of radius $R = 7 \times 10^8\,\mathrm{m}$. Dimensional analysis of Ampère's Law (1.4) yields

$$J \sim \frac{B}{\mu_0 R} \simeq 10^{-5}\,\mathrm{A\ m^{-2}}\ ; \tag{1.8}$$

In the solar interior this current density is generated by a net drift speed $\mathbf{v}$ between electrons and ions, i.e., $\mathbf{J} = nq\mathbf{v}$. With an electron particle density $n \simeq 10^{29}\,\mathrm{m^{-3}}$ at the base of the solar convection zone, the required drift speed is a minuscule $|\mathbf{v}| \sim 10^{-15}\,\mathrm{m\ s^{-1}}$.

Drift current

1.1.2 Timescales and the magnetic Reynolds number

The relative importance of induction versus dissipation, and associated timescales, can be estimated by dimensional analysis of Eq. (1.5). Assume that it is possible to identify *a priori* a characteristic values u_0 for the flow speed, and L for a length scale adequately characterizing the spatial variations of both the flow and magnetic field. Replacing spatial differential operators by $1/L$ and temporal derivatives by $1/\tau$ in eq. (1.5) leads to:

$$\frac{1}{\tau} \sim \frac{u_0}{L} - \frac{\eta}{L^2}\ . \tag{1.9}$$

The ratio of the first to second term on the RHS of Eq. (1.9) yields a measure of the relative importance of induction versus dissipation. This dimensionless ratio is known as the *Magnetic Reynolds number*:

Magnetic Reynolds number

$$\mathrm{Rm} = \frac{u_0 L}{\eta}\ . \tag{1.10}$$

With the magnetic diffusivity $\eta \sim 1\,\mathrm{m^2\,s^{-1}}$ for the bulk of the solar convection zone, $u_0 \sim 10\,\mathrm{m\,s^{-1}}$ for deep convection, and L set equal to the solar radius $R_\odot = 6.96 \times 10^8\,\mathrm{m}$, we get $\mathrm{Rm} \sim 10^{10}$, indicating that Ohmic dissipation is very inefficient on global solar scales. Note that this is not so much because u_0 is particularly large or η very small —copper at room temperature is a much better electrical conductor than the plasma in the solar interior,— but is instead a consequence of the large spatial scale of the system. Equation (1.9) also yields two natural timescales for magnetic field evolution, namely the *advective timescale*:

$$\tau_u = L/u_0\ , \tag{1.11}$$

Advection time

and the *diffusive timescale*:

$$\tau_\eta = L^2/\eta\ . \tag{1.12}$$

Diffusion time

Note that under these definitions $\mathrm{Rm} \equiv \tau_\eta/\tau_u$. Using the same numerical values as above, we get $\tau_u \simeq 1\,\mathrm{yr}$ and $\tau_\eta \simeq 10^{10}\,\mathrm{yr}$, the latter being twice the age of

the Sun[1]. The very long diffusive timescale implies that we must look to the flow $\mathbf{u}$ to explain the much shorter evolutionary timescales observed, from the decadal cycle period, down to minutes for the evolution of small photospheric magnetic flux concentrations.

1.1.3 Dynamics: the Lorentz force

At first glance the MHD induction equation (1.5) is linear in $\mathbf{B}$, but this apparent linearity is deceptive because magnetic fields alter the inductive flow $\mathbf{u}$ through the Lorentz (magnetic) force. This nonlinear magnetic backreaction is ultimately what limits the strength of the solar magnetic field, and thus the amplitude of the magnetic activity cycle. In the MHD limit, the magnetic force per unit volume acting on the plasma is given by

Lorentz force

$$\mathbf{F} = \mathbf{J} \times \mathbf{B} \tag{1.13}$$

(see §2.2 in Davidson, 2001, for an illuminating derivation). At the microscopic level the Lorentz force acts on individual charged constituents, but in a collisionally-dominated plasma the momentum so transfered to these charged constituents is very rapidly redistributed to neutrals (if there are any around) via collisions, so that the plasma as a whole experiences a volumetric body force.

It will often prove useful to decompose this force into two contributions:

$$\mathbf{J} \times \mathbf{B} = \frac{1}{\mu_0}(\nabla \times \mathbf{B}) \times \mathbf{B} = \nabla \left(\frac{\mathbf{B}^2}{2\mu_0} \right) + \frac{1}{\mu_0}(\mathbf{B} \cdot \nabla)\mathbf{B} \; . \tag{1.14}$$

Magnetic pressure
Magnetic tension

The first term on the RHS is the gradient of magnetic pressure, and the second is magnetic tension.

1.1.4 Flux freezing and ideal MHD

The plasma in the solar interior and atmosphere is characterized by a relatively high electrical conductivity, which leads to $\mathrm{Rm} \gg 1$ on scales ranging from convection through active regions up to the solar radius. This has crucial consequences for the dynamical interaction between flow and magnetic fields.

Going back to Faraday's Law (1.1), but now expressed in its integral form:

Faraday's law

$$\int_S (\nabla \times) \cdot \hat{\mathbf{n}} \mathrm{dS} = \oint_\gamma \mathbf{E} \cdot \mathrm{d}\boldsymbol{\ell} = -\frac{\partial}{\partial \mathrm{t}} \int_\mathrm{S} \mathbf{B} \cdot \hat{\mathbf{n}} \, \mathrm{dS} \; , \tag{1.15}$$

where the first equality results from the use of Stokes's theorem. Here S is some arbitrarily-shaped surface with local normal unit vector $\hat{\mathbf{n}}$, bounded by the closed contour γ. Both are fixed in space (Eulerian representation), so that $\int_S$ and $\partial/\partial t$ commute. This leads to:

$$\oint_\gamma \mathbf{E} \cdot \mathrm{d}\boldsymbol{\ell} = -\frac{\partial}{\partial \mathrm{t}} \int_\mathrm{S} \mathbf{B} \cdot \hat{\mathbf{n}} \, \mathrm{dS} \; , \tag{1.16}$$

[1]Note that these and similar estimates presented in these class notes are sensitively dependent on the exact choice of length scale L.

The LHS is the electromotive force, and the RHS is the time derivative of the magnetic flux Φ_B crossing the surface S:

$$\Phi_B = \int_S \mathbf{B} \cdot \hat{\mathbf{n}} \mathrm{dS} \ . \tag{1.17}$$

Magnetic flux

Assume now that S is a material surface moving (non-relativistically) with the fluid. The above expression still holds provided the partial time derivative is replaced by the Lagrangian (or material) derivative $\mathrm{D}/\mathrm{D}t \equiv \partial/\partial t + \mathbf{u} \cdot \nabla$. Moreover, the co-moving surface (and bounding contour γ) being by definition at rest with respect to the moving fluid, $\mathbf{E}$ can be replaced by $\mathbf{J}/\sigma$. Thus in this Lagrangian viewpoint Eq. (1.15) becomes:

$$\frac{1}{\sigma} \oint_\gamma \mathbf{J} \cdot \mathrm{d}\boldsymbol{\ell} = -\frac{\mathrm{D}}{\mathrm{Dt}} \int_\mathrm{S} \mathbf{B} \cdot \hat{\mathbf{n}} \, \mathrm{dS} \ . \tag{1.18}$$

In the limit of infinite electrical conductivity, this expression reduces to:

$$\frac{\mathrm{D}}{\mathrm{D}t} \int_S \mathbf{B} \cdot \hat{\mathbf{n}} \, \mathrm{dS} = 0 \ . \tag{1.19}$$

This indicates that the magnetic flux threading any material surface of arbitrary shape and orientation is conserved as the surface is transported and/or deformed by the flow. This is known as *flux freezing*.

Flux freezing

With the magnetic field expressed in terms of a vector potential $\mathbf{A}$ via $\mathbf{B} = \nabla \times \mathbf{A}$, Stokes' theorem allows to rewrite Eq. (1.19) in terms of the circulation Γ of $\mathbf{A}$:

$$\frac{\mathrm{D}\Gamma}{\mathrm{D}t} = 0 \ , \qquad \Gamma = \oint_\gamma \mathbf{A} \cdot \mathrm{d}\boldsymbol{\ell} \ . \tag{1.20}$$

As depicted on Figure 1.1, Equation (1.20) requires that a single magnetic field-line threading any material surface bounded by the contour γ must remain "attached" to that surface as it is moved and deformed by the flow. Since the argument holds even for any infinitesimal contour enclosing any single fieldline, one must conclude that in the limit of infinite conductivity, magnetic fieldlines must move with the fluid, i.e., they are "frozen in". This is known as *Alfvén's theorem*[2] (see also §3.1 in Moffatt and Dormy, 2019).

Alfvén's theorem

Alfvén's theorem can also be understood upon recalling that in MHD what sustains the magnetic field is the current density $\mathbf{J}$, itself associated with the very small drift speed between charged constituents of the globally neutral plasma (viz. §1.1.2). Infinite electrical conductivity implies that electrical charges drift through the plasma without the associated current density being attenuated; in other words, the current system $\mathbf{J}$ moves along with the bulk flow, and so does the magnetic field, as per Ampère's Law (1.4).

The case of infinite conductivity (equivalently, $\eta = 0$ or $\mathrm{Rm} \to \infty$) defines the *ideal MHD* regime. The MHD induction equation (1.5) then becomes

Ideal MHD

[2]This is identical to the behavior of vorticity lines in an inviscid fluid; in that hydrodynamical context the equivalent of (1.20) is known as Kelvin's theorem.

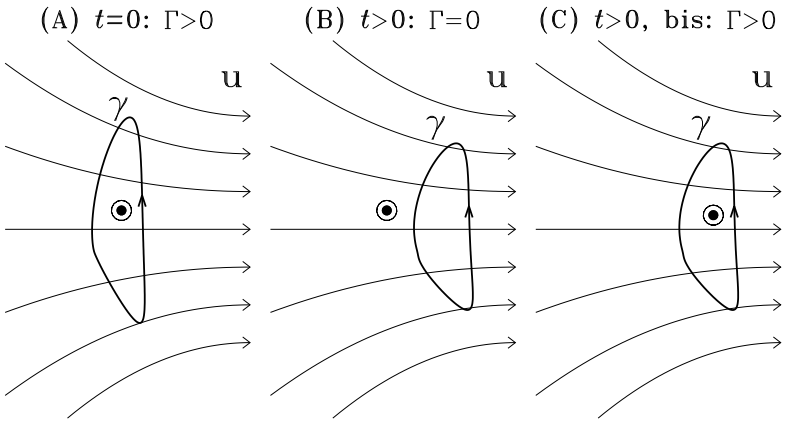

Figure 1.1: In (A), a material contour γ bounds a surface S threaded by a single magnetic fieldline pointing outside the page (indicated by a "$\odot$"). Under the right-hand rule, the circulation Γ of the associated vector potential is > 0. In (B), the contour has moved to the right but the fieldline has stayed behind; now $\Gamma = 0$, and so is the magnetic flux threading the surface bounded by γ. Equation (1.19) precludes this in the ideal MHD limit, requiring instead that the situation be as depicted in (C), where the magnetic fieldline has moved so as to remained enclosed by the material contour γ. This is flux freezing.

identical to the kinematic theorem describing the advection of a line element by a flow $\mathbf{u}$, implying again that magnetic fieldlines move with the fluid (see, e.g., Davidson 2001, §2.7.4). The consequent ability of the fluid flow to bend and stretch magnetic fieldlines, in the very high Rm regime relevant to solar plasma, is at the heart of the MHD induction mechanism. The strong flow-field coupling embodied in by flux-freezing is also essential for the acceleration of plasma by the Lorentz force.

From the mathematical point of view, the ideal MHD limit $\eta \to 0$ is singular, because the associated small parameter, here η, multiplies the highest order derivatives in Eq. (1.5). As η becomes vanishingly small (or, again equivalently, $\mathrm{Rm} \to \infty$), dissipation persists, but in boundary-layer-like structures of typical thickness $\propto \mathrm{Rm}^{-1/2}$. Outside of these structures, Ohmic dissipation remains negligible; flux freezing is thus expected to hold in the bulk of the fluid.

1.1.5 Magnetic Helicity

Flux freezing has far-reaching consequences because it also implies that magnetic fieldlines cannot break or cross one another, which poses a strong topological constraint on the field's spatiotemporal evolution. This can be quantified through magnetic helicity, a global topological measure of linkage between magnetic flux systems threading a volume V Berger (1999); Pevtsov et al. (2014):

Magnetic helicity

$$\mathcal{H}_B = \int_V \mathbf{A}\cdot\mathbf{B}\mathrm{dV}, \tag{1.21}$$

where again the vector potential $\mathbf{A}$ is such that $\mathbf{B} = \nabla\times\mathbf{A}$. In a closed system, i.e. without helicity flux through its boundaries, magnetic helicity can be shown to evolve according to:

$$\frac{\mathrm{d}}{\mathrm{d}t}\int \mathbf{A}\cdot\mathbf{B}\mathrm{dV} = -2\mu_0\eta\int \mathbf{J}\cdot\mathbf{B}\mathrm{dV}\ , \tag{1.22}$$

where the quantity $\mathbf{J}\cdot\mathbf{B}$ is the *current helicity* (see Brandenburg and Subramanian, 2005; Schrijver and Siscoe, 2009, chap. 3). In ideal limit $\eta\to 0$, which is the relevant limit for the interiors and atmospheres of the sun (and stars), the RHS vanishes and Eq. (1.22) then indicates that total helicity must be conserved, or at best vary on the long diffusive timescale τ_η. Conservation of magnetic helicity thus puts a strong constraint on the high-Rm amplification of any magnetic field that carries a net helicity, which is certainly the case with the large-scale solar magnetic field.

Current helicity

Helicity conservation

1.1.6 Energetics

An evolution equation for magnetic energy can be constructed by taking the scalar product of the magnetic field $\mathbf{B}$ on both sides the MHD induction equation (1.5). After exerting considerable vector calculus skills and integrating over the volume V containing the plasma and magnetic field, one arrives at:

Magnetic energy

$$\frac{\mathrm{d}E_B}{\mathrm{d}t} \equiv \frac{\mathrm{d}}{\mathrm{d}t}\int_V \frac{\mathbf{B}^2}{2\mu_0}\mathrm{dV} = -\oint_{\partial\mathrm{V}} \mathbf{S}\cdot\hat{\mathbf{n}}\,\mathrm{dA} - \frac{1}{\sigma}\int_{\mathrm{V}}\mathbf{J}^2\mathrm{dV} - \int_{\mathrm{V}}\mathbf{u}\cdot(\mathbf{J}\times\mathbf{B})\mathrm{dV} \tag{1.23}$$

where $\mathbf{S}$ is the Poynting (electromagnetic energy) flux:

$$\mathbf{S} = \frac{1}{\mu_0}\mathbf{E}\times\mathbf{B} \qquad [\mathrm{W\,m^{-2}}]\ . \tag{1.24}$$

The associated term on the RHS of Eq. (1.23) is zero for an isolated star embedded in vacuum[3].

The second term on the RHS is Ohmic dissipation, irreversibly decreasing total magnetic energy by converting it to heat. In MHD this *Joule heating* is given by the *Ohmic dissipation function*:

$$\phi_B = \frac{\eta}{\mu_0}(\nabla\times\mathbf{B})^2 \qquad [\mathrm{J\,m^{-3}\,s^{-1}}]\ . \tag{1.25}$$

The third term in Eq. (1.23) expresses the work per unit time done by (on) the flow against (by) the Lorentz force. This is the channel through which the

[3]This follows from $\mathbf{E}$ dropping with distance at best as r^{-2} (if a net electric charge is present) and $\mathbf{B}$ as r^{-3} (for a dipolar magnetic field). With the surface element dA increasing as r^2, the integrand in the surface integral on the RHS of (eq. 1.23) drops at least as r^{-3}, which guarantees that the integral vanishes as the boundary ∂V is pushed to $r\to\infty$.

kinetic energy of the flow can be converted to electromagnetic energy, or vice versa. If $\mathbf{u}\cdot(\mathbf{J}\times\mathbf{B}) < 0$ then the plasma system converts kinetic energy of the flow into magnetic energy. If this happens in a manner sufficiently efficient to offset losses due to Ohmic dissipation so that $\mathrm{d}E_B/\mathrm{d}t > 0$, then the plasma system is called a *dynamo*. This requirement is the very essence of any dynamo process, and also reveals its fundamentally nonlinear nature.

Dynamo energy conversion

The opposite case $\mathbf{u}\cdot(\mathbf{J}\times\mathbf{B}) > 0$ implies that the magnetic field transfer energy to the plasma flow. Most eruptive manifestations of solar activity are powered in this manner (viz. Lectures by Francesca Zuccarello).

1.2 The many solar dynamo problems

In its conceptually simplest form, the dynamo problem consists in finding a flow $\mathbf{u}$ which, when inserted in the MHD induction equation (1.5), leads to amplification of and sustenance of $\mathbf{B}$ against Ohmic dissipation. From this point of view our prospects are quite good, because vigorous flows abound in the sun. Thermally-driven turbulent convection transports the bulk of the solar luminosity in the outer 30% of the sun's radius. This same turbulent convection also generates Reynolds stressess driving inverse cascades that power large-scale flows, notably *differential rotation* and *meridional circulation* (see, e.g. Miesch and Toomre, 2009). Energetically, solar convection and differential rotation are the primary contributors to $\mathbf{u}$ in Eqs. (1.5) and (1.23).

Thermal convection

Differential rotation
Meridional circulation

The structure of the inductive term $\nabla\times(\mathbf{u}\times\mathbf{B})$ in the MHD induction equation (1.5) certainly suggests that magnetic fields are produced on a spatial scale commensurate with that of the flow $\mathbf{u}$. Such flows are characterized as *small-scale dynamos* and will be discussed at length later this week in the Lectures by Matthias Rempel. As his Lectures will show, small-scale dynamo action provides a convincing explanatory framework for the origin of the strong and spatiotemporally intermittent small magnetic flux elements observed in the solar photosphere (see Lectures by Luis Bellot Rubio).

Magnetic elements

In contrast, the magnetic field component associated with the solar 11-yr activity cycle is structured on scales much larger than convection, commensurate in fact with the solar radius, and is characterized by a significant amount of net magnetic flux on those scales, persisting over timecales much longer than the convective turnover time. Fluid dynamos achieving the amplification and sustenance of such magnetic fields are known as *large-scale dynamos*. They can still be powered in part or in totality by small-scale fluid motions such as thermally-driven convection, but one must then conceive of a plausible physical scenario where by a turbulent flow with typical scales of order 10^5–10^7 m and 10^3–10^6 s, induce and sustain against dissipation a spatiotemporally coherent magnetic component with scales of order 10^9 m and 10^8 s. As we shall see shortly, this turns out to be possible, although far from trivial.

Large-scale dynamo

The observed spatiotemporal evolution of the solar magnetic field on large spatial scales ($\approx R_\odot$) conventionally associated with the solar cycle suggest that the dynamo loop can be broken into two steps, whereby the action of fluid

flows on a pre-existing poloidal component (P, fieldlines contained in meridional planes) induces a toroidal (T, zonally-oriented) magnetic component, and in turn flows acting on this toroidal component generate a new poloidal component, of polarity opposite to that originally present. Schematically, the process can be represented as:

$$... \rightarrow P(+) \rightarrow T(-) \rightarrow P(-) \rightarrow T(+) \rightarrow P(+) \rightarrow ... \tag{1.26}$$

where the ($\pm$) indicate the polarity of each large-scale component. In reality the situation is not as cleanly delineated, as both steps are operating concurrently, and may not be spatially coincident, in which case a magnetic flux transport process is required to link the two regions of induction. Nonetheless, this two-step framework will prove useful in categorizing the various types of solar cycle models discussed throughout this lecture.

For the $P(\pm) \rightarrow T(\mp)$ step, the vast majority of models and scenarios rely on the shearing of a large-scale poloidal field by differential rotation (§1.4 below); here a key turning point occurred in the later 1980's, when helioseismology succeeded in mapping the internal solar differential rotation, revealing the presence of the multiple rotational shear regions (Brown et al., 1989; Dziembowski et al., 1989).

In contrast, concensus has not yet been reached regarding the $T(\pm) \rightarrow P(\pm)$ step, for which a variety of mechanisms are being considered, the most promising of which to be introduced later in this Lecture. All ultimately rely on the Coriolis force to generate an azimuthally-oriented electromotive force through non-reflectionally symmetric fluid motions acting on a pre-existing large-scale toroidal magnetic field.

1.3 Amplification by Stretching and Squeezing

Inductive amplification of magnetic fields can take place across a bewildering variety of physical scenarios. Working in the ideal MHD limit $\eta \rightarrow 0$, it will prove useful to first recast the induction equation (1.5) in the form:

$$\underbrace{\left(\frac{\partial}{\partial t} + \mathbf{u}\cdot\nabla\right)}_{\text{advection}}\mathbf{B} = \underbrace{(\mathbf{B}\cdot\nabla)\mathbf{u}}_{\text{shearing}} - \underbrace{\mathbf{B}(\nabla\cdot\mathbf{u})}_{\text{compression}} \ . \tag{1.27}$$

The advection operator on the LHS is just the Lagrangian derivative, and captures the bulk transport of $\mathbf{B}$ by the flow $\mathbf{u}$, without deformation of amplification. The shearing and compression term both act as source terms, and thus can amplify $\mathbf{B}$; for very subsonic flows the mass conservation constraint is well approximated by $\nabla\cdot(\varrho\mathbf{u}) \simeq 0$, so that $\nabla\cdot\mathbf{u} = -\mathbf{u}\cdot\nabla(\log\varrho)$. In the strongly stratified outer convection zone and photosphere, strong field amplification can take place via this term, with the scale height of the stratification now imprinting itself on the vertical structure of the induced field. More on this in Matthias Rempel's Lectures.

kinematic approximation

Both terms on the RHS of (1.27) are linear in $\mathbf{B}$ and proportional to derivatives of $\mathbf{u}$; Assuming again that $\mathbf{u}$ is steady, the required mathematical ingredients for exponential growth of the magnetic field are clearly present in Eq. (1.27). How this pans out in a real flow, however, turns out to be anything but simple, especially with the nonlinear backreaction of the Lorentz force is taken into account.

1.4 Shearing by differential rotation

An obvious way to have a dynamo producing net magnetic flux on the scale of the solar radius is to capitalize on the inductive action of a flow itself structured on this large scale. Solar differential rotation is an obvious candidate.

Poloidal magnetic field
Differential rotation

Working in spherical polar coordinates (r, θ, ϕ), we consider the shearing of an axisymmetric $(\partial/\partial\phi \equiv 0)$ poloidal magnetic field (component contained in meridional planes) by a steady differential rotation (an axisymmetric zonal flow):

$$\mathbf{u} = \varpi\, \Omega(r,\theta)\hat{\mathbf{e}}_\phi \ . \tag{1.28}$$

$$\mathbf{B}_p \equiv B_r(r,\theta)\hat{\mathbf{e}}_r + B_\theta(r,\theta)\hat{\mathbf{e}}_\theta \ . \tag{1.29}$$

where $\varpi \equiv r\sin\theta$ is the cylindrical radius. Under this very simple configuration, and neglecting Ohmic dissipation, the three components of the induction equation then reduce to

$$\frac{\partial B_r}{\partial t} = 0 \ , \tag{1.30}$$

$$\frac{\partial B_\theta}{\partial t} = 0 \ , \tag{1.31}$$

$$\frac{\partial B_\phi}{\partial t} = \varpi[B_r\hat{\mathbf{e}}_r + B_\theta\hat{\mathbf{e}}_\theta]\cdot\nabla\Omega \ . \tag{1.32}$$

For a purely poloidal magnetic field at $t = 0$, the ϕ-component then integrates to

$$B_\phi(r,\theta,t) = \varpi(\mathbf{B}_p\cdot\nabla\Omega)\, t \ , \tag{1.33}$$

Toroidal magnetic field

i.e., at any point in the meridional $[r, \theta]$ plane, a magnetic component oriented in the zonal direction —a toroidal field— grows linearly in time, at a rate proportional to the local poloidal field strength and magnitude of the rotational shear. Note that in itself, such a stretching of the poloidal field in the zonal direction leaves the strength of the poloidal component unaffected. Note also that for this axisymmetric configuration, the only possible steady-state solutions $(\partial/\partial t = 0)$ must satisfy

$$[B_r\hat{\mathbf{e}}_r + B_\theta\hat{\mathbf{e}}_\theta]\cdot\nabla\Omega = 0 \ , \tag{1.34}$$

Ferraro theorem

i.e., the angular velocity must be constant along any poloidal fieldline. This is known as *Ferraro's theorem*.

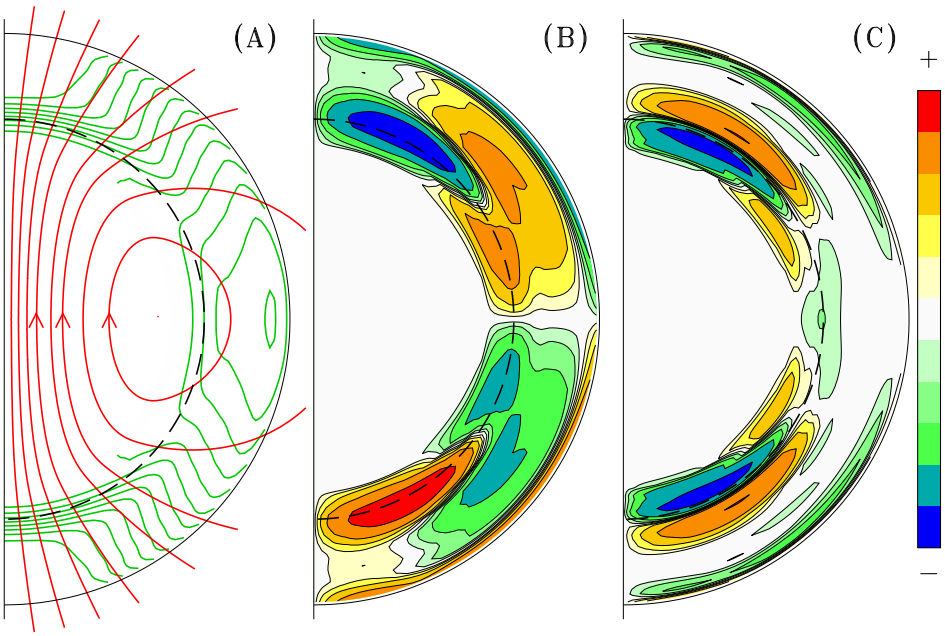

Figure 1.2: Shearing of an axisymmetric large-scale poloidal magnetic field (red fieldlines on panel A) by the solar differential rotation (green isocontours in A). The resulting toroidal magnetic component on panel B is antisymmetric about the equatorial plane, and peaks here in the tachocline, where rotational shear is strongest. The associated Lorentz force on panel C always opposes the shearing flow, as is required for energy transfer from the flow to the magnetic field. The dashed circular arc indicates the base of the convective envelope.

Figure 1.2 illustrated this shearing process, for the case of a dipolar large-scale magnetic field (red fieldlines on panel A) being sheared by a solar internal rotation profile displayed on panel (A) as green isocontours of angular velocity $\Omega(r,\theta)$. Such a profile is characterized by a more rapidly rotating equator and slowly rotating pole through the convective envelope ($0.7 \leq r/R \leq 1$), matching onto a rigily rotating radiative core across a thin rotational shear layer called the *tachocline* (Brown et al., 1989; Spiegel and Zahn, 1992; Howe, 2009), straddling the core-envelope interface (dashed circular arcs on all panels of Fig. 1.2). The angular velocity also drops significantly in the subsurface layers, generating a layer of strong negative radial shear ($\partial\Omega/\partial r < 0$) from the equator up to $\sim 60^\circ$ latitude. Panel (B) is a color rendering of the toroidal magnetic component produced by this shearing process. The strongest toroidal fields are produced in regions of strong shear where poloidal fieldlines are most closely aligned with $\nabla\Omega$, as expressed by Eq. (1.33). For the solar-like differential rotation profile used here, strong toroidal fields are produced in the tachocline and subsurface

differental rotation

Tachocline

Surface shear layer

shear layer through the agency of radial shear, and at mid-latitudes within the convection zone primarily via the latitudinal shear.

One can readily verify that a solar-like $10^{-3}\,\mathrm{T}$ (10 G) poloidal field, when subjected to a solar-like pole-to-equator angular velocity contrast $+10^{-6}\,\mathrm{rad\,s^{-1}}$ induces in 10 yr a toroidal component of strength $\sim 0.3\,\mathrm{T}$ (3 kG). This is approaching the estimated strength of the sunspot-forming internal solar magnetic field (Fan, 2021, and references therein). It also implies that on large spatial scales the internal zonal (toroidal) component is $\sim 10^3$ more intense than the dipolar (poloidal) component.

Because the latitudinal shear changes sign across the equator, the induced toroidal field will also be antisymmetric about the equator, which is the magnetic parity inferred from Hale's polarity Laws (§1.8.1 below).

Hale's polarity Laws

With the toroidal component growing linearly with time according to Eq. (1.33), so will the Lorentz force. For the setup considered here its component in the ϕ-direction is given by:

$$F_\phi(r,\theta,t) = \frac{t}{\mu_0 \varpi}\mathbf{B}_p \cdot \nabla[\varpi B_\phi(r,\theta,t)] \ . \tag{1.35}$$

This zonal component of the Lorentz force is illustrated on Fig. 1.2C. Careful comparison with panel (A) reveals that the Lorentz force acts here in a direction such as to reduce the rotational shear. This is in fact required by Eq. (1.23) if energy is to be extracted from the flow, to supply the magnetic energy associated with the growth of the toroidal magnetic component. This is a general, robust result, which is not at all restricted to the flow/field configuration considered here.

Setting Eq. (1.35) equal to zonal acceleration per unit mass, dimensional analysis indicates that the Lorentz force will backreact on differential rotation on a dynamical timescale given by:

$$\tau_\Omega = \frac{\mu_0 \varrho L^2 \Omega}{B_p B_\phi} \ . \tag{1.36}$$

Using the numerical values $B_\phi \sim 1\,\mathrm{T}$ and $\varrho \sim 10\,\mathrm{kg\,m^{-3}}$ for the outer half of the solar convection zone yields $\tau_\Omega \sim 10^3\,\mathrm{yr}$; and a $\sim 1\%$ variation in Ω, commensurate with observed solar torsional oscillations (Howe, 2009), can be generated in $\sim 10\,\mathrm{yr}$.

Torsional oscillations

1.5 Cowling's theorem

Rotational shearing of a steady ($\partial/\partial t \equiv 0$) axisymmetric ($\partial/\partial\phi \equiv 0$) poloidal magnetic field by steady differential rotation, as we just considered, obviously cannot produce polarity reversals.

Less obvious but even more important is the fact that this setup in itself, cannot sustain the magnetic field against Ohmic dissipation over timescales of the order of the magnetic diffusion time (Eq. (1.12)). To understand why

nmetric magnetic field

consider the following representation of an axisymmetric magnetic field, whereby its poloidal component is defined in terms of a toroidal vector potential $\mathbf{A} = A(r,\theta,t)\hat{\mathbf{e}}_\phi$:

$$\mathbf{B}(r,\theta,t) = \underbrace{\nabla \times (A(r,\theta,t)\hat{\mathbf{e}}_\phi)}_{\text{poloidal}} + \underbrace{B(r,\theta,t)\hat{\mathbf{e}}_\phi}_{\text{toroidal}} \ . \tag{1.37}$$

This ensures $\nabla \cdot \mathbf{B} = 0$ for any axisymmetric magnetic field so constructed. Again retaining only the contribution of differential rotation to the large-scale flow (viz. Eq. (1.28)), substitution of Eq. (1.37) into the induction equation allows to separate the latter into the following pair of evolution equations for A and B:

$$\frac{\partial A}{\partial t} = \eta \left(\nabla^2 - \frac{1}{\varpi^2} \right) A \ , \tag{1.38}$$

$$\frac{\partial B}{\partial t} = \eta \left(\nabla^2 - \frac{1}{\varpi^2} \right) B + \varpi (\nabla \times (A\hat{\mathbf{e}}_\phi)) \cdot \nabla\Omega \ , \tag{1.39}$$

where the magnetic diffusivity η is assumed constant. The second term on the RHS of (2.4) acts as a source term for B, proportional to A; however, no such source is present on the RHS of Eq. (2.3). As a consequence, the latter can only resistively decay on the diffusive timescale (1.12). Once A has vanished, the source term on the RHS of Eq. (2.4) also vanishes, and from that point on B will also decay on the resistive timescale. This is the essence of *Cowling's theorem*: an axisymmetric flow cannot support an axisymmetric magnetic field against Ohmic dissipation.

Cowling's theorem

The unbounded linear growth of the toroidal magnetic field obtained previously in the case of rotation shearing (Eq. (1.33)) results from having assumed a steady poloidal component; as a solution of the induction equation, this is therefore only (approximately) valid for times much shorter than the diffusion time (1.12). In itself, the flow/field system of §1.4 is not a dynamo.

Escape from Cowling's theorem must therefore involve departures from axisymmetry. In the solar case salvation can be found in turbulent convection, but at the price of facing the wide disparity of scales and dynamical intricacies characterizing MHD turbulence at high fluid and magnetic Reynolds numbers.

1.6 Mean-field electrodynamics and the α-effect

It is an observed fact that solar convection is characterized by spatial scales much smaller that the solar radius; and that the magnetic field associated with the solar activity cycle is spatially organized on the much larger global scale of the sun. This *scale separation* is at the core of *mean-field electrodynamic*, an approach allowing to capture statistically the inductive effect of a small-scale turbulent flow acting on a large-scale magnetic component.

1.6.1 Scale separation and the turbulent emf

Scale separation

The first step is to separate the total flow and magnetic field into large-scale and small-scale contributions:

$$\mathbf{B} = \langle \mathbf{B} \rangle + \mathbf{b}' \ , \qquad \mathbf{u} = \langle \mathbf{U} \rangle + \mathbf{u}' \ , \tag{1.40}$$

where the angular brackets denote an averaging over an intermediate length scale, sufficiently large so that $\langle \mathbf{u}' \rangle = 0$ and $\langle \mathbf{b}' \rangle = 0$. This is not a linearization, as no assumptions are being made regarding the magnitude of $\mathbf{u}'$ versus $\langle \mathbf{U} \rangle$, or $\mathbf{b}'$ vs $\langle \mathbf{B} \rangle$. Inserting Eq. (1.40) into the MHD induction equation (1.5) and averaging leads to the *mean-field induction equation*:

$$\frac{\partial \langle \mathbf{B} \rangle}{\partial t} = \nabla \times \left(\langle \mathbf{U} \rangle \times \langle \mathbf{B} \rangle + \boldsymbol{\xi} - \eta \nabla \times \langle \mathbf{B} \rangle \right) \ , \tag{1.41}$$

Mean emf

where

$$\boldsymbol{\xi} = \langle \mathbf{u}' \times \mathbf{b}' \rangle \tag{1.42}$$

is the *mean electromotive force* (hereafter emf) produced by correlated fluctuations of the flow and field at small scales. The key point is that this emf can act as a source term for $\langle \mathbf{B} \rangle$, because it will not necessarily average to zero, even though $\mathbf{u}'$ and $\mathbf{b}'$ individually do[4]. If Eqs. (1.40) are inserted into the MHD induction equation, without averaging, but now subtracting Eq. (1.41), one obtains an evolutionary equation for the small scale field:

$$\frac{\partial \mathbf{b}'}{\partial t} = \nabla \times \left(\langle \mathbf{U} \rangle \times \mathbf{b}' + \mathbf{u}' \times \langle \mathbf{B} \rangle + \mathbf{u}' \times \mathbf{b}' - \boldsymbol{\xi} - \eta \nabla \times \mathbf{b}' \right) \ . \tag{1.43}$$

Formally solving Eqs. (1.41) and (1.43) as a coupled system is not a desirable avenue here, as the whole aim of the mean-field approach is to avoid having to deal explicitly with the small scales. Consider instead the mathematical nature of the coupling between Eqs. (1.41) and (1.43); for $\mathbf{u}'$ considered given, Eq. (1.43) is linear in $\mathbf{b}'$, except for a source term $(\mathbf{u}' \times \langle \mathbf{B} \rangle)$ linear in $\langle \mathbf{B} \rangle$; similarly, with $\langle \mathbf{U} \rangle$ and $\mathbf{u}'$ given, Eq. (1.41) is linear in $\langle \mathbf{B} \rangle$, except for $\boldsymbol{\xi}$ providing a source term linear in $\mathbf{b}'$. It follows that the mean emf can be expressed as a linear (tensorial) development in terms of the large-scale magnetic field:

$$\mathcal{E}_i = a_{ij} \langle B \rangle_j + b_{ijk} \frac{\partial \langle B \rangle_j}{\partial x_k} + ... \ , \tag{1.44}$$

where the tensors $\mathbf{a}$, $\mathbf{b}$, etc, depend on the statistical properties of $\mathbf{u}'$, but cannot depend on $\langle \mathbf{B} \rangle$. It is physically illuminating to explicitly separate the symmetric and antisymmetric parts of these tensors, so that the emf becomes

$$\boldsymbol{\xi} = \boldsymbol{\alpha} \cdot \langle \mathbf{B} \rangle + \boldsymbol{\gamma} \times \langle \mathbf{B} \rangle - \boldsymbol{\beta} \cdot (\nabla \times \langle \mathbf{B} \rangle) + ... \tag{1.45}$$

[4]This mean electromotive force is entirely analogous to the Reynolds stresses appearing in the Navier-Stokes unmagnetized fluid equations upon introducing scale separation and averaging.

The symmetric rank-2 tensor $\boldsymbol{\alpha}$ is just the symmetric part of a_{ij}, the pseudo-velocity $\boldsymbol{\gamma}$ collects its three independent antisymmetric components, and the rank-2 tensor $\boldsymbol{\beta}$ collects the antisymmetric parts of b_{ijk}:

$$\alpha_{ij} = \frac{1}{2}(a_{ij} + a_{ji}) \ , \tag{1.46}$$

$$\gamma_k = -\frac{1}{2}\epsilon_{kij} a_{ij} \ , \tag{1.47}$$

$$\beta_{ij} = \frac{1}{4}(\epsilon_{ikl} b_{jkl} + \epsilon_{jkl} b_{ikl}) \ , \tag{1.48}$$

(see Krause and Rädler, 1980; Schrinner et al., 2007, for further details). These three quantities capture the physical effects most often invoked in constructing mean-field dynamo models of the solar cycle, and in principle can be computed if the statistical properties of the turbulent flow and field are known. For perfectly homogeneous, isotropic turbulence, one expects

$$\alpha_{ij} = \alpha\delta_{ij} \ , \tag{1.49}$$

$$\gamma_k = 0 \ , \tag{1.50}$$

$$\beta_{ij} = \beta\delta_{ij} \ , \tag{1.51}$$

where δ_{ij} is the usual Kronecker delta. Substituting Eq. (1.45) in the mean-field induction equation (1.41) then yields:

$$\frac{\partial \langle \mathbf{B} \rangle}{\partial t} = \nabla \times (\langle \mathbf{U} \rangle \times \langle \mathbf{B} \rangle + \alpha \langle \mathbf{B} \rangle - (\eta + \beta) \nabla \times \langle \mathbf{B} \rangle) \ . \tag{1.52}$$

The α-term now emerges as a (turbulent) electromotive force aligned with the mean-magnetic field, in contrast to the conventional motional emf $\propto \langle \mathbf{U} \rangle \times \langle \mathbf{B} \rangle$ which is perpendicular to $\langle \mathbf{B} \rangle$. This contribution to the total turbulent emf, crucial in many dynamo models discussed further below, is known as the *α-effect*, and is non-zero for flows lacking reflection symmetry.

α-effect

The β-term in (1.45), makes an additive contribution to the magnetic diffusivity η, and can thus be interpreted as *turbulent diffusion* of $\langle \mathbf{B} \rangle$. The α- and β-effects in Eq. (1.52) embody, respectively, constructive and destructive folding of the mean-magnetic field by the small-scale turbulent flow (see Fig. 1.3). In other words, turbulence may provide a mean-electromotive force acting as a source for the mean-magnetic field, but it will also inevitably generate enhanced dissipation of that same mean magnetic field. No free lunch !

turbulent diffusivity

The $\boldsymbol{\gamma}$ term, when present, adds to the mean flow $\langle \mathbf{U} \rangle$. This is a non-solenoidal ($\nabla \cdot \boldsymbol{\gamma} \neq 0$) pseudo-flow, in the sense that it acts only as such on the mean magnetic field $\langle \mathbf{B} \rangle$. It is known as *turbulent pumping*.

turbulent pumping

1.6.2 Calculating the α-effect and turbulent diffusion

Approximate expressions for α, β and $\boldsymbol{\gamma}$ can be obtained for turbulence that is mildly inhomogeneous and anisotropic, as would be expected in the presence

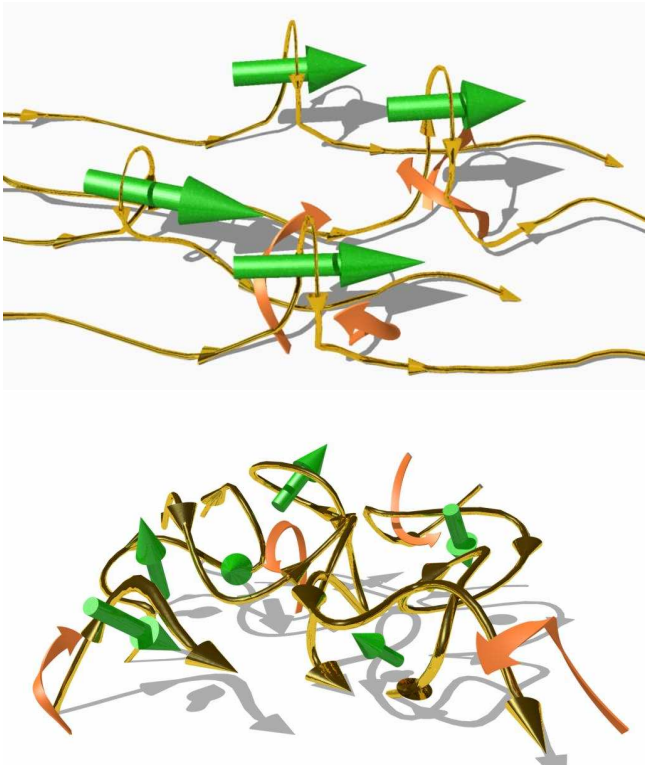

Figure 1.3: Illustration of constructive (top) and destructive (bottom) folding of a mean-magnetic field by a small-scale flow. In (A), radially-diverging cyclonic updrafts (orange flat arrows) create magnetic field loops with associated local electrical current density (green 3D arrows), as per Ampère's Law. If the field suffers relatively little deformation, then these local currents are oriented approximately parallel to the original mean magnetic field, and collectively add up to a mean current density parallel to the mean field. In (B), a "random" small-scale flow (orange flat arrows) acting on a mean magnetic field generate randomly-oriented magnetic field loops, with which are associated randomly-oriented local current densities; unlike in (A), these now vectorially add up to zero, but still contribute to enhanced Ohmic dissipation. Artwork kindly provided by D. Passos.

of stratification and rotation. Tractable formulations are restricted to a few specific physical regimes: low magnetic Reynolds number, turbulence with short coherence time, or strong mean magnetic field. In all cases this amounts to the large-scale mean magnetic field suffering little deformation by the small-scale flow, as on Fig. 1.3A. In these regimes it can be shown that:

$$\alpha = -\frac{\tau_c}{3}\langle \mathbf{u}' \cdot (\nabla \times \mathbf{u}')\rangle \ , \tag{1.53}$$

$$\boldsymbol{\gamma} = -\frac{\tau}{6}\nabla\langle(\mathbf{u}')^2\rangle \ , \tag{1.54}$$

$$\beta = \frac{\tau_c}{3}\langle(\mathbf{u}')^2\rangle \ . \tag{1.55}$$

(see, e.g., Ossendrijver, 2003; Brandenburg and Subramanian, 2005; Schrijver and Siscoe, 2009, chap. 3). Order-of-magnitude estimates for the middle of the solar convection zone using $|\mathbf{u}'| \sim 10\,\mathrm{m\,s^{-1}}$ and $\tau_c \sim 1\,$month lead to $\beta \sim 10^8\,\mathrm{m^2 s^{-1}}$, and α and $|\boldsymbol{\gamma}|$ both in the $\mathrm{m\,s^{-1}}$ range.

From the dynamo point of view, the key addition made by the turbulent emf is the α-effect, because it allows to bypass Cowling's theorem. In the solar context, the break of reflection symmetry required to produce a non-vanishing α-effect is imparted on the turbulent flow by the Coriolis force, with convective updrafts developing a systematic sense of twist, counterclockwise (clockwise) in the Northern (Southern) solar hemisphere (Parker, 1955), much like cyclones in Earth's atmosphere, as illustrated schematically on Fig. 1.3A.

Cowling's theorem

Cyclonicity

In this context a key dimensionless grouping is the *Rossby number*, measuring the influence of the Coriolis force on the small-scale flow:

Rossby number

$$\mathrm{Ro} = \frac{u}{2\Omega\, L} \ , \tag{1.56}$$

where u and L are typical velocity and length scales for the flow under consideration, and Ω is the solar angular velocity. Turbulent fluid motions acquire a cyclonic character in the $\mathrm{Ro} < 1$ regime, but not in the opposite situation where $\mathrm{Ro} > 1$. Deep convection, with $u \sim 10\,\mathrm{m\,s^{-1}}$ and $L \sim 10^7\,$m, has $\mathrm{Ro} \sim 0.1$ and so is expected to acquire a cyclonic character, whereas whereas surface granulation, ($u \sim 10^3\,\mathrm{m\,s^{-1}}$ and $L \sim 1000\,$km leading to $\mathrm{Ro} \sim 10^2$) is not. With $\mathrm{Ro} \sim 1$ supergranulation ($u \sim 10^2\,\mathrm{m\,s^{-1}}$ and $L \sim 30\,$Mm) is borderline cyclonic.

Convection
Supergranulation
Granulation

With the break of homogeneity and isotropy provided, respectively, by stratification and rotation, Eq. (1.53) becomes:

$$\alpha = -\frac{16}{15}\tau_c^2 (u')^2 \boldsymbol{\Omega} \cdot \nabla \ln(\varrho u') \ , \tag{1.57}$$

where $u' = \sqrt{\langle(\mathbf{u}')^2\rangle}$ and $\boldsymbol{\Omega}$ is the sun's angular rotation vector. In the sun's convection zone the turbulent convective velocity is independent of latitude to a good first approximation, and increases with radius more slowly than density decreases, so that $\nabla \ln(\varrho u') < 0$. (see Brandenburg and Subramanian, 2005, §6.2, and esp. Note 5). Equation (1.57) thus predict an α-effect varying as $\cos\theta$, positive (negative) in the sun's Northern (Southern) hemisphere, except

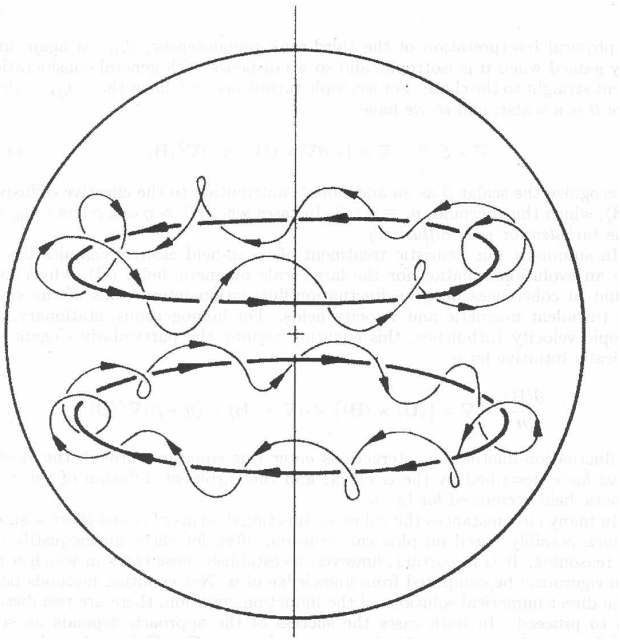

Figure 1.4: Schematic representation of an axisymmetric and equatorially antisymmetric toroidal magnetic field (thick lines) deformed at small scales by cyclonic convective updrafts/downdrafts into meridional planes (thin lines). The collective effect of this deformation is to drive a zonal electrical current parallel to the original toroidal field, oriented in the same direction in both hemisphere. This zonal EMF will thus generate a dipole-like large-scale poloidal magnetic component [Reproduced from Parker 1979, *Cosmical Magnetic Fields*, Oxford: Clarendon Press, p. 548]

at the very base of the convection zone where $\nabla \ln(\varrho u')$ can change sign because convective velocities drop rapidly as downflows impinge on the stably stratified radiative interior.

Imagine now the α-effect acting on a large-scale magnetic toroidal component, such as that generated by shearing of a pre-existing large-scale dipole (viz. §1.4 and Fig. 1.2). Geometrically, the zonally-directed magnetic fieldlines are lifted and twisted into meridional planes, as illustrated schematically on Figure 1.4. The combined effect of many such cyclonic events is to generate a magnetic component in meridional (r, θ) planes —or, equivalently, a zonally-oriented mean electrical current— where there was none originally (Parker, 1955); the net effect is thus to produce a large-scale poloidal magnetic component from a pre-existing large-scale toroidal component, i.e., a $T \rightarrow P$ process. As explained earlier in §1.4, shearing of this poloidal magnetic component can in turn induce a toroidal component. Acting jointly, the α-effect ($T \rightarrow P$) and shearing by differential rotation ($P \rightarrow T$) can thus (in principle) produce a working dynamo

$T \rightarrow P$

loop, each mechanism providing the magnetic field component required by the other to operate. Of course, such a dynamo scenario is only viable provided turbulent induction wins over turbulent dissipation at large spatial scales.

1.6.3 The dynamo number

Consider a simple situation in which no large-scale flow is present. The large-scale magnetic component can then be assumed to be force-free, i.e., it satisfies $\mathbf{J} \times \mathbf{B} = 0$. A wide classes of such force-free magnetic fields can be expressed as:

$$\nabla \times \langle \mathbf{B} \rangle = k \langle \mathbf{B} \rangle \ . \tag{1.58}$$

This is a reasonable approximation if no large-scale flow contributes to induction[5]. Assuming $\beta \gg \eta$ and with neither α nor β depending on position, the substitution of Eq. (1.58) into (1.52) immediately leads to:

$$\frac{\partial \langle \mathbf{B} \rangle}{\partial t} = k(\alpha - k\beta) \langle \mathbf{B} \rangle \ , \tag{1.59}$$

which accepts eigensolutions of the form:

$$\langle \mathbf{B} \rangle (\mathbf{x}, t) = \hat{\mathbf{b}}(\mathbf{x}) \exp(k(\alpha - k\beta)t) \ . \tag{1.60}$$

Growth of the magnetic field is only possible provided

Dynamo number

$$D \equiv \frac{\alpha}{k\beta} > 1 \ . \tag{1.61}$$

The dimensionless combinaison of constants on the RHS of this expression defines the *dynamo number* (D) for this model; the *critical dynamo number* ($D_{\rm crit}$), here equal to unity, is the threshold value marking the onset of exponential growth. Remembering that k is an inverse length scale associated with $\langle \mathbf{B} \rangle$, this indicates that turbulent induction will tend to favor the growth of the eigenmode with the largest spatial scale than can be accomodated in the system, because the smaller magnetic scales are more strongly affected by dissipation[6]. Equation (1.60) also indicates that once D exceeds $D_{\rm crit}$, its value sets the growth rate of the magnetic field.

Critical dynamo number

This exponentially growing magnetic solution evidenty cannot exhibit magnetic polarity reversals, but this can be remedied by introducing a large-scale, uniformly sheared flow in the problem. As first demonstrated by Parker (1955), the linear kinematic form of the mean-field dynamo equations in Cartesian geometry sustain wave-like exponentially growing solutions known as *dynamo waves*. . Parker's model and analytical solution are detailed in Appendix A to these lecture notes. As Lecture 2 will demonstrate, dynamo waves also materialize in both linear and nonlinear mean-field dynamo models in spherical geometry.

dynamo waves

[5]The small-scale magnetic component driving the α-effect cannot be force-free, of course, otherwise no energy transfer from the flow to the magnetic field could take place, as per Eq. (1.23).

[6]These "smaller magnetic scales" characterizing $\langle \mathbf{B} \rangle$ are still much larger than those associated with the small-scale flow $\mathbf{u}'$ driving the α-effect and turbulent diffusivity, as per the assumption of scale separation.

1.7 Electromotive forces from instabilities

The Coriolis force, ultimately responsible for the appearance of the α-effect in non-reflection symmetric convective turbulence, can in principle act on any flow resulting from development of any instabilities, provided its growth rate is roughly commensurate with the solar rotation period.

In the mildly stably stratified upper tachocline, immediately beneath the base of the solar convection zone, the presence of differential rotation and strong magnetic fields is conducive to the growth of a number of hydrodynamical and magnetohydrodynamical instabilities. Under the action of the Coriolis force, the growth of some of these instabilities can generate flows with a net helicity which, upon acting on a pre-existing large-scale magnetic field, can produce a field-aligned electromotive force reminiscent of the α-effect (see, e.g., Ferriz-Mas et al., 1994; Ossendrijver, 2000; Thelen, 2000; Dikpati and Gilman, 2001; Chatterjee et al., 2011). These instabilities are usually invoked to provide the zonal electromotive force required to regenerate the poloidal large-scale component, with shearing of this poloidal component by the tachocline differential rotation (viz. §1.4) to close the dynamo loop.

1.8 Active region decay and the Babcock-Leighton mechanism

We now turn to a distinct $T \to P$ induction mechanism predating the development of mean-field electrodynamics, formulated semi-empirically based instead closely on the observed evolution of the surface magnetic field of the Sun. We thus open this section with an observational detour.

1.8.1 The Laws of Hale and Joy

Magnetic flux rope
Ω-loop

At least on the larger scales, magnetic fields emerge at the photosphere as bipolar magnetic regions (hereafter BMR; see Fig. 1.5, right panel) believed to be associated with magnetic flux ropes buoyantly rising from the solar interior as Ω-loops (Parker, 1955). Two related solar magnetographic pattern of great importance in the dynamo context are known as Hale's Law(s) and Joy's Law, after Hale et al. (1919).

Hale's Laws

Hale's Laws refers to the ordering pattern of magnetic polarities in bipolar magnetic regions observed in the photosphere, most of which being approximately aligned with the E-W direction of solar rotation (see again Fig. 1.5):

- In a given cycle, a given hemisphere always present the same polarity ordering of leading/trailing pole with respect to the direction of rotation.
- In a given cycle, the ordering leading/trailing poles is opposite in the two hemispheres;

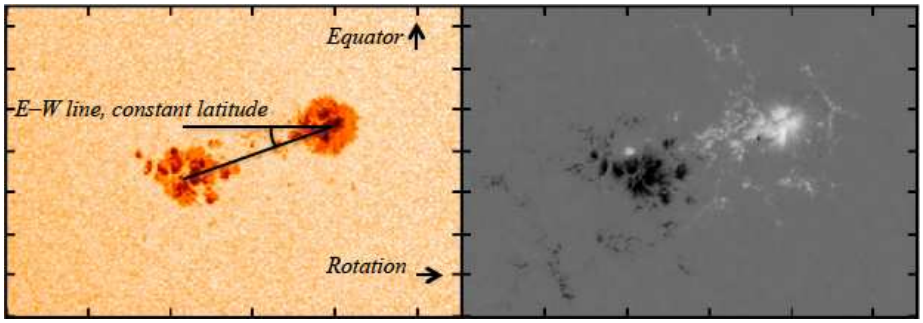

Figure 1.5: Continuum image (left) and magnetogram (right) of NOAA active region 11428 on 2 March 2012. the line segment joining the centers of the two magnetic poles of this "textbook" bipolar magnetic region makes a tilt angle α with the East-West direction of solar rotation, here horizontal. Graphics kindly provided by Aimee Norton, Stanford U.

- This hemispheric polarity ordering reverses from one sunspot cycle to the next.

Hale's Law thus establish the existence of a large-scale equatorially antisymmetric toroidal flux system in the solar interior, reversing polarity from one sunspot cycle to the next. If BMR are interpreted as Ω-loops anchored in this deep-seated toroidal flux system, then its magnetic polarity is given by the trailing polarity of the emerging BMRs.

Joy's Law refers to the fact that, on average, the leading (with respect to rotation) pole of a bipolar magnetic region lies a bit closer to the solar equator than the trailing pole. This tilt with respect to the E-W direction is also illustrated on Fig. 1.5). The observed mean tilt angle γ is found to increase with heliographic latitude (λ). A minimal relationship capturing this variation is

Joy's Laws

$$\gamma = 15.7 \sin \lambda \ , \qquad [\text{degree}] \tag{1.62}$$

(Fisher et al., 1995). Substantial scatter exists about this mean curve, and increases with decreasing unsigned magnetic flux of the BMR. See McClintock and Norton (2013) for more details on the observational characterization (and the many associated subtleties) of Joy's Law.

1.8.2 Stability and buoyant rise of magnetic flux rings

Magnetohydrodynamical numerical simulations of the formation, destabilization, rise and emergence of magnetic flux tubes and ropes through the solar convection zone are extremely challenging, in view of the extreme range of scales involved (see, e.g., Hotta and Iijima, 2020, and references therein). Much of our understanding of the global patterns of magnetic flux emergence and its contribution to the dynamo process powering the solar cycle comes from simplified

models and local area numerical simulations. All relevant aspects of the topic are very comprehensively covered in the extensive review article by Fan (2021); what follows focuses on results most relevant to foregoing discussion of the Babcock-Leighton mechanism (§1.8.3 below).

In the ideal MHD regime, the MHD induction equation becomes structurally identical to the evolution equation for a line element passively advected by a flow (see §2.7.2 in Davidson, 2001). This is at the root of the *thin flux tube approximation* (Spruit, 1981), which reduces a magnetic flux tube or rope to a material line, an approximation justified as long as the tube's cross-sectional radius is much smaller than all other relevant length scale in the system. This thin flux tube regime turns out extremely useful and computationally efficient in modelling the destabilisation and buoyant rise (the so-called Parker instability) of magnetic flux ropes through the convection zone.

Because a subadiabatic environment is usually consider essential to ensure the amplification and storage of magnetic fields on a timescale commensurate with the magnetic cycle, current thinking places the formation and (temporary) storage site of the participating flux ropes —or, more specifically, toroidal flux rings— at or immediately beneath the interface between the convection zone, in the stably stratified but weakly subadiabatic overshoot layer (Parker, 1975; Moreno-Insertis, 1986; Choudhuri and Gilman, 1987; Fan, 2021).

Overshoot layer

Figure 1.6, taken from Ferriz-Mas et al. (1994), show the results of a stability calculation for a thin ring-shaped flux tube carrying 10^{14} Wb (10^{22} Mx) of magnetic flux, with initial magnetic strength B_0 and placed at latitude λ_0 in a very mildly subadiabatic stratification ($\delta = -2.6 \times 10^{-6}$), characteristic of the overshoot region. Important results from such simulations are:

- Non-axisymmetric buoyancy-driven instabilities of low azimutal wavenumbers are easier to excite than the axisymmetric ($m = 0$) form of the instability
- Flux tubes of magnetic strength inferior to a few Tesla (10 kG) remain stable in the overshoot region, at all latitudes and for all (reasonable) levels of subadiabacity.
- Magnetic tension stabilizes flux tubes at latitudes in excess of $\sim 70°$.
- The instability growth rate is very short as soon as the instability threshold is exceeded.

Once a flux tube is deemed unstable, its subsequent deformation and rise through the convection zone can be followed by integration of the thin flux tube equations Many such simulations have been carried out under various assumptions regarding the background stratification, flux tube properties, energetics, etc. (see, e.g., Choudhuri and Gilman, 1987; Fan et al., 1993; D'Silva and Choudhuri, 1993; Caligari et al., 1995; Fan and Fisher, 1996; Weber et al., 2013). While the thin flux tube approximation breaks down before the tubes reach the photosphere, as their diameter exceeds the rapidly decreasing scale height beyond $r/R_\odot \simeq 0.98$, their behavior and properties at that depth can

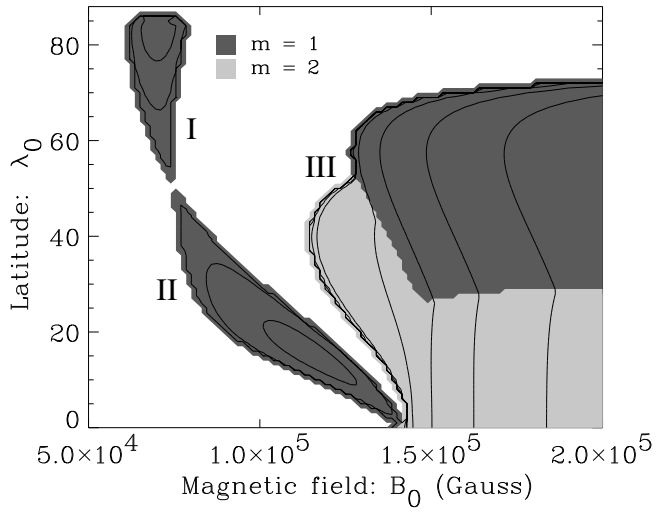

Figure 1.6: A stability diagram for magnetic flux rings located in the slightly subadiabatic fluid layers underlying the solar convection zone. The plot displays isocontour of the growth time (in days) in the latitude-field strength plane, for instability planforms of azimuthal order $m = 1$ and $m = 2$, as indicated by the gray scale. The 50 day contour intersects the abcissa at $B_0 \simeq 1.5 \times 10^5$ G. Regions left white are stable. Diagram kindly provided by A, Ferriz-Mas, used by permission.

still be compared to the patterns and properties of BMRs observed emerging in the solar photosphere. Particularly pertinent in the solar dynamo context are the following:

1. Flux tubes of magnetic strength inferior to a few Tesla (10 kG) are deflected poleward and emerge at high latitude, even if they originate from low latitudes deep in the sun;

2. Flux tubes with magnetic strength in the approximate range $4 \lesssim B \lesssim 10$ T rise almost radially, and develop a tilt with respect to the East-West direction similar to Joy's Law (more on Joy's Law immediately below).

3. Flux tubes with magnetic intensity in excess of B 10 T rise radially but emerge without a tilt.

A key quantity in understanding these patterns is the ratio of the tube's rise time to the solar rotation period (akin to an inverse Rossby number). When this ratio is of order unity or larger, the Coriolis force will strongly impact the tube's shape and rise trajectory. Not surprisingly, the rise time turns out to decrease with increasing magnetic field strength of the initial flux tube, a direct consequence of increased magnetic buoyancy.

The latitudinal dependency of Joy's law (viz. Eq. 1.62) materializes naturally in thin flux tubes simulations (see, e.g. D'Silva and Choudhuri, 1993; Caligari et al., 1995), from the action of the Coriolis force on the secondary flow developing along the rising flux tube as a consequence of angular momentum conservation (Fan et al., 1993). Here again the the tilt angle at emergence depends primarily on the field strength of the tube, and much less on its total flux.

Weber et al. (2011) (see also Weber et al., 2013) have imbedded thin flux tube simulations in a non-static background, specifically a 3D hydrodynamical numerical simulation of rotating stratified solar convection, so as to model more realistically the interaction of the rising tube with its environment. Convective entrainement markedly reduces the rise time of weakly magnetized flux tubes ($B_0 \lesssim 4\,\mathrm{T} \equiv 40\,\mathrm{kG}$, see their Fig. 8), thus avoiding their deflection to high latitudes. The observed dependence of Joy's Law on BMR field strength, including the (large) scatter about the mean tilt angle at a given latitude and field strength is also reproduced quite well (Weber et al., 2013). Interestingly, these simulations also suggest an alternate and equally plausible physical explanation for the physical origin of Joy's Law, namely the drag-mediated twist of the flux tubes by cyclonic convective upflows.

Joy's law

1.8.3 The Babcock-Leighton mechanism

Whatever its physical origin, the tilt of the magnetic axis of an emerging BMR implies a non-zero projection along the N-S direction, which amounts to a dipole moment (non-vanishing $m = 0$ terms in a spherical harmonics expansion). For a BMR of unsigned magnetic flux Φ emerging at latitude λ, with the two poles separated by an angular distance d and with a tilt angle γ with respect to the E-W direction, the dipole contribution δD is given by:

$$\delta D = \frac{3d\cos\lambda}{4\pi R^2}\Phi\sin\gamma\ . \tag{1.63}$$

Surface flux transport

Joy's law

The decay of this BMR and subsequent dispersal and transport of its magnetic flux by surface flows (as described further below) can tap into a fraction of this dipole moment and contribute to the global solar dipole. This occurs again because of Joy's Law: the leading members of each BMR pair is, at least on average, closer to the equatorial plane and thus subjected to greater cross-equatorial diffusive cancellation than the trailing member. The resulting excess of trailing magnetic polarity can then accumulate at high latitudes, as illustrated by the simple surface flux simulation (hereafter SFT) shown on Fig. 1.7. Such simulations solve the r-component of the MHD induction equation on a 2D (latitude-longitude) spherical computational corresponding to the solar photosphere. The magnetic field evolves following transport by differential rotation, poleward meridional flow, diffusion associated with small-scale convective motions, and emergence of bipolar magnetic regions (see Mackay and Yeates, 2012; Jiang et al., 2014, for reviews).

The "pedagogical" SFT simulation plotted on Fig. 1.7 is initialized (panel A) with two sets of four BMRs initially located at latitudes $\pm 15^\circ$ and equally spaced in longitude. The polarity ordering respects Hale's polarity law, and the BMR axes subtend a small angle with respect to the E-W direction (panel A), as per Joy's Law. Even though at $t = 0$ the signed flux is zero in each hemisphere (panel A), at later times (panel F) non-zero hemispheric signed flux has built up, in the form of an axisymmetric large-scale dipole. The net effect of the emergence and decay of many such BMRs is thus the production of a dipole moment (poloidal field) from decaying active regions (emerging toroidal field). This is a toroidal-to-poloidal ($T \rightarrow P$) magnetic regeneration process, known as the Babcock-Leighton mechanism, after Babcock (1961) and Leighton (1964). Together with shearing by differential rotation (§1.4), it can yield a working dynamo loop, even in the absence of turbulent induction[7]

B-L mechanism

B-L dynamo

With observed BMR emergences used instead as input, SFT simulations such as on Fig. 1.7 can reproduce quite well observed synoptic evolution of the surface magnetic field on solar cycle timescales, and generate synthetic magnetic butterfly diagrams closely resembling observations, including a good reproduction of the solar dipole's temporal evolution (DeVore et al., 1984; Wang et al., 1989; Wang and Sheeley Jr, 1991; Schrijver et al., 2002; Baumann et al., 2004; Jiang et al., 2014; Upton and Hathaway, 2014; Lemerle et al., 2015; Upton and Hathaway, 2018). Figure 1.8 shows an example spanning activity cycle 21 (1976–1986). The bottom panel is a magnetic butterfly diagram obtained by zonal averaging of the latitude-longitude computational plane of the SFT simulation. The salt-and-pepper pattern at low latitudes reflects the emergence of bipolar magnetic regions, which do not zonally average out to zero on this time-latitude diagram because of their Joy law tilt. The poleward transport of the trailing polarity shows up as slanded streaks, black (negative B_r) in the Northern hemisphere and white (positive B_r) in the South. This eventually leads to the reversal of the positive dipole of the initial condition, occuring here about 5 years after the beginning of the simulation. This is followed by the buildup of the negative dipole, peaking close near the end of the simulation at polar field strength approaching 5×10^{-4} T (5 G).

Surface flux transport

A different view of the dipole evolution is presented on the top panel, showing latitudinal profiles of the zonally-averaged surface radial magnetic field spaced 25 months apart, as color-coded. Note the steep cross-equatorial gradient in B_r building up and sustained throughout the rising and maximum phases of the sunspot cycle, a manifestation of the preferred diffusive cancellation of the leading polarity flux (DeVore et al., 1984). The reversal of the existing dipole and its subsequent buildup reflects the operation of he Babcock-Leighton mech-

B-L mechanism

[7]The conceptual similarities and differences between the mean-field α-effect (§1.6) and the Babcock-Leighton mechanism are worth reflecting upon: in the former, a small-scale cyclonic flow twists individual toroidal magnetic fieldlines into meridional planes, and turbulent diffusion then merges these small-scale loops into a large-scale poloidal field; in the latter, the Coriolis force and/or large cyclonic convective cells twist a buoyantly rising toroidal flux ring —a large-scale magnetic object— out of the $[r, \phi]$ plane, and following emergence and decay, diffusion and surface flows build a large-scale dipole. In both cases, the Coriolis force is the ultimate culprit.

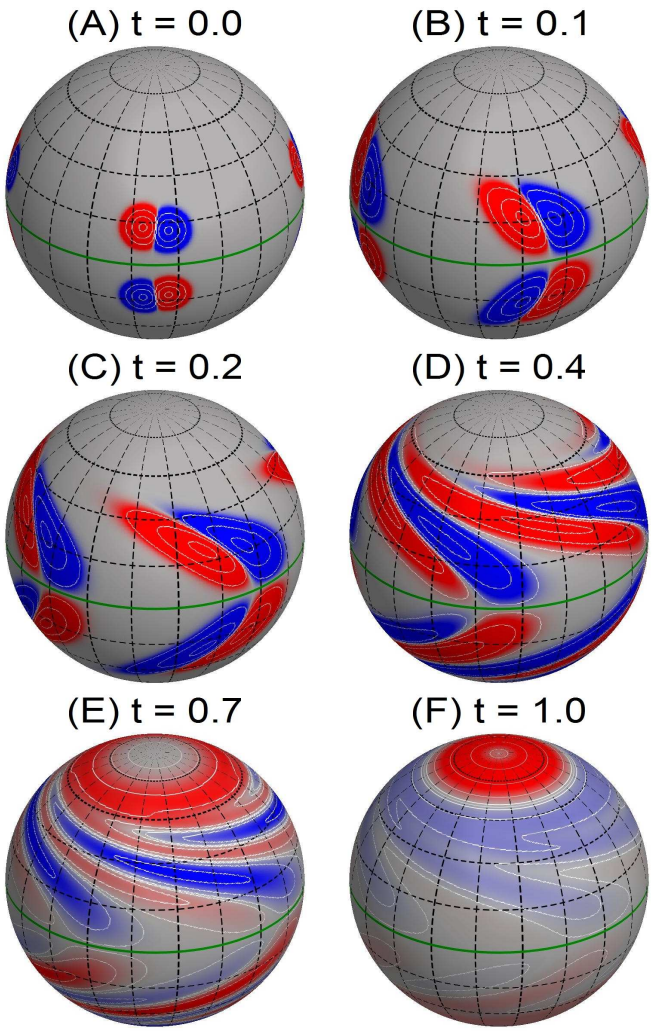

Figure 1.7: A pedagogical surface flux transport simulation. Diffusion and shearing by surface differential rotation inexorably distorts the surface field distribution, with the trailing polarity accumulating at the poles in response to the poleward-directed meridional flow. Note that for visualization purposes, each BMR's initial surface areas in (A) is unrealistically large, and the peak surface field strength is normalized to unity in each frame. Time is given in units of the turnover time of the meridional flow.

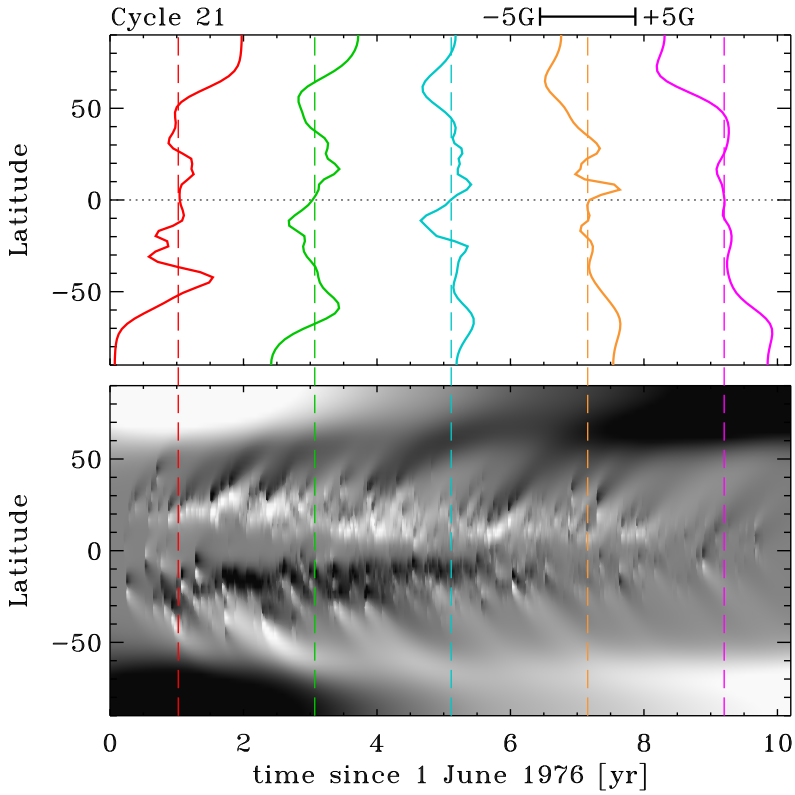

Figure 1.8: A simulation of solar surface magnetic flux evolution showing the Babcock-Leighton mechanism in action, in response to emergence of bipolar magnetic regions in the course of activity cycle 21 (1976–1986). The bottom panel shows the corresponding magnetic butterfly diagram, with the vertical lines flagging the five times at which the temporal cuts are plotted on the top panel. The grayscale is saturated at ± 5 G to better emphasize the poleward transport at mid-latitudes. Surface flux evolution simulation taken from Lemerle et al. (2015), using as input the cycle 21 active region emergence database of Wang and Sheeley (1989).

anism.

In such simulations the bulk of the initial magnetic flux undergoes diffusive cancellation, and only a minute fraction accumulates at the pole. In the solar context, however, this is not problematic. The solar polar cap magnetic flux adds up to $\sim 10^{14}$ Wb, which is about the unsigned flux contained in one large bipolar magnetic regions. About 10^{17} Wb (10^{25} Mx) of magnetic flux emerges in such active regions in the course of a typical activity cycle so the toroidal-to-poloidal flux conversion efficiency required of the Babcock-Leighton mechanim is in fact quite low.

The important take-home message is: the Babcock-Leighton mechanism is observed operating at the solar surface, and so is very well-constrained observationally. The key question, in the solar cycle context, is whether it is a crucial component of the dynamo loop, or represents a mere side-effect of a dynamo operating independently in the solar interior. This question will be revisited in my second lecture.

1.9 Summary

1. The spatiotemporal evolution of magnetic fields in the solar interior and extended atmosphere is well-described by magnetohydrodynamics;

2. In the solar interior and atmosphere, for all but the smallest spatial scales the magnetic Reynolds number is very high so that flux freezing holds;

3. A flow is deemed a dynamo if its inductive action can amplify and sustain the magnetic field against Ohmic dissipation;

4. Dynamo tap into the kinetic energy of the inductive flows via the work done against the Lorentz force;

5. Small-scale dynamos generate magnetic fields on scales comparable or smaller than those of the inductive flow, but no magnetic flux on larger scales;

6. Large-scale dynamos generate net magnetic flux on spatial and temporal scales larger than those of the inductive flows.

7. Many distinct inductive effects can potentially contribute to the regeneration of the solar magnetic field: shearing by differential rotation, cyclonic turbulence in the convection zone, surface decay of active regions, and assorted MHD instabilities in the tachocline and/or outer reaches of the radiative core;

8. Magnetic buoyancy is the primary driver of magnetic flux emergence from the solar interior.

Chapter 2

Dynamo models of the solar cycle

It is imperative to open this lecture with a simple and sobering fact: we currently do not have a concensus dynamo model for the solar cycle. Even the physical origin of some rather basic features is not yet settled; for example what process(es) set the cycle period, regulate its amplitude, or drive the equatorward progression of surface activity in the course of a cycle; but at least the starting point is generally agreed upon: the solar cycle is powered by the inductive action of flows in the solar interior, and under solar/stellar interior conditions this dynamo process is well described by the magnetohydrodynamical induction equation (1.5).

The aim of this lecture is to describe the construction of dynamo models of the solar cycle, and review their general features and properties. Here "solar cycle model" is to be understood as a physically and/or geometrically simplified mathematical/physical/computational construct that can describe —and perhaps predict— the observed spatiotemporal evolution of the large-scale solar magnetic field.

2.1 The magnetic solar cycle

The various manifestations of the solar magnetic activity cycle, and their associated temporal variations, are discussed at length in the Lectures by Theodosios Chatzistergos. Sunspots are the best known tracer of the magnetic cycle. They appear when deep-seated toroidal flux ropes rise through the convective envelope and emerge at the photosphere (Parker, 1955, 1975; Fan, 2021). Assuming that they rise radially and are formed where the magnetic field is the strongest, the sunspot butterfly diagram can be interpreted as a spatio-temporal "map" of the Sun's internal, large-scale toroidal magnetic field component.

Figure 2.1 is a magnetic butterfly diagram of the surface radial component of the solar magnetic field. The global magnetic polarity reversal on a $\approx 11\,\mathrm{yr}$ pe-

riod is quite obvious. The imprint of the sunspot butterfly diagram is visible at low latitudes ($\lesssim 35°$). At high latitudes a surface dipole pattern is also present, reversing polarity at times of sunspot maximum. Note also the poleward drift of the surface fields, away from sunspot latitudes. This pattern is believed to originate from the transport of magnetic flux released by the decay of sunspots at low latitudes [1]

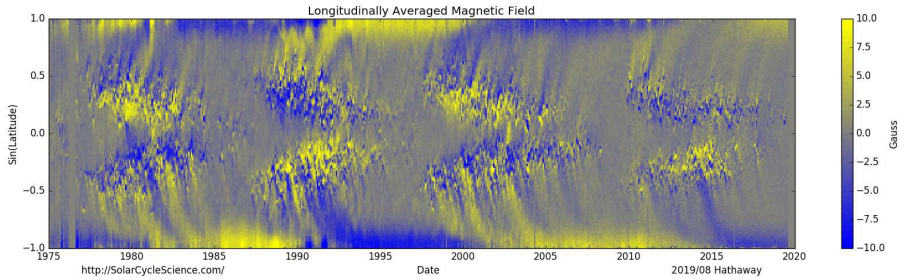

Figure 2.1: Zonally-averaged time-latitude magnetogram of the radial component of the solar surface magnetic field. The low-latitude component is associated with sunspots. Note the polarity reversal of the high-latitude magnetic field, occurring approximately at time of sunspot maximum (courtesy of D. Hathaway, Solar Cycle Science; see `http://solarcyclescience.com/bin/magbfly.png`).

In the solar cycle context, the dynamo problem is reformulated towards identifying the circumstances under which the flow fields observed and/or inferred in the Sun can sustain the cyclic regeneration of the magnetic field associated with the observed solar cycle. This involves more than merely sustaining the field. A model of the solar dynamo should also reproduce:

- cyclic polarity reversals with a decadal half-period,
- low-latitude confinement and equatorward migration of the sunspot-generating deep toroidal field and its inferred strength,
- poleward migration of the diffuse surface field,
- observed $\pi/2$ phase lag between poloidal and toroidal components,
- peak surface polar field strength of order $\sim 10^{-3}$ T (10 G),
- observed antisymmetric equatorial parity,
- predominantly negative (positive) magnetic helicity in the Northern (Southern) solar hemisphere.

[1] for alternate viewpoints, see Petrovay and Szakály (1999); Ulrich and Tran (2013).

At the next level of "sophistication", a solar dynamo model should also be able to exhibit amplitude fluctuations, and reproduce (at least qualitatively) the empirical patterns and correlations extracted from the sunspot and proxy records, including the so-called Grand Minima, during which the cycle amplitude –and perhaps the cycle itself– is strongly suppressed over many cycle periods One should finally add to the list torsional oscillations in the convective envelope, with proper amplitude and phasing with respect to the magnetic cycle. All this adds up to a very tall order by any standard.

2.2 Kinematic axisymmetric dynamo models

Because of the great disparity of time- and length scales involved, and the fact that the outer 30% in radius of the Sun are the seat of vigorous, thermally-driven turbulent convective fluid motions, the solar dynamo problem is very hard to tackle as a direct numerical simulation of the full set of MHD equations (but do see Sect. 2.7 below). Most solar dynamo modelling work has thus relied on simplification – usually drastic – of the MHD equations, as well as assumptions on the structure of the Sun's magnetic field and internal flows.

Two drastic yet (it turns out) reasonable and common assumptions are:

1. **kinematic approximation**: the large-scale flow field $\mathbf{u}$ is considered given and steady.

2. **axisymmetric approximation**: the large-scale magnetic field associated with the magnetic cycle is considered axisymmetric ($\partial/\partial\phi = 0$ in spherical polar coordinates).

To a good first approximation, the kinematic approximation is well-supported by solar observations: Helioseismology (Christensen-Dalsgaard, 2002) has pinned down with good accuracy the two dynamo-relevant solar large-scale flow components, namely differential rotation throughout the interior, and meridional circulation in the outer half of the solar convection zone (for reviews, see Gizon, 2004; Howe, 2009), with cycle-related variations (torsional oscillations) being of very low amplitude, a few percent.

Also to a good first approximation, axisymmetry on large scales ($\approx R_\odot$) is supported by the sunspot butterfly diagram, Hale's polarity law, synoptic magnetograms, and the shape of the solar corona at and around solar activity minimum. These observations also indicate that the large-scale solar magnetic field has its symmetry axis coincident with the rotation axis (unlike for Earth's magnetic field).

2.2.1 Mathematical formulation

Under axisymmetry, it is convenient to express the large-scale field as the sum of a toroidal (i.e., longitudinal) component and a poloidal component (i.e., contained in meridional planes), the latter being expressed in terms of a toroidal

vector potential. This is the same mathematical approach used earlier in establishing Cowling's theorem (§1.5) Working in spherical polar coordinates (r, θ, ϕ), one writes again

$$\mathbf{B}(r,\theta,t) = \nabla \times (A(r,\theta,t)\hat{\mathbf{e}}_\phi) + B(r,\theta,t)\hat{\mathbf{e}}_\phi. \tag{2.1}$$

Likewise, the (steady) large-scale flow field $\mathbf{u}$ is written as the sum of an axisymmetric azimuthal component (differential rotation), and an axisymmetric "poloidal" component $\mathbf{u}_p$ ($\equiv u_r(r,\theta)\hat{\mathbf{e}}_r + u_\theta(r,\theta)\hat{\mathbf{e}}_\theta$), i.e., a flow confined to meridional planes:

$$\mathbf{u}(r,\theta) = \mathbf{u}_p(r,\theta) + \varpi\Omega(r,\theta)\hat{\mathbf{e}}_\phi \ , \tag{2.2}$$

where $\varpi = r\sin\theta$ and Ω is the angular velocity (rad s^{-1}). Substitution of (2.1) and (2.2) into the MHD induction equation (1.5) yields two separate (but coupled) evolution equations for A and B:

$$\frac{\partial A}{\partial t} = \underbrace{\eta\left(\nabla^2 - \frac{1}{\varpi^2}\right)A}_{\text{resistive decay}} - \underbrace{\frac{\mathbf{u}_\mathrm{p}}{\varpi}\cdot\nabla(\varpi A)}_{\text{transport}}, \tag{2.3}$$

$$\begin{aligned}\frac{\partial B}{\partial t} &= \underbrace{\eta\left(\nabla^2 - \frac{1}{\varpi^2}\right)B + \frac{1}{\varpi}\frac{\partial(\varpi B)}{\partial r}\frac{\partial \eta}{\partial r}}_{\text{resistive decay}} - \underbrace{\varpi\mathbf{u}_\mathrm{p}\cdot\nabla\left(\frac{B}{\varpi}\right)}_{\text{transport}} \\ &- \underbrace{B\nabla\cdot\mathbf{u}_\mathrm{p}}_{\text{compression}} + \underbrace{\varpi(\nabla\times(A\hat{\mathbf{e}}_\phi))\cdot\nabla\Omega}_{\text{shearing}}.\end{aligned} \tag{2.4}$$

where, in anticipation of later developments, the magnetic diffusivity may depend on radius inside the sun.

Once augmented with suitable additional source terms, Eqs. (2.3)–(2.4) will become our model axisymmetric dynamo equations. They are to be solved in a meridional plane, i.e., $R_\mathrm{i} \le r \le R_\odot$ and $0 \le \theta \le \pi$, with regularity of the solutions requiring that $A = 0$ and $B = 0$ on the symmetry axis. It is usually assumed that the deep radiative interior can be treated as a perfect conductor, so that one sets $A = 0$ and $\partial(rB)/\partial r = 0$ at some depth R_i chosen deeper than the lowest extent of the region where dynamo action is taking place. It is usually assumed that the Sun/star is surrounded by a vacuum, in which no electrical currents can flow, i.e., $\nabla\times\mathbf{B} = 0$; such an axisymmetric potential field, expressed via Equation (2.1), then requires

$$\left(\nabla^2 - \varpi^2\right)A = 0, \qquad B = 0, \qquad r/R_\odot > 1, \tag{2.5}$$

Formulated in this manner, the dynamo solution spontaneously "picks" its own parity, i.e., its symmetry with respect to the equatorial plane. Alternately, one may solve only in a meridional *quadrant* ($0 \le \theta \le \pi/2$) and *impose* equatorial parity via the boundary condition at the equatorial plane ($\theta = \pi/2$):

$$\frac{\partial A}{\partial \theta} = 0, \qquad B = 0 \qquad \rightarrow \text{ antisymmetric}, \tag{2.6}$$

$$A = 0, \qquad \frac{\partial B}{\partial \theta} = 0 \qquad \rightarrow \text{ symmetric}. \tag{2.7}$$

2.2.2 Model ingredients

All kinematic solar dynamo models discussed in what follows have some basic "ingredients" in common. Unless noted otherwise, all illustrative models discussed below are computed using the following analytic formulae for the angular velocity $\Omega(r,\theta)$ and magnetic diffusivity $\eta(r)$:

$$\frac{\Omega(r,\theta)}{\Omega_{\rm E}} = \Omega_{\rm C} + \frac{\Omega_{\rm S}(\theta) - \Omega_{\rm C}}{2}\left[1 + \mathrm{erf}\left(\frac{r - r_{\rm c}}{w}\right)\right], \tag{2.8}$$

with

$$\Omega_{\rm S}(\theta) = 1 - a_2\cos^2\theta - a_4\cos^4\theta, \tag{2.9}$$

and

$$\frac{\eta(r)}{\eta_T} = \Delta\eta + \frac{1-\Delta\eta}{2}\left[1 + \mathrm{erf}\left(\frac{r - r_{\rm c}}{w}\right)\right]. \tag{2.10}$$

With appropriately chosen parameter values, Equation (2.8) describes a solar-like differential rotation profile, namely a purely latitudinal differential rotation in the convective envelope, with equatorial acceleration and smoothly matching a core rotating rigidly at the angular speed of the surface mid-latitudes[2]. This rotational transition takes place across a tachocline, of half-thickness w coinciding with the core-envelope interface at $r_{\rm c}/R_\odot = 0.7$ (see Fig. 2.2B, with parameter values listed in caption). As per Eq. (2.10), a similar transition takes place with the net diffusivity, falling from some large, "turbulent" value η_T in the envelope to a much smaller diffusivity $\eta_{\rm c}$ in the convection-free radiative core, the diffusivity contrast being given by $\Delta\eta = \eta_{\rm c}/\eta_T$. Given helioseismic constraints, these represent minimal yet reasonably realistic choices[3].

Differential rotation

Magnetic diffusivity

This idealized solar-like differential rotation profile is still quite complex, in that it is characterized by *three* partially overlapping shear regions:

- a strong positive radial shear in the equatorial regions of the tachocline,
- an even stronger negative radial shear in its the polar regions,
- a significant latitudinal shear throughout the convective envelope and extending partway into the tachocline.

For a tachocline of half-thickness $w/R_\odot = 0.05$, the mid-latitude latitudinal shear at $r/R_\odot = 0.7$ is comparable in magnitude to the equatorial radial shear; its potential contribution to dynamo action should not be casually dismissed.

Meridional circulation is as unavoidable as differential rotation in turbulent, compressible rotating convective shells (see Featherstone and Miesch, 2015, and references therein). The convenient parametric form developed by van Bal-

Medridional circulation

[2]Belvedere et al. (2000) presents an alternate analytic expression that is even closer to helioseismic inversions.

[3]Helioseismology has also revealed the existence of a significant radial shear in the outermost layers of the solar convective envelope. Even if the storage problem could be somehow bypassed, it does not appear possible to construct a viable solar dynamo model relying exclusively on this angular velocity gradient (see, e.g., Dikpati et al., 2002; Brandenburg, 2005; Pipin and Kosovichev, 2011a, for illustrative calculations).

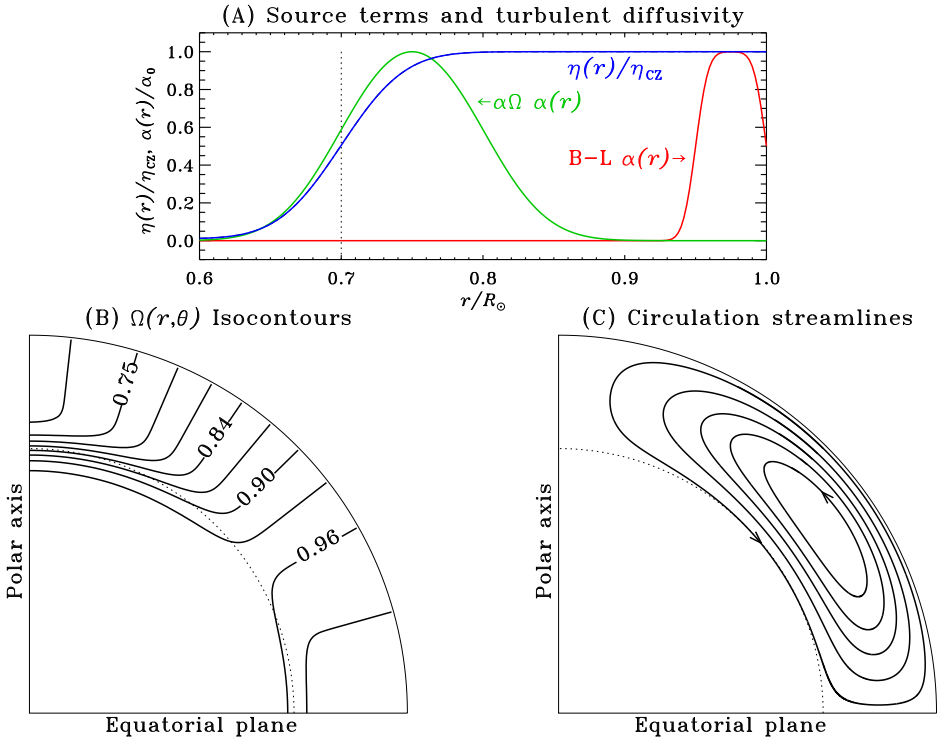

Figure 2.2: Common ingredients to the mean-field and mean-field-like dynamo models discussed in the following sections. Panel (B) shows the run of net magnetic diffusivity (blue) with depth, as described by Eq. (2.10), with parameter values $r_c/R_\odot = 0.7$ and $w/R_\odot = 0.05$. The red and green profiles refer to the depth dependency of the poloidal source terms introduced in Sects. 2.3 and 2.4, and 2.5, respectively. Panel (B) shows isocontours of angular velocity normalized to the surface equatorial value, as generated by Equation (2.8) with parameter values $\Omega_C = 0.8752$, $a_2 = 0.1264$, $a_4 = 0.1591$. The radial shear changes sign at colatitude $\theta = 55°$ at the core-envelope interface (dotted line on all panels). Panel (C) depicts streamlines of the meridional flow, from the model of van Ballegooijen and Choudhuri (1988), with parameter values $m = 0.5$, $p = 0.25$, $q = 0$, and $r_b = 0.675$.

legooijen and Choudhuri (1988) is used in all forthcoming illustrative models including meridional circulation (Sects. 2.4 and 2.5). This "minimal" parameterization defines a steady quadrupolar circulation pattern, with a single flow cell per quadrant extending from the surface down to a depth r_b. Circulation streamlines are shown in Fig. 2.2C; the flow is poleward in the outer convection zone, with an equatorial return flow peaking slightly above the core-envelope interface, and rapidly vanishing below. This is consistent with the latest helioseismic inversions (see Gizon et al., 2020).

2.3 Mean-field dynamo models

We now add the mean-electromotive force (§1.6.1) to Eqs. (2.3)–2.4), under the assumption of isotropy so that $\boldsymbol{\xi} = \alpha\langle\mathbf{B}\rangle + \beta\nabla\times\langle\mathbf{B}\rangle$. This leads to the following form for the adimentional axisymmetric mean-field dynamo equations:

$$\frac{\partial A}{\partial t} = \underbrace{-\frac{\mathrm{Rm}}{\varpi}(\mathbf{u}_p\cdot\nabla)(\varpi A)}_{\text{advection}} + \underbrace{\eta\left(\nabla^2 - \frac{1}{\varpi^2}\right)A}_{\text{dissipation}} + \underbrace{C_\alpha\xi_\phi}_{\alpha\text{ effect}} \tag{2.11}$$

$$\begin{aligned}\frac{\partial B}{\partial t} &= -\mathrm{Rm}\left[\underbrace{\varpi(\mathbf{u}_p\cdot\nabla)\left(\frac{B}{\varpi}\right)}_{\text{advection}} - \underbrace{(\nabla\cdot\mathbf{u}_p)B}_{\text{compression}}\right] + \underbrace{\eta\left(\nabla^2 - \frac{1}{\varpi^2}\right)B + \frac{1}{\varpi}\frac{\mathrm{d}\eta}{\mathrm{d}r}\frac{\partial(\varpi B)}{\partial r}}_{\text{dissipation}} \\ &+ \underbrace{C_\Omega\varpi(\nabla\times A\hat{\mathbf{e}}_\phi)\cdot\nabla\Omega}_{\text{shearing}} + \underbrace{C_\alpha\nabla\times(\xi_r\hat{\mathbf{e}}_r + \xi_\theta\hat{\mathbf{e}}_\theta)}_{\alpha\text{ effect}}\end{aligned} \tag{2.12}$$

Note how the α-term is the only inductive contribution appearing on the RHS of (2.11), allowing the regeneration of the large-scale poloidal magnetic component and thus evading Cowling's theorem The above dimensionless forms are produced by expressing time in units of the (turbulent) magnetic diffusion time R^2/η_0, with R the solar radius, used to scale lengths. Three dimensionless groupings now appear in these dimensionless dynamo equations:

Cowling's theorem

$$C_\alpha = \frac{\alpha_0 R}{\eta_0}\ , \tag{2.13}$$

$$C_\Omega = \frac{\Omega_0 R^2}{\eta_0}\ , \tag{2.14}$$

$$\mathrm{Rm} = \frac{u_0 R}{\eta_0}\ , \tag{2.15}$$

where α_0, η_0, Ω_0 and u_0 are representative values for the magnitudes of the α-effect, turbulent diffusivity, rotational shear and meridional flow speed, respectively. The first two are dynamo numbers associated with the α-effect and

Dynamo number

rotational shearing, while the third is a magnetic Reynolds number measuring the relative importance of the meridional flow versus diffusion in transporting the magnetic field in meridional planes.

Estimates based on the mixing-length model of convection as well as measurements in MHD simulations (viz. Fig. 2.13A–C) indicate α_0 being of the order of a few $\mathrm{m\,s^{-1}}$ which, for $\Omega_0 \sim 10^{-6}\,\mathrm{rad\,s^{-1}}$ and $R = 7\times10^8\,\mathrm{m}$, yields $C_\alpha/C_\Omega \simeq 10^{-3} \ll 1$, independently of the poorly constrained value of η_0. On this basis the terms involving α on the RHS of Eq. (2.12) are often set to zero, yielding the $\alpha\Omega$ *dynamo model*, effectively retaining only the $\alpha_{\phi\phi}$ component of the full $\boldsymbol{\alpha}$-tensor. The net dynamo number, setting the growth rate of the dynamo solutions in the linear regime (viz. §1.6.3) is then given by $D = C_\alpha \times C_\Omega$.

$\alpha\Omega$ dynamo

Dynamo number

If on the other hand the shearing term ($\propto \nabla\Omega$) is neglected, one obtains the purely turbulent α^2 *dynamo model*, encountered already in §1.6.3. Such models are relevant to dynamo action in planetary cores and convective stars with vanishing differential rotation (if such an object were to exist).

α^2 dynamo

Retaining both inductive contribution on the RHS of (2.12) yields the more general $\alpha^2\Omega$ *dynamo model*. Mean-field analysis of many global MHD simulations (discussed in upcoming §2.7.2) producing large-scale cycling magnetic fields suggests that these simulations operate in this regime (Racine et al., 2011; Augustson et al., 2015; Simard et al., 2016; Warnecke et al., 2018).

$\alpha^2\Omega$ dynamo

2.3.1 Linear solutions as eigenvalue problems

With the large-scale flows, turbulent diffusivity and α-effect considered given, Equations (2.11, 2.12) become truly linear in A and B. It becomes possible to seek eigensolutions in the form

$$A(r,\theta,t) = a(r,\theta)\exp(st), \qquad B(r,\theta,t) = b(r,\theta)\exp(st), \tag{2.16}$$

with $s = \sigma + i\omega$. Substitution of these expressions into Equations (2.11, 2.12) yields an eigenvalue problem for s and associated eigenfunction $\{a, b\}$. The real part σ of the eigenvalue is then a growth rate, and the imaginary part ω an oscillation frequency. One typically finds that $\sigma < 0$ until the total dynamo number

$$D \equiv C_\alpha \times C_\Omega\ , \tag{2.17}$$

exceeds a critical value D_{crit} beyond which $\sigma > 0$, corresponding to a growing solutions (cf. §1.6.3). Such solutions are said to be *supercritical*, while the solution with $\sigma = 0$ is *critical*. A dynamo solution is considered weakly supercritical if its dynamo number only slightly exceeds D_{crit}; cyclic solution exhibiting polarity reversals require $\omega \neq 0$. In the weakly supercritical regime such cyclic solutions typically have $\sigma \ll \omega$, while $\sigma \gg \omega$ in the strongly supercritical regime.

Critical dynamo number

Figure 2.3 shows variation of the dynamo growth rate and frequency for four distinct sequences of linear $\alpha\Omega$ eigensolutions. All sequences use the model ingredients of Fig. 2.2, with the minimal dependency $\alpha \propto \cos\theta$ and omit the meridional flow, i.e., $\mathbf{u}_p = 0$ is set in eqs. (2.11)–(2.12). The four sequences differ

only in the sign of the α-effect and in the parity imposed via the equatorial plane boundary condition, as labeled. Some noteworthy characteristics are:

- Both the growth rate and cycle frequency increases with the total dynamo number D
- The growth rates and frequency are nearly independent of equatorial parity.
- The critical dynamo number ($\sigma = 0$) and dynamo frequency are ony weakly dependent on the sign of the dynamo number.

These characteristics carry over to other kinematic $\alpha\Omega$ model setups as well (see, e.g. Stix, 1976).

Figure 2.4 shows four eigenfunction snapshots of the $C_\alpha = +5$ equatorially antisymmetric solution of Fig. 2.3, spanning half a magnetic cycle, i.e., the $\varphi = \pi$ snapshot is identical to $\varphi = 0$ except for opposite magnetic polarities for both toroidal and poloidal components. Note that:

- The eigenfunction peak at mid-latitudes at the base of the convective envelope (dashed circular arc), a direct consequence of the $\propto \cos\theta$ dependence for the α-effect, and that both the radial shear and α-effect also peak at the core-envelope interface (viz. Fig. 2.2).
- The ratio of poloidal-to-toroidal field strength, in turn, is found to scale as some power (usually close to 1/2) of the ratio C_α/C_Ω, at a fixed value of the product $C_\alpha \times C_\Omega$.
- The phase difference between the poloidal and toroidal components is $\pm\pi/2$, according to the sign of the product $C_\alpha \times C_\Omega$ (see, e.g. Stix, 1976).

2.3.2 Dynamo waves

One of the most remarkable property of the $\alpha\Omega$ dynamo model is that it supports travelling wave solutions, as a careful examination of Fig. 2.4 reveals. This was first demonstrated in Cartesian geometry by Parker (1955) (as detailed in Appendix A), who proposed that a latitudinally-travelling "dynamo wave" was at the origin of the observed equatorward drift of sunspot emergences in the course of the cycle. This finding was subsequently shown to hold in spherical geometry, as well as for non-linear models (Yoshimura, 1975; Stix, 1976). Dynamo waves [4] travel in a direction $\mathbf{s}$ given by

Dynamo wave

$$\mathbf{s} = \alpha\nabla\Omega \times \hat{\mathbf{e}}_\phi, \tag{2.18}$$

a result now known as the "Parker-Stix-Yoshimura sign rule". For the linear $\alpha\Omega$ dynamo solution of Fig. 2.4, the α-effect is positive in the Northern hemisphere and the angular velocity gradient is negative in the high latitude tachocline, so that the above expression predicts latitudinal propagation towards the equator.

[4] These are not "waves" in usual sense of the word, although they are described by modal solutions of the form $\exp(i\mathbf{k}\cdot\mathbf{x} - \omega t)$; wave-like propagation results from a spatial offset between source and dissipation.

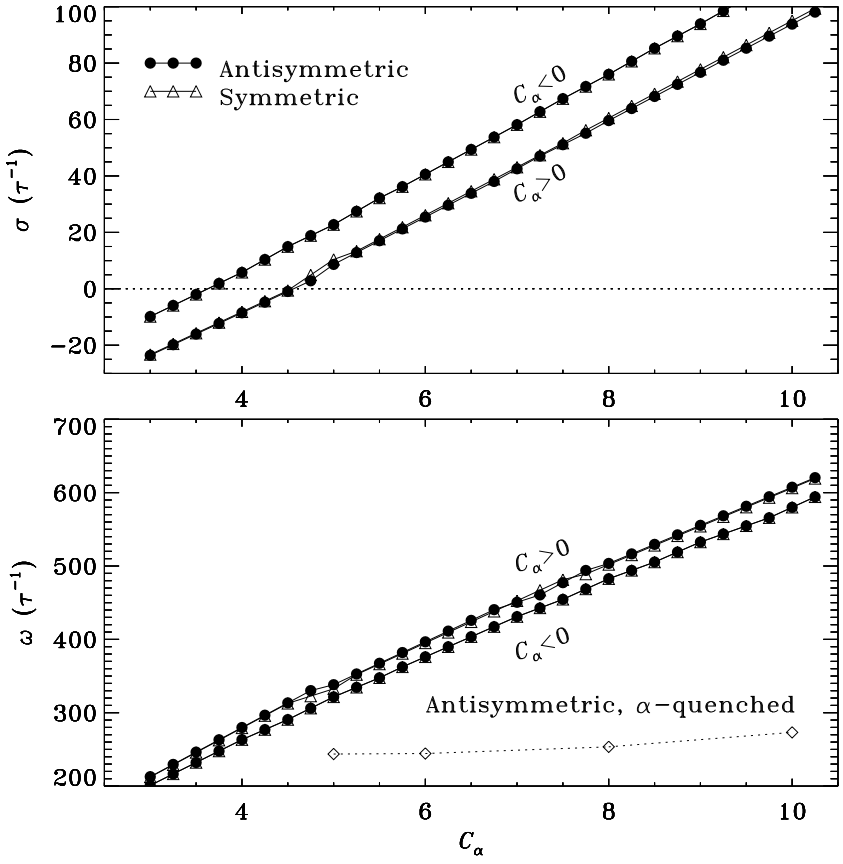

Figure 2.3: Growth rates (top) and frequency (bottom) versus dynamo number C_α for sequences of linear kinematic axisymmetric $\alpha\Omega$ dynamo solutions, with positive or negative dynamo number and fixed equatorial parity, as labeled. Model ingredients as on Fig. 2.2, and parameter values $C_\Omega = 2.5 \times 10^4$, and $\eta_0 = 5 \times 10^7\,\mathrm{m^2\,s^{-1}}$, (leading to $\tau \simeq 300\,\mathrm{yr}$). Exponentially growing dynamo modes have $\sigma > 0$. The first mode to reach criticality is the negative C_α mode, at $D_{\rm crit} = -0.9 \times 10^5$, almost independently of equatorial parity. The positive-C_α mode becomes critical at $D_{\rm crit} = 1.1 \times 10^5$. Diamonds in the bottom panel give the cycle frequency in α-quenched but otherwise identical model (see §2.3.3 below).

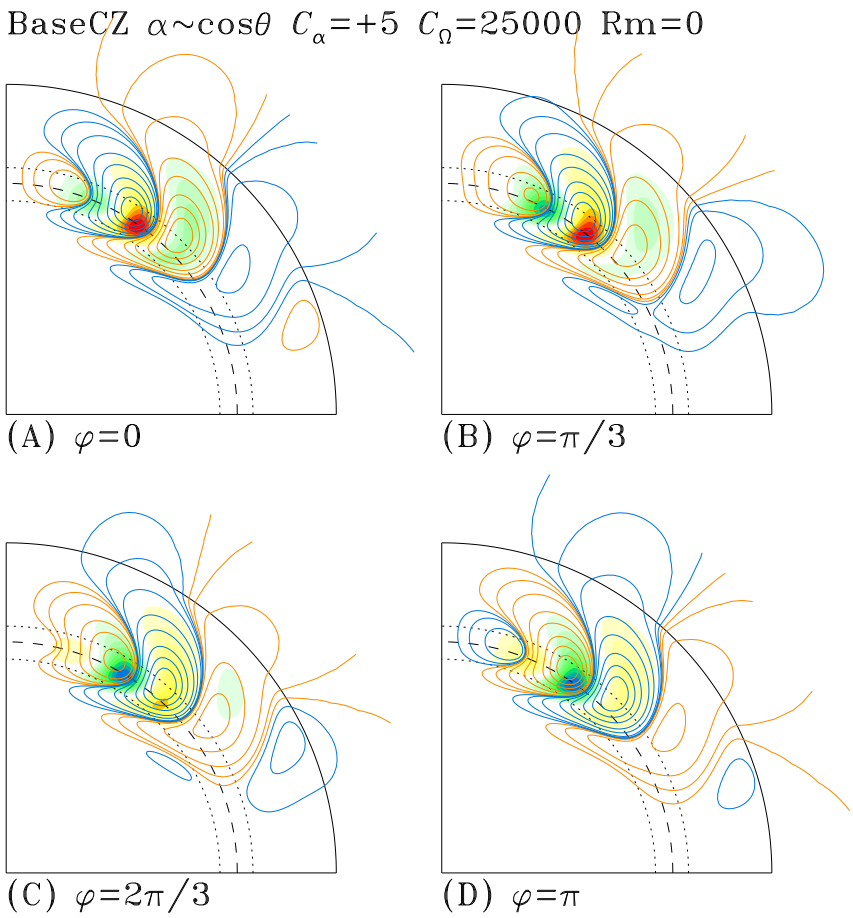

Figure 2.4: Four meridional plane snapshots of a mildly supercritical linear $\alpha\Omega$ dynamo solution, spanning half a magnetic cycle and with exponential growth removed. The defining parameters are $C_\Omega = 25000$, $C_\alpha = +5$, and $\mathrm{Rm} = 0$ (no meridional flow). The toroidal field is rendered in color (green to blue for negative B, yellow to red for positive B). Poloidal fieldlines are superimposed (blue for clockwise orientation, orange for counterclockwise). The dashed circular arc indicates the base of the convection zone at $r/R = 0.7$, and the dotted arcs give the width of the transition layer for η and Ω (see Fig. 2.2). The polar axis coincides with the left quadrant boundary. An animation of this solution is available on the web page complementing these lecture notes.

2.3.3 Nonlinear solutions: α-quenching

Exponential growth of the large-scale magnetic cannot perdure indefinitely. Magnetic tension will increasingly resist deformation by the small-scale turbulent fluid motions. This should then leads to a reduction of the α-effect, and eventual saturation of the dynamo-generated magnetic field amplitude, the dynamo number being effectively reduced to its critical value. This is called α-quenching.

One may thus expect that α-quenching sets in when the growing dynamo-generated mean magnetic field reaches a magnitude such that its energy per unit volume is comparable to the kinetic energy of the underlying turbulent fluid motions:

$$\frac{\langle \mathbf{B} \rangle^2}{8\pi} = \frac{1}{2} \varrho (\mathbf{u}')^2 \ . \tag{2.19}$$

Equipartition field strength

Denoting the corresponding *equipartition field strength* by $B_{\rm eq}$, one often introduces an *ad hoc* nonlinear dependency of α directly on the mean-field $\langle \mathbf{B} \rangle$ by writing:

$$\alpha \to \alpha(\langle \mathbf{B} \rangle) = \frac{\alpha_0}{1 + (\langle \mathbf{B} \rangle / B_{\rm eq})^2} \ . \tag{2.20}$$

α-quenching

This algebraic quenching expression "does the right thing", in that $\alpha \to 0$ as $\langle \mathbf{B} \rangle$ grows beyond $B_{\rm eq}$. It remains an extreme oversimplification of the complex interaction between flow and field that characterizes MHD turbulence, but its wide usage in solar dynamo modeling makes it a nonlinearity of choice for the illustrative purpose of this lecture[5].

A useful quantity to monitor in order to ascertain saturation is the total magnetic energy, integrated over the computational domain:

$$\mathcal{E}_{\rm B} = \frac{1}{8\pi} \int_V \langle \mathbf{B} \rangle^2 \, {\rm d}V. \tag{2.21}$$

Figure 2.5 shows time series of this quantity in a sequence of α-quenched kinematic $\alpha\Omega$ mean-field dynamo solutions, otherwise identical to the antisymmetric, positive C_α linear solutions of Fig. 2.3. The four solutions have increasing values for the dynamo number D, and all start from the same initial condition of very weak magnetic field.

The linear phase of exponential growth (gray lines), with growth rate increasing with D, is followed by saturation at an energy level also increasing with D; these are behaviors typical of α-quenched mean-field and mean-field-like dynamo models operating not too far in the supercritical regime. Here α-quenching has had the desired effect, namely stabilizing the cycle amplitude at field strengths corresponding to a significant fraction of the equipartition value $B_{\rm eq}$ introduced in the quenching parametrization (2.20). In contrast, for subcritical solutions ($D/D_{\rm crit} < 1$), the magnetic field decays exponentially to zero whatever the initial condition might be.

[5] Analyses of various MHD numerical simulations do support to some extent the general idea of α-quenching (e.g., Brandenburg et al., 2008; Karak et al., 2014; Simard et al., 2016).

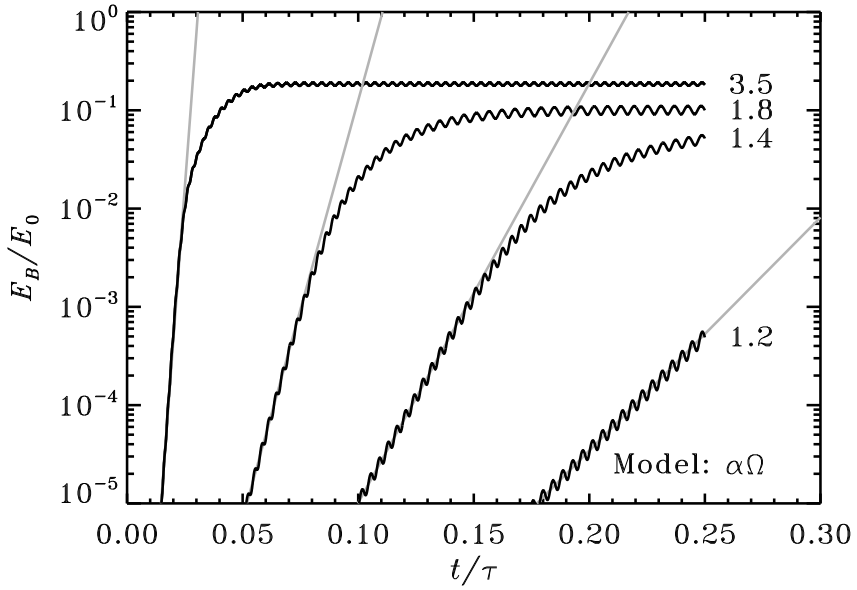

Figure 2.5: Time series of total magnetic energy in an α-quenched kinematic axisymmetric $\alpha\Omega$ mean-field dynamo model, for increasing values of the dynamo number scaled to its critical value ($D/D_{\rm crit}$), as labeled. Magnetic energy is scaled to the corresponding equipartition field strength $B_{\rm eq}$ in Eq. (2.20), via Eq. (1.23). All solutions are initialized with a purely toroidal magnetic field of very low amplitude. The gray lines indicate the linear phase, during which the magnetic amplitude grows exponentially at a rate increasing with the dynamo number. In the nonlinearly saturated phase that is eventually established, the overall magnetic cycle amplitude increases with increasing value of the dynamo number.

2.3.4 Cycle period and butterfly diagram

In such nonlinearly saturated models the cycle frequency shows reduced sensitivity to D and becomes equal to some approximately fixed fraction of the magnetic diffusion time (1.12), as indicated by the diamonds and dotted line on the bottom panel of Fig. 2.3. The primary determinant of the (dimensional) period then becomes the adopted value for the turbulent diffusivity. Although model dependent to some extent, decadal periods typically require 10^8 to $10^9\,{\rm m}^2\,{\rm s}^{-1}$, roughly consistent with estimates from mixing length models of convective energy transport; values lower by a factors of ~ 10 are required for dynamos contained in radially thin layers, because the smaller radial length scale enhances dissipation. Similarly low values are also possible (and in fact expected) in the upper tachocline, where residual turbulent diffusivity presumably results

from convective overshoot.

Figure 2.6 shows time-latitude diagrams of the toroidal field extracted at the core-envelope interface, here $r/R_\odot = 0.7$. If sunspot-producing toroidal flux ropes form in regions of peak toroidal field strength, and if those ropes rise radially to the surface, then such diagrams are directly comparable to the sunspot butterfly diagram.

The top panel is an α-quenched cousin of the linear solution shown on Fig. 2.4, while in the bottom two panels the α-effect has been artificilly concentrated towards the equator through an assumed latitudinal dependency $\propto \sin^2\theta\cos\theta$. With an eye on Fig. 2.2B, notice also how the dynamo waves propagates along isocontours of angular velocity, in agreement with the Parker–Yoshimura sign rule (cf. Sect. 2.3.2). Note that even for an equatorially-concentrated α-effect (Panels B and C), a strong polar branch is nonetheless apparent in the butterfly diagrams, a direct consequence of the stronger radial shear present at high latitudes in the tachocline. Models using an α-effect operating throughout the whole convective envelope, on the other hand, would feed primarily on the latitudinal shear therein, so that for positive C_α the dynamo mode would propagate radially *upward* in the envelope (see Lerche and Parker, 1972).

It is noteworthy that co-existing dynamo branches, as in Panel B of Fig. 2.6, can have distinct dynamo periods (on this see also Belvedere et al., 2000), which in nonlinearly saturated solutions leads to long-term amplitude modulation. This does not occur for the $C_\alpha < 0$ solution, where both branches propagate away from each other, but share a common latitude of origin and so are phased-locked at the onset (cf. Panel C of Fig. 2.6).

An important take-home message from Fig. 2.6 is that the solar internal differential rotation profile, with its multiple shear regions, can lead to very complex dynamo wave patterns. Low latitude confinement and equatorward propagation, as suggested by the sunspot butterfly diagram, requires the α-effect to be concentrated at low latitudes at the base of the convection zone, and to be negative in the Northern hemisphere.

2.4 Flux transport dynamos

Meridional circulation can bodily transport the dynamo-generated magnetic field (terms labeled "transport" in Equations (2.3, 2.4)), and therefore, for a (presumably) solar-like equatorward return flow that is vigorous enough – in the sense of Rm being large enough – overpower the Parker–Yoshimura propagation rule (see, e.g. Choudhuri et al., 1995; Küker et al., 2001; Charbonneau and Barlet, 2011; Pipin and Kosovichev, 2011b). Figure 2.7 shows an example, here for a kinematic α-quenched $\alpha\Omega$ mean-field model including meridional flow, but otherwise identical to the model of Fig. 2.6A, i.e. an α-effect positive in the Northern hemisphere and $\propto \cos\theta$. In the absence of meridional flow this model would generate a dynamo wave propagating poleward at low latitude; but here the advective action of the meridional flow succeeds in driving equatorward propagation.

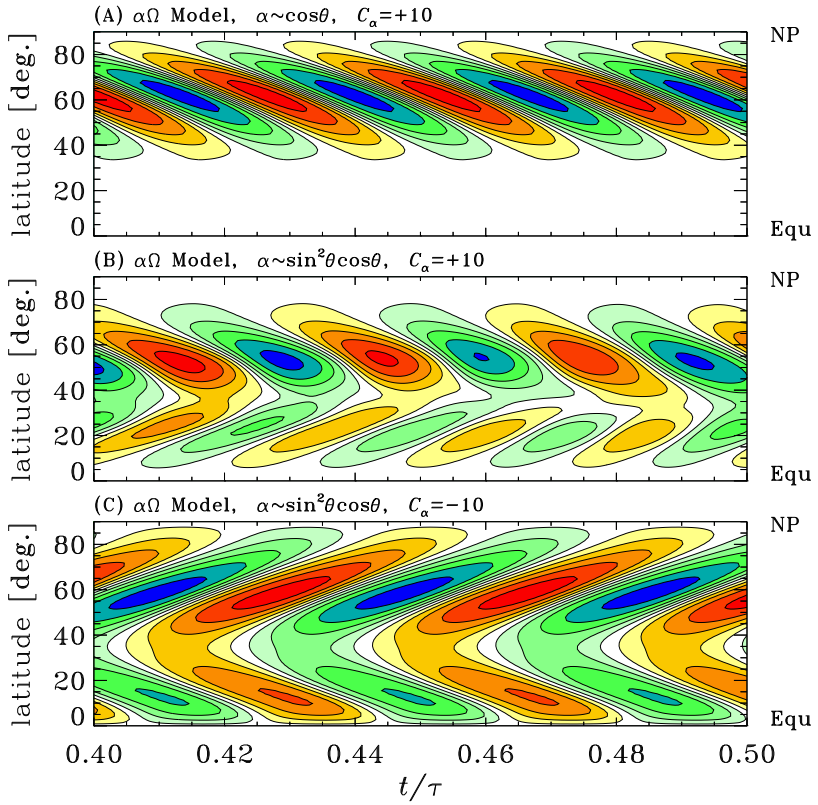

Figure 2.6: Northern hemisphere time-latitude ("butterfly") diagrams for the three α-quenched kinematic $\alpha\Omega$ dynamo solutions with different spatial distribution and sign for the α-effect. The diagrams are constructed at the depth $r/R_\odot = 0.7$ corresponding to the core-envelope interface. Isocontours of toroidal field are normalized to their peak amplitudes, and plotted for increments $\Delta B/_{\max}(B) = 0.2$, with yellow-to-red (green-to-blue) contours corresponding to $B > 0$ (< 0). The assumed latitudinal dependency of the α-effect is given above each panel. Other model ingredients as in Fig. 2.2. Note the co-existence of two distinct cycle periods in the solution shown in Panel B.

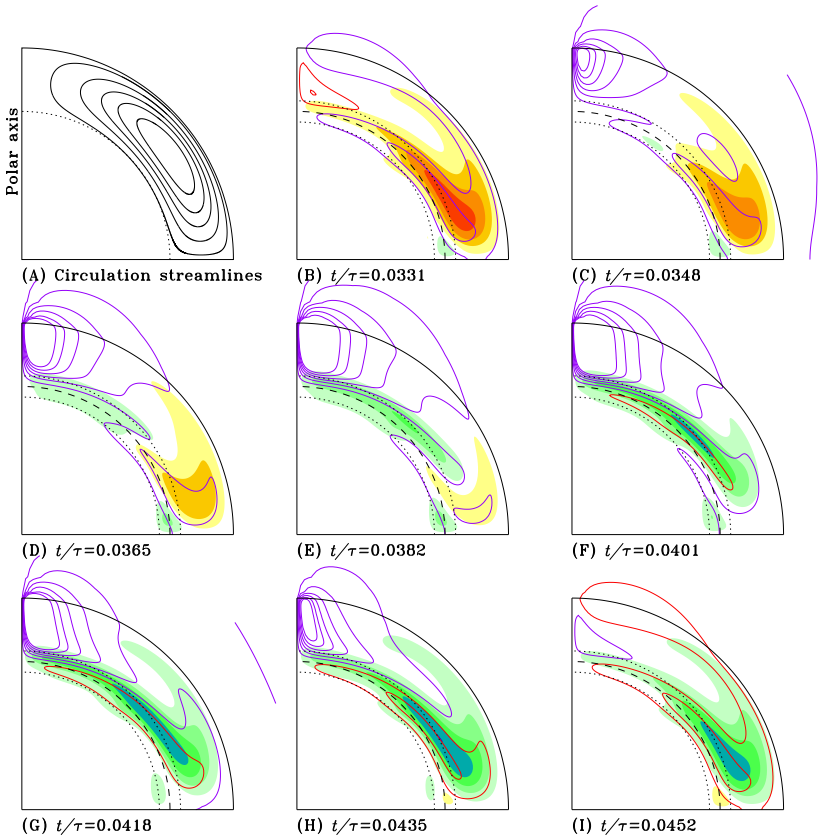

Figure 2.7: Snapshots covering half a cycle of an $\alpha\Omega$ kinematic mean-field linear $\alpha\Omega$ dynamo solution, including a meridional flow and α-quenching, spanning half a magnetic cycle. The defining parameters are $C_\Omega = 5 \times 10^5$, $C_\alpha = +0.5$, and Rm = 2500. Color coding of poloidal and toroidal components same as on Fig. 2.4 above. Note the strong amplification of the surface polar field and the latitudinal stretching of poloidal magnetic fieldlines at the core-envelope interface. An animation of this solution is available on the web page complementing these lecture notes.

The behavioral turnover from dynamo wave-like solutions to circulation-dominated magnetic field transport sets in when the circulation speed becomes comparable to the phase speed of the dynamo wave, i.e., in the high Rm regime. In this circulation-dominated regime, the cycle period loses sensitivity to the assumed turbulent diffusivity value, and becomes determined primarily by the circulation's turnover time. Models achieving equatorward propagation of the deep toroidal magnetic component in this manner are now often called *flux-transport dynamos* (see Dikpati and Gilman, 2009; Karak et al., 2014, and references therein).

Flux transport dynamo

In the opposite limit of low Rm, the dynamo wave is simply Doppler shifted, the frequency increasing (decreasing) if the wave travels in the same (opposite) direction as the flow (Roberts and Stix, 1972). If both flow and wave phase speeds are of the same order, then dynamo action can become severely altered, the solution sometimes transiting to a steady mode, or even decaying altogether, the exact behavior being dependent on model details. See §4.4 in Charbonneau (2020) for further discussion.

2.5 Babcock-Leighton models

Solar cycle models based on what is now called the Babcock–Leighton mechanism (see §1.8) were first proposed by Babcock (1961) and further elaborated by Leighton (1964, 1969), yet they were all but eclipsed by the rise of mean-field electrodynamics in the mid- to late 1960s. Their revival in the aerly 1990's was motivated in part by the fact that synoptic magnetographic monitoring over sunspot cycles 21 and 22 gave strong evidence that the surface polar field reversals are indeed triggered by the decay of active regions (see Wang et al., 1989; Wang and Sheeley Jr, 1991; Mackay and Yeates, 2012, and references therein).

2.5.1 Source term

The mean-field dynamo equations (2.11)–(2.12) are often taken as a starting point for building a solar cycle model based on the Babcock-Leighton mechanism. The idea is to replace the α-effect term in the poloidal equation (2.11) by a source term designed to capture the $T \to P$ workings of the Babcock-Leighton mechanism. Three main approaches are used in the literature:

1. A poloidal source term is introduced in the surface layers, and made linearly proportional to the toroidal field strength at the corresponding latitude at the bottom of the model convection zone This non-local approach was introduced by Wang et al. (1991) and later used by Dikpati and Charbonneau (1999), Charbonneau et al. (2005), Guerrero and de Gouveia Dal Pino (2008) Hotta and Yokoyama (2010); Kitchatinov and Olemskoy (2012), and Olemskoy and Kitchatinov (2013).

2. The $\alpha\Omega$ form of the mean-field dynamo equation is retained, with an α-effect-like poloidal source term concentrated in the surface layer, and

a "buoyancy algorithm" displaces toroidal fields from the bottom layers when some set field strength threshold is exceeded (Nandy and Choudhuri, 2001, 2002). See also Chatterjee et al. (2004) and Jiang et al. (2007).

3. Whenever the deep-seated toroidal field exceeds some preset threshold, an axisymmetric "double ring" of vector potential is deposited in the surface layer, and left to spread latitudinally under the influence of magnetic diffusion. This approach, developed by Durney (1995) (see also Durney 1996, 1997) and later used by Muñoz-Jaramillo et al. (2010), is closest to the essence of the Babcock–Leighton mechanism.

In all cases the poloidal source term is concentrated in the outer convective envelope, and is akin to a positive α-effect, in that a positive dipole moment is being produced from a positive deep-seated mean toroidal field. Most aforecited model implementations introduce an algebraic α-quenching-like upper operating threshold on the toroidal field strength. Some implementations also include a lower operating threshold, as suggested by thin flux tubes simulations (see, e.g., Durney, 1995; Nandy and Choudhuri, 2001; Charbonneau et al., 2005).

2.5.2 A representative solution

Figure 2.8 displays a sequence of meridional plane snapshots for a representative Babcock–Leighton dynamo solution computed following the model implementation of Charbonneau et al. (2005) (non-local source term, radial profile given by the red curve on Fig. 2.2). The equatorward advection of the deep toroidal field by meridional circulation is here clearly apparent. Note also how the surface poloidal field first builds up at low latitudes, and is subsequently advected poleward and concentrated near the pole. Compare this carefully to the similar Figure 2.7, for a flux transport mean-field $\alpha\Omega$ solution. Both behave very similarly, yet in principle embody very different inductive mechanisms for the poloidal field.

2.5.3 Cycle period and butterfly diagram

Figure 2.9 shows N-hemisphere time-latitude diagrams for the toroidal magnetic field at the core-envelope interface (Panel A), and the surface radial field (Panel B), for a Babcock–Leighton dynamo solution taken from Dikpati and Charbonneau (1999). Note how the polar radial field changes from negative (blue) to positive (red) at just about the time of peak positive toroidal field at the core-envelope interface; this is the phase relationship inferred from synoptic magnetograms (see, e.g., Figure 2.1 herein) as well as observations of polar faculae (see Sheeley Jr, 1991).

Although it exhibits the desired equatorward propagation, the toroidal field butterfly diagram in Panel A of Figure 2.9 peaks at much higher latitude ($\sim 45^\circ$) than the sunspot butterfly diagram ($\sim 15^\circ - 20^\circ$, cf. Figure 2.1). This occurs because this is a solution with high magnetic diffusivity contrast, where meridional

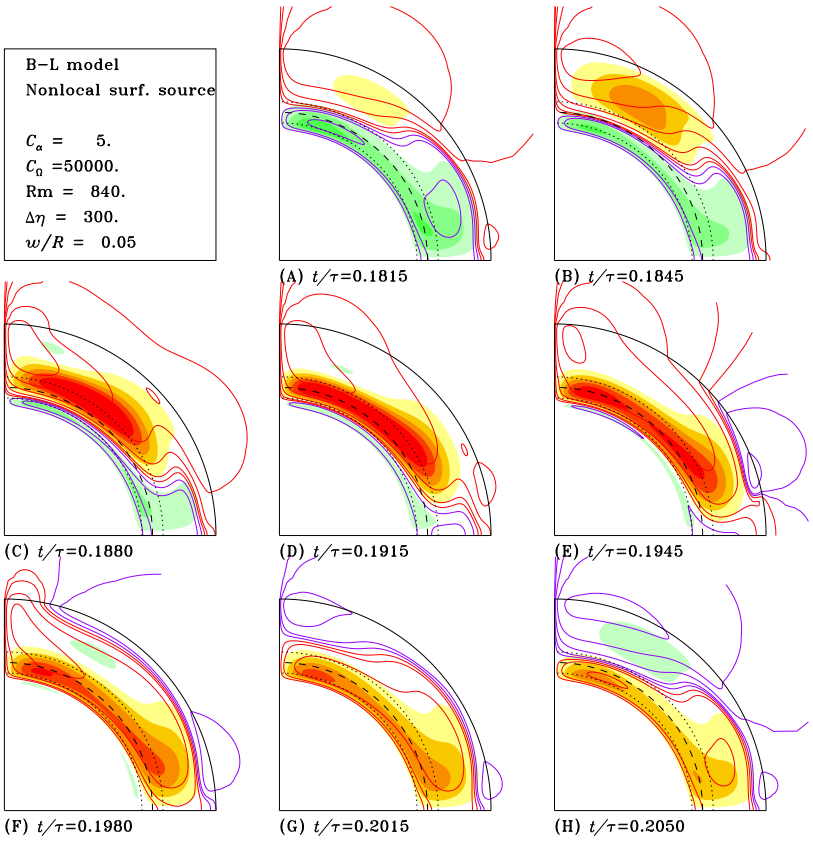

Figure 2.8: Snapshots covering half a cycle of a kinematic mean-field-like Babcock-Leighton dynamo solution, spanning half a magnetic cycle. The defining parameters are $C_\Omega = 5 \times 10^4$, $C_\alpha = +5$, and Rm = 840. Format same as on Fig. 2.7 above. Note again the strong amplification of the surface polar field, leading here to a buildup of toroidal field in the high-latitude portion of the tachocline. An animation of this solution is available on the web page complementing these lecture notes.

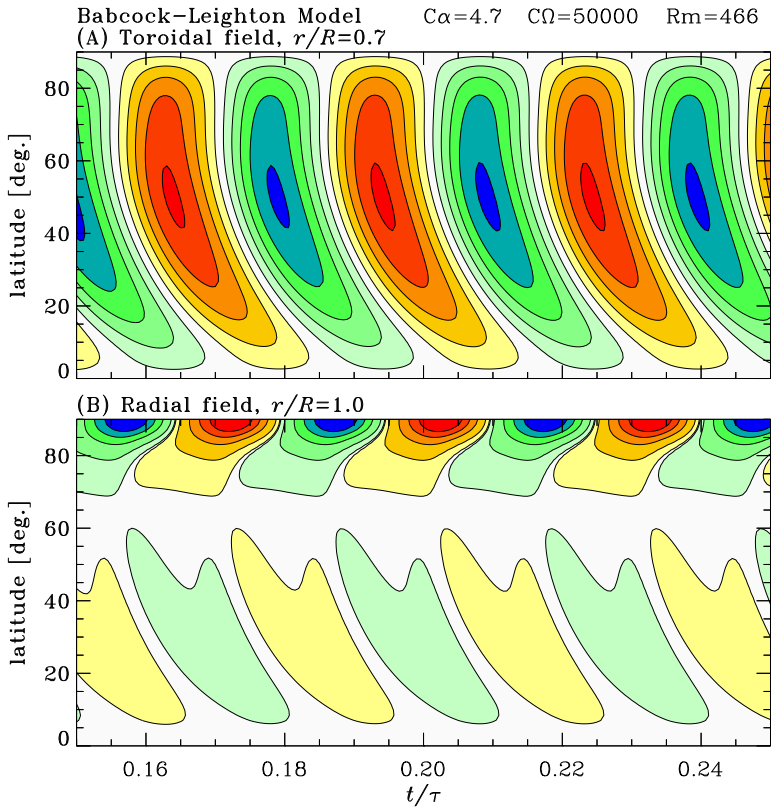

Figure 2.9: Time-latitude diagrams of the toroidal field at the core-envelope interface (Panel A), and radial component of the surface magnetic field (Panel B) in the Babcock–Leighton model of the solar cycle. This solution is computed for solar-like differential rotation and meridional circulation, the latter here closing at the core-envelope interface. The core-to-envelope contrast in magnetic diffusivity is $\Delta\eta = 1/300$, the envelope diffusivity $\eta_T = 2.5 \times 10^{11}$ cm^2 s^{-1}, and the (poleward) mid-latitude surface meridional flow speed is $u_0 = 16$ m s^{-1}. Figure produced from numerical data kindly provided by M. Dikpati.

circulation closes at the core-envelope interface, so that the *latitudinal* component of differential rotation dominates the production of the toroidal field. This difficulty can be alleviated by adjustment of the meridional flow profile (see, e.g. Nandy and Choudhuri, 2001, 2002), or (of course) by artificially concentrating the Babcock-Leighton poloidal source term at low latitudes.

A noteworthy property of this class of solar cycle model is the dependency of the cycle period on model parameters; in the advection dominated regime, the meridional flow speed is found to be the primary determinant of the cycle period P. For example, in the Dikpati and Charbonneau (1999) model, the cycle period P scales as:

$$P = 56.8\, u_0^{-0.89} s_0^{-0.13} \eta_T^{0.22} \text{ [yr]}. \tag{2.22}$$

This behavior arises because, in these models, the two source regions are spatially segregated, and the time required for circulation to carry the poloidal field generated at the surface down to the tachocline is what effectively sets the cycle period. The corresponding time delay introduced in the dynamo process has rich dynamical consequences (see, e.g., Charbonneau et al., 2005, and references therein). The weak dependency of P on η_T and on the magnitude s_0 of the poloidal source term is very much unlike the behavior typically found in mean-field models, where both these parameters usually play a dominant role in setting the cycle period.

Magnetic flux transport in Babcock-Leighton model can also be achieved by means other than the meridional flow, notably by turbulent pumping (§1.6.1) With the expected downward pumping throughout the bulk of the convective envelope, and with a significant equatorward latitudinal component at low latitudes (see Fig. 2.13D,E further below), the Babcock–Leighton mechanism can lead to dynamo action even if the internal meridional flow is weak and/or constrained to the upper portion of the convective envelope. Downward turbulent pumping then links the two sources regions, and latitudinal pumping provides the needed equatorward concentration of the deep-seated toroidal component. See Guerrero and de Gouveia Dal Pino (2008); Karak and Nandy (2012); Jiang et al. (2013); Karak et al. (2014); Hazra and Nandy (2016); Karak and Cameron (2016). The dynamo solutions presented Guerrero and de Gouveia Dal Pino (2008) are found to obey a scaling law of the form

$$P = 181.2\, u_0^{-0.12} \gamma_{r0}^{-0.51} \gamma_{\theta 0}^{-0.05} \text{ [yr]}, \tag{2.23}$$

over a wide range of parameter values. The radial pumping speed γ_{r0} emerges here as the primary determinant of the cycle period.

2.5.4 Beyond 2D: non-axisymmetric models

Some recent Babcock-Leighton solar cycle models abandon the axisymmetric approximation, either by solving the problem in three spatial dimensions (Yeates and Muñoz-Jaramillo, 2013; Miesch and Dikpati, 2014; Miesch and Teweldebirhan, 2016; Hazra et al., 2017; Karak and Miesch, 2017; Kumar et al., 2019;

Whitbread et al., 2019), or solving a (non-axisymmetric) surface magnetic flux evolution model concurrently with a axisymmetric mean-field-like interior dynamo model (Lemerle and Charbonneau, 2017; Nagy et al., 2017). All of these dynamo models are still kinematic (prescribed, time independent differential rotation and meridional flow), and use a mean-field-like turbulent diffusivity. A parameterized prescription is introduced to generate emergence of (tilted) bipolar magnetic regions in the surface layers of the model, as a function of the internal distribution of magnetic fields.

See §5.5 in Charbonneau (2020) for more on such non-axisymmetric model formulations.

2.6 Cycle regulation and fluctuations

The nonlinear dynamical backreaction of the field on the flow is a *sine qua non* energetic requirement for field amplification (viz. rightmost term in Eq. (1.23)). It can achieve saturation of the magnetic field, as with the simplistic algebraic α-quenching introduced in §2.3.3, or generate periodic or quasi-periodic variability of the basic cycle on a variety of timescales, depending on the inductive mechanisms included in a given dynamo model. Moreover, the turbulent nature of the solar convection zone implies that most of the inductive mechanisms considered in the first lectures will be subjected to significant stochastic fluctuations. *The solar dynamo is both nonlinear and stochastic.*

This section aims at providing a brief introduction to these matters, and indicating a few good entry points into the vast technical literature on this topic. See also §7 in Charbonneau (2020).

2.6.1 Stochastic forcing

Sources of stochastic fluctuations abound in the solar interior, all ultimately due to the strongly turbulent character of solar convection, the ultimate energy source of all inductive processes contributing to solar dynamo action. Tensor components describing the turbulent electromotive force are expected to be strongly fluctuating quantities, an expectation confirmed by analytical estimates (e.g., Hoyng, 1988, 1993) and measurements in numerical simulations (e.g., Otmianowska-Mazur et al., 1997; Ossendrijver et al., 2001; Brandenburg and Sokoloff, 2002; Käpylä et al., 2006; Racine et al., 2011; Simard et al., 2016; Warnecke et al., 2018, and references therein).

The effect of stochastic forcing has been investigated in most detail in the context of classical mean-field models (see Choudhuri, 1992; Hoyng, 1993; Ossendrijver and Hoyng, 1996; Ossendrijver et al., 1996; Mininni and Gómez, 2002, 2004; Moss et al., 2008; Charbonneau and Barlet, 2011). In models not too far from criticality variations of the cycle amplitude on timescales much longer than the cycle period are readily generated, especially when the models include a tachocline-like low-diffusivity layer beneath the nominal convection zone.

As for the Babcock-Leighton mechanism, observations of emerging bipolar magnetic active regions reveals large fluctuations in key characteristics for buildup of surface polar fields, notably tilt angle, flux, and pole separation Mean-field-like implementations of Babcock-Leighton dynamos behave similarly to bona fide mean-field models upon introduction of random stochastic forcing in their source term and/or other model components (see e.g. Charbonneau and Dikpati, 2000; Charbonneau and Barlet, 2011; Choudhuri and Karak, 2012; Olemskoy and Kitchatinov, 2013; Kitchatinov et al., 2018; Hazra and Nandy, 2019). In particular, incorporating observed distributions of active region properties in Babcock-Leighton dynamos including a latitude-longitude representation of the solar surface, as considered in §2.5.4, can also lead to very solar-like cyclic behavior. See, e.g., Nagy et al. (2017) and Karak and Miesch (2017).

2.6.2 A zoo of nonlinearities

The nonlinear dynamical feedback of the field on the flow can achieve saturation of the magnetic field in various ways, depending on the inductive mechanisms included in a given dynamo model:

- The magnetic field can suppress the turbulent cyclonic fluid motions giving rise to the α-effect. This is generally known as α-quenching, and is potentialy important in all mean-field dynamo models relying on a turbulent electromotive force. For α-quenching formulations more elaborate than introduced in §2.3.3, see e.g. Brandenburg et al. (2009); Pipin et al. (2012). α-quenching

- The Lorentz force associated with the large-scale magnetic field can suppress the large-scale flows contributing to induction. This is traditionally called the Malkus-Proctor effect, and is a potentially important nonlinearity in all models relying on shearing by differential rotation to generate the toroidal large-scale magnetic component. See, e.g., Moss and Brooke (2000); Bushby (2006); Simard and Charbonneau (2020). Malkus-Proctor effect

- The magnetic field can reduce differential rotation indirectly by altering the Reynolds stresses powering large-scale flows. This is known as Λ-quenching, and like the Malkus-Proctor effect is a potentially important nonlinearity in any model where the toroidal field is produced through shearing by differential rotation. See, e.g., Kitchatinov and Rüdiger (1993); Küker et al. (1999). Λ-quenching

- Magnetic flux loss through magnetic buoyancy is potentially important in all dynamo models: $\sim 10^{17}$ Wb of magnetic flux emerges in the form of active region in the course of a typical cycle. See, e.g., Moss et al. (1990); Kitchatinov et al. (2000)

- In flux transport models relying on the Babcock-Leighton mechanism for regenerating the surface dipole, the growing magnetic field can cause a

tilt-quenching

reduction of the tilt giving rise to a dipole component in emerging bipolar magnetic regions. See, e.g., Lemerle and Charbonneau (2017); Jha et al. (2020).

- In flux transport dynamo models operating with spatially segregated source regions, including but not limited to Babcock-Leighton models, the growing magnetic field can reduce the efficiency of the transport mechanism linking the two source regions. See, e.g., Rempel (2006); Karak and Choudhuri (2012).

2.6.3 The dynamo as a dynamical instability

The behavior seen on Fig. 2.5 is typical of self-excited dynamos operating near criticality, whatever the actual nonlinear mechanism of amplitude saturation may be. However weak the magnetic field of the initial condition (excluding only $\mathbf{B} = 0$ everywhere in the domain), supercritical solutions ($D/D_{\rm crit} > 1$) grow exponentially and saturate at a magnetic amplitude increasing with the value of the dynamo number; whereas in subcritical solutions ($D/D_{\rm crit} < 1$) the magnetic field always decays exponentially to zero, no matter how strongly magnetized an initial condition might be. Dynamo action can thus be viewed as an *instability*. Zero magnetic field is always a valid solution to the induction equation, but beyond $D_{\rm crit}$ this solution becomes unstable to any small magnetic perturbation introduced in the system.

In the language of dynamical systems, the onset of dynamo action reflects the loss of stability of the fixed-point trivial solution $\mathbf{B} = 0$ to a limit cycle, through a *Hopf bifurcation*. This is illustrated schematically on Figure 2.10A, showing a *bifurcation diagram* as could be constructed from a sequence of solutions with increasing $D/D_{\rm crit}$, as on Fig. 2.5. The thick line represents a measure of the saturated magnetic amplitude, plotted versus the dynamo number normalized to its critical value. Immediately beyond the bifurcation point, the saturated amplitude increases first very rapidly, then gradually more slowly, with increasing $D/D_{\rm crit}$. The Hopf bifurcation route to cyclic dynamo action is believed to be a generic feature of nonlinear solar/stellar dynamos (e.g. Tobias et al., 1995; Weiss and Tobias, 2016, and references therein).

Hopf bifurcation

Bifurcation diagram

Some of the magnetic field regeneration mechanism described in the first lecture are subject to a lower operating threshold on the magnetic field strength. This is the case for the Babcock-Leighton mechanism (§1.8), as well as for the mean electromotive force generated by the development of MHD instabilities in the tachocline (§1.7). The presence of an operating threshold on $\mathbf{B}$ leads to the bifurcation structure depicted schematically on Fig. 2.10B. Even if $D/D_{\rm crit} > 1$, the initial condition must lie within the *attraction basin* (gray shaded area) for exponential growth to the stable limit cycle solution to ensue. Initial conditions lying outside the attraction basin decay exponentially to the trivial solution $\mathbf{B} = 0$. Unlike for the classical Hopf bifurcation of panel A, now at the onset of dynamo action the magnetic amplitude is already finite. Such dynamos are not self-excited, in that they cannot amplify an arbitrarily weak seed magnetic

Attraction basin

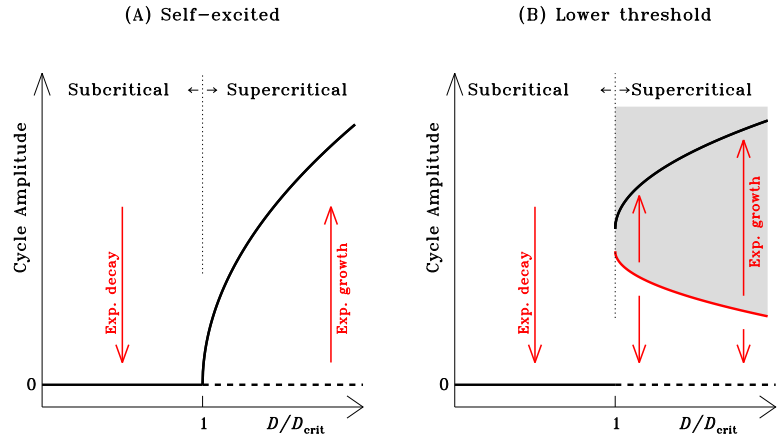

Figure 2.10: Schematic depiction of a bifurcation leading to nonlinearly saturated cycle amplitude following onset of dynamo action beyond the critical dynamo number. Panel (A) is a standard Hopf bifurcation, relevant to self-excited dynamos such as those relying on the mean-field α-effect. The thick black line shows the variation of the nonlinearly saturated cycle amplitude as a function of the dynamo number D, normalized to its critical value $D_{\rm crit}$. Panel (B) shows the bifurcation structure expected in dynamo with a lower operating threshold on the magnetic field strength. In that latter case dynamo solutions materialized only in a finite-sized basin of attraction, indicated by the gray shading (see text).

field.

2.6.4 Intermittency

The distinction between the two bifurcation structures depicted on Fig. 2.10 has important consequences for the response of the dynamo to stochastic forcing, and in particular for the production of so-called Grand Minima of markedly suppressed cyclic activity (viz. Lectures by Theodosius Chatzistergos). As depicted schematically on Fig. 2.11A, fluctuations (of whatever origin) of inductive process can push the solution across the primary Hopf bifurcation, leading to shutdown of dynamo action. In non-self-excited dynamos, fluctuations can knock the solution out of its basin of attraction, leading to a collapse to the trivial solution $\mathbf{B} = 0$ (Fig. 2.11B). An an additional inductive mechanism is then required to climb back into the attraction basin.

See §7.3 in Charbonneau (2020) for a few examples of dynamo models exhibiting intermittency, and further references to the technical literature.

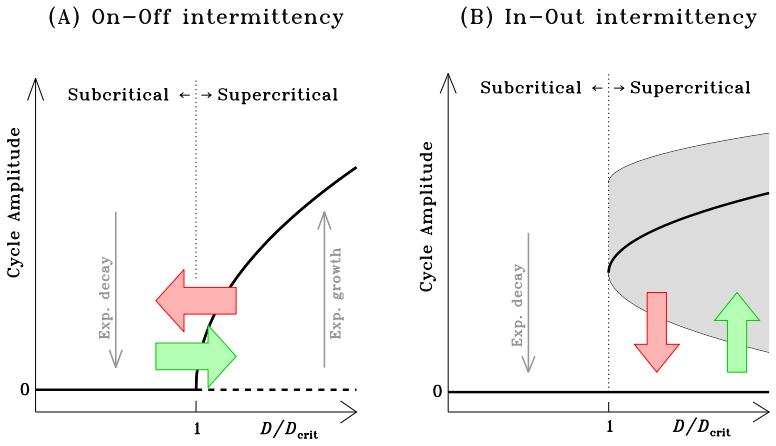

Figure 2.11: Schematic depiction of (A) on-off intermittency and (B) in-out intermittency in a generic bifurcation diagram close to criticality. In (B) the gray shaded area indicates the basin of attraction of the finite amplitude cycle. Outside of this basin the amplitude decays exponentially to zero, even if $D > D_{\rm crit}$ (see text).

2.7 Insight from MHD numerical simulations

I close with a brief overview of some results from MHD numerical simulations that offer some level support for the various geometrically and physically simpler solar cycle models described in the course of this lecture.

2.7.1 Large-scale magnetic fields and cycles

Magnetohydrodynamical (MHD) simulations of solar convection solve numerically the set of coupled nonlinear partial differential equations describing the conservation of mass, momentum, internal energy and magnetic flux in a thick spherical shell of electrically conducting fluid subjected to thermal forcing. The dynamical backreaction of the Lorentz force on the inductive flow is then properly captured at all scales resolved by the simulation.

Starting with pioneering work of Gilman (1983) and Glatzmaier (1984, 1985), and propelled by ever improving compute power and algorithmic design, in the past decade many global MHD simulations have succeeded in generating a large-scale magnetic field, sometimes undergoing polarity reversals in the form of more or less regular cycles; for a representative sample, see: Racine et al. (2011); Masada et al. (2013); Nelson et al. (2013); Fan and Fang (2014); Simitev et al. (2015); Duarte et al. (2016); Guerrero et al. (2016); Hotta et al. (2016); Käpylä et al. (2017); Strugarek et al. (2018).

As an example of a simulated large-scale magnetic cycle, consider Figure 2.12, showing sample results for a 300-yr long segment of the EULAG-MHD

1600-yr long "millenium" simulation discussed in Passos and Charbonneau (2014). This simulation generates a very regular magnetic cycle, well synchronized

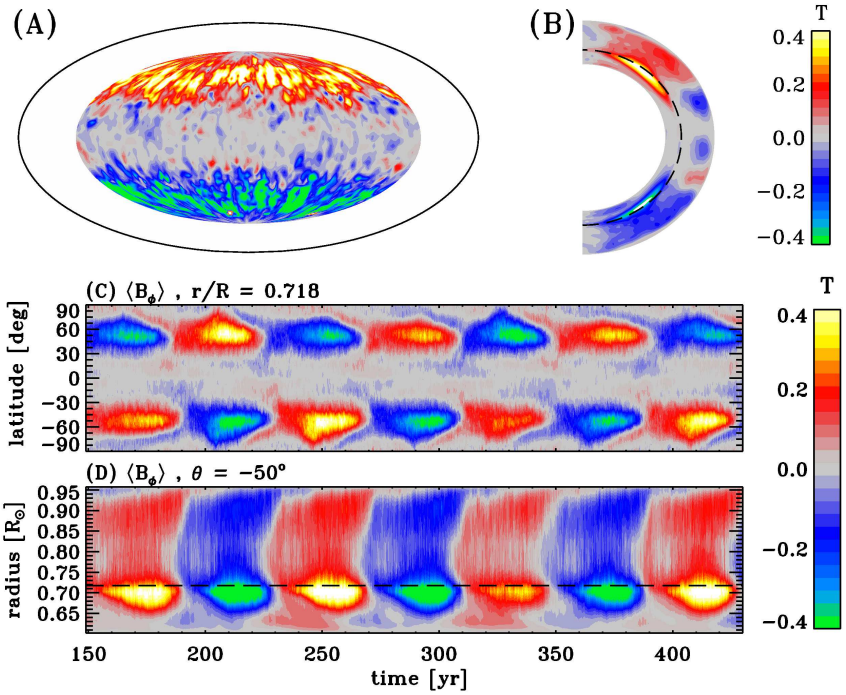

Figure 2.12: Magnetic cycles in the global EULAG-MHD anelastic "millenium" simulation of Passos and Charbonneau (2014). Part (A) shows a snapshot in Mollweide projection of the toroidal (zonal) magnetic component at depth $r/R_\odot = 0.718$; part (B) is a snapshot of the zonally-averaged toroidal field in a meridional plane, taken at the same time as in (A). Part (C) and (D) show respectively time-latitude and radius-latitude diagrams of the zonally-averaged toroidal field, the former at depth $r/R = 0.718$ and the latter at latitude -50 degrees. The dashed lines in (B) and (D) indicate the bottom of the convectively unstable layers. An animation of this simulation is available on the web page complementing these Lectures notes.

across hemispheres and with the magnetic field antisymmetric about the equator, all similar to the sun, but with a full magnetic cycle period of about 80 yr, longer than the sun's by a factor of nearly four, at the upper end of the range of cycle periods produced by other global MHD simulations that produce reasonably regular magnetic cycles. As evidenced on Fig. 2.12B and D, the magnetic field accumulates and reaches its peak strength in the outer reaches of the convectively stable fluid layer (see also Browning et al., 2006; Masada et al., 2013; Guerrero et al., 2016, 2019), approaching or exceeding equipartition. The "butterfly diagram" of panel C indicates that activity peaks at mid- rather than

low-latitudes, and shows only a hint of equatorward propagation on the poleward edges of the toroidal field bands; some other simulations fare better in this respect (e.g. Warnecke et al., 2014; Augustson et al., 2015; Duarte et al., 2016; Strugarek et al., 2018). This simulation also generates a strong dipole moment oscillating in phase with the toroidal component, torsional oscillations of solar-like magnitude, and a weak cyclic modulation of the convective luminosity in phase with the magnetic cycle, also solar-like.

Summing up the most salient empirically determined features of simulated large-scale magnetic cycles materializing in these types of MHD simulations:

- Regular, solar-like stable cycles with strong hemispheric coupling and synchrony are the exception rather than the rule.
- The presence and period of magnetic cycles depends sensitively on rotation; low Ro favors magnetic cycles, high Ro favors steady large-scale magnetic fields. In the solar range of Ro, the cycle period increases with increasing rotation rate.
- Multiple magnetic cycles with significantly different periods can coexist at moderately small Rossby numbers ($0.1 \lesssim \mathrm{Ro} \lesssim 1$).
- In many (but not all, viz. Viviani et al. 2019) simulations, the spatiotemporal propagation of the large-scale magnetic fields appears consistent with the Parker-Yoshimura rule for dynamo waves.
- Both Λ-quenching and the Malkus-Proctor mechanism are detected in simulations. A form α-quenching is also measured, while quenching of the turbulent diffusivity appears marginal.
- The presence of a stably stratified fluid layer underlying the convecting fluid yields longer period cycles, and the growth of MHD instabilities therein may impact cyclic activity

For further details and discussion of these types of global MHD simulations, see §3 in Charbonneau (2014) and/or §6 in Charbonneau (2020).

2.7.2 Mean-field tensors

The output of the global simulations ijust discussed can be used to *measure* the mean-field coefficient introduced previously, including the essential α-tensor, and thus test the range of validity and analytic predictions of mean-field theory (see Brandenburg and Sokoloff, 2002; Schrinner et al., 2007; Racine et al., 2011; Dubé and Charbonneau, 2013; Augustson et al., 2015; Beaudoin et al., 2016; Simard et al., 2016; Warnecke et al., 2018; Viviani et al., 2019).

As an example, Figure 2.13A–C shows meridional plane representations of the diagonal elements of the $\boldsymbol{\alpha}$-tensor, radial and latitudinal turbulent pumping speed in D–E, and in F the isotropic part of the the turbulent diffusivity tensor $\boldsymbol{\beta}$, all extracted from the same global MHD simulation as on Fig. 2.12 (Simard

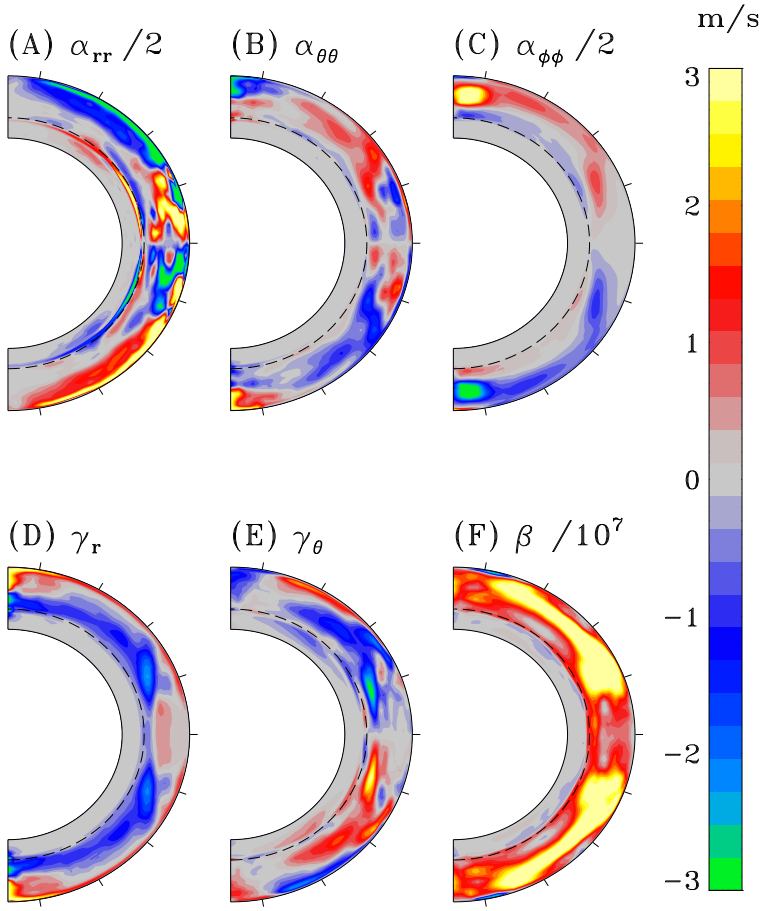

Figure 2.13: A selection of mean-field tensor components extracted from a global EULAG-MHD simulations of magnetic cycles (to be discussed in chapter 2, viz. Fig. 2.12). (A) α_{rr}; (B) $\alpha_{\theta\theta}$; (C) $\alpha_{\phi\phi}$; (D) radial turbulent pumping speed γ_r; (E) latitudinal turbulent pumping speed γ_θ; (F) the isotopic part of the $\boldsymbol{\beta}$ tensor, in unit of $10^7\,\mathrm{m^2 s^{-1}}$. In all cases the extraction is carried out independently in each hemisphere, so that the high degree of symmetry/antisymmetry about the equatorial plane is a true feature of the simulation.

et al., 2016). These show both similarities and differences with the tensor components extracted from the distinct simulations of Augustson et al. (2015) and Warnecke et al. (2018). Focusing on the similarities, the following appear to be robust properties:

α-effect

- The $\boldsymbol{\alpha}$-tensor is full, with off-diagonal components of roughy similar magnitude as diagonal components;
- The largest magnitudes, reaching up to a few tens of $\mathrm{m\,s^{-1}}$, are found in the α_{rr} component, with $\alpha_{\phi\phi}$ taking second place. The simulations of Augustson et al. (2015) is somewhat more balanced in this respect, with the $\alpha_{\theta\theta}$ and off-diagonal components showing magnitudes similar to α_{rr} and $\alpha_{\phi\phi}$.
- $\alpha_{\phi\phi}$ and $\alpha_{\theta\theta}$ are both mostly positive (negative) in the Northern (Southern) hemisphere, but shows a sign change near the base of convecting fluid layer;

Turbulent pumping

- Radial turbulent pumping is downwards in the bulk of the convecting layers.
- Significant equatorward latitudinal turbulent pumping, at speed ranging from a few to $\sim 10\,\mathrm{m\,s^{-1}}$, materializes at mid- to low-latitudes in the bulk of the convecting fluid layers.

Turbulent diffusivity

- The isotropic turbulent diffusivity β is high, ranging from a few $10^7\,\mathrm{m^2\,s^{-1}}$ on Fig. 2.13F, approaching $10^9\,\mathrm{m^2\,s^{-1}}$ in the more luminous simulations analyzed by Warnecke et al. (2018).
- In mean-field terminology, simulated large-scale magnetic cycles are driven by an $\alpha^2\Omega$ dynamo.

2.7.3 Flux emergence from numerical simulations

Some of the aforecited global MHD simulations of solar convection have also been found to generate elongated tube-like strands of superequipartition magnetic field (Nelson et al., 2013, 2014; Fan and Fang, 2014; Chen et al., 2017). Figure 2.14 shows an example, taken from Nelson et al. (2013). At low latitudes within its convective layers, this global MHD simulations generates an intense toroidal flux system of opposite polarity the two hemisphere (left panel). Within each of these so-called wreaths, superequipartition-strength magnetic flux strands form and are entrained by turbulent convection, forming Ω-loop-like undulations that grow and rise under the combined action of convective entrainement and buoyancy caused a density deficit within the strands (center and right panels).

Ω-loops

Despite being locally twisted and deformed by convective fluid motions, the rising flux strands manage to maintain the overall East-West alignment of the

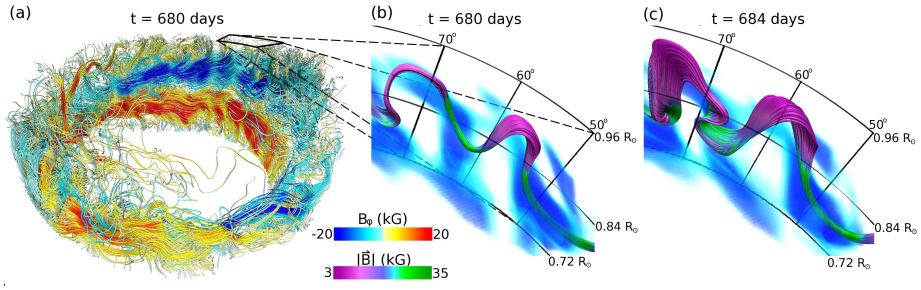

Figure 2.14: Formation and rise of rope-like magnetic flux systems in the wreaths of toroidal magnetic field generated in the 3D global MHD simulations of Nelson et al. (2013). The superequipartition-strength magnetic flux strands form within the wreaths and subsequently expand and twist as they rise towards the top of the simulation domain. Reproduced from Nelson et al. (2013) (their Figure 18), by permission

toroidal wreaths from which they originate, and thus would satisfy Hale's polarity law. Moreover, the strand's apexes develop a Joy Law-like tilt as they rise to the top of the simulation domain (Nelson et al., 2014). This is caused by twisting by the cyclonicity of the turbulent convective upflows, as in the thin flux tube simulations of Weber et al. (2013).

For further details and discussion of the formation and emergence of magnetic flux ropes in in global MHD simulations, Fan (2021).

2.8 Summary

- There is currently no concensus on a "basic" solar cycle model; various inductive mechanisms are possible, and may be operating concurrently;
- There is currently no concensus on the exact channel(s) through which the dynamical backreaction of the Lorentz force regulates the solar cycle's amplitude and duration;
- The nonlinear dynamics of flow-field interactions can generate a wide variety of cycle amplitude patterns, going from simple amplitude stabilisation all the way to chaotic modulation;
- The turbulent nature of the solar convection zone, within which the dynamo is operating in part or entirely, implies that transport and inductive mechanisms acting therein are subjected to strong stochastic fluctuations;
- The solar dynamo is both nonlinear and stochastic;
- The interaction of stochastic forcing with dynamical nonlinearities can generate a bewildering spectrum of behaviors unfolding on timescales much longer than the period of the primary magnetic cycle.

Appendix A

Linear Cartesian dynamo waves

This Appendix presents the analytic solution of the mean-field dynamo equations first obtained by Parker (1955), demonstrating the existence of dynamo wave behavior.

Parker's solution is kinematic and formulated in Cartesian geometry, as with the simple exponentially growing/decaying solution considered in §1.6.3, but now introduces a large-scale, uniformly sheared flow in the problem. To be specific, working in Cartesian geometry we identify the direction $\hat{\mathbf{e}}_z$ as "radial", $\hat{\mathbf{e}}_y$ as "azimuthal", and $\hat{\mathbf{e}}_x$ as "latitudinal". We write the mean flow as:

$$\langle \mathbf{U} \rangle = \Omega z \hat{\mathbf{e}}_y \ , \tag{A.1}$$

describing a purely 'radial" constant shear, and express the large-scale magnetic field as:

$$\langle \mathbf{B} \rangle (x,z,t) = \nabla \times (A(x,z,t)\hat{\mathbf{e}}_y) + B(x,z,t)\hat{\mathbf{e}}_z \ . \tag{A.2}$$

Assuming again $\beta \gg \eta$, upon substituting this expression into the mean-field induction equation (1.52), the latter separates into:

$$\frac{\partial A}{\partial t} - \beta \left(\frac{\partial^2 A}{\partial x^2} + \frac{\partial^2 A}{\partial z^2} \right) = \alpha B \ , \tag{A.3}$$

$$\frac{\partial B}{\partial t} - \beta \left(\frac{\partial^2 B}{\partial x^2} + \frac{\partial^2 B}{\partial z^2} \right) = -\Omega \frac{\partial A}{\partial x} + \alpha \left(\frac{\partial^2 A}{\partial x^2} + \frac{\partial^2 A}{\partial z^2} \right) \ . \tag{A.4}$$

With α, β and Ω independent of position and time, eigensolutions can be sought in the form of plane waves:

$$\begin{bmatrix} A(x,z,t) \\ B(x,z,t) \end{bmatrix} = \begin{bmatrix} a \\ b \end{bmatrix} \exp\bigl[\lambda t + \mathrm{i}k(z\cos\vartheta + x\sin\vartheta)\bigr] \ . \tag{A.5}$$

where the wavenumber k sets the scale of the large-scale magnetic field, and ϑ the propagation direction in the $[x, z]$ plane. Substituting this expression into Eqs. (A.3)–(A.4) leads to the dispersion relation

$$\left(\lambda + \beta k^2\right)^2 = \alpha k\left(\alpha k + \mathrm{i}\,\Omega \sin\vartheta\right) . \tag{A.6}$$

This is a quadratic (complex) polynomial in λ, with the two solutions:

$$\begin{aligned}\lambda_\pm = \quad - \quad & \beta k^2 \pm \sqrt{\frac{|\alpha| k}{2}} \Bigg\{ \left(\sqrt{\Omega^2 \sin^2\vartheta + \alpha^2 k^2} + |\alpha| k\right)^{\frac{1}{2}} \\ + \quad & \mathrm{i}\,\mathrm{sign}(\Omega\alpha \sin\vartheta) \left(\sqrt{\Omega^2 \sin^2\vartheta + \alpha^2 k^2} - |\alpha| k\right)^{\frac{1}{2}} \Bigg\} ,\end{aligned} \tag{A.7}$$

The λ_- solution can only produce decaying disturbances ($\mathrm{Re}(\lambda_-) < 0$), whereas the λ_+ root can potentially leads to dynamo action, in the sense that $\mathrm{Re}(\lambda_+) > 0$. Examination of equation (A.7) indicates that an exponentially growing *dynamo wave* can materialize in a finite wavenumber "window" $k \in]0, k_*[$, where k_* is a root of:

$$k_*^6 - \frac{\alpha^2}{\beta^2} k_*^4 - \frac{\alpha^2 \Omega^2}{4\beta^4} \sin^2\vartheta = 0 . \tag{A.8}$$

In the limit of strong shear ($|\alpha| \ll \sqrt{\beta |\Omega \sin\vartheta|}$, or, equivalently, if the second term on the RHS of Eq. (A.4) is negligible with respect to the first, then we have

$$\mathrm{Re}(\lambda_+) \simeq -\beta k^2 + \sqrt{\frac{|\alpha\Omega \sin^2\vartheta| k}{2}} , \tag{A.9}$$

and exponential growth of the magnetic field will thus take place provided

$$\frac{|\alpha\Omega \sin\vartheta|}{2\beta^2 k^3} > 1 . \tag{A.10}$$

with the root of Eq. (A.8) then given by

$$k_* \simeq \left(\frac{|\alpha\Omega \sin\vartheta|}{2\beta^2}\right)^{1/3} . \tag{A.11}$$

Dynamo number

The LHS of Eq. (A.10) thus acts as the dynamo number for this dynamo wave solution, with a critical value of unity. Once again we find that the larger scales (small k) are favored by the dynamo process. Equation (A.10) indicates that the growth rates is largest for $\vartheta = \pi/2$; i.e., for a wavevector oriented in x, along isolines of $\langle \mathbf{U} \rangle$.

The eigenvalues associated with these growing solutions have nonzero imaginary parts, so that the combined action of large-scale shear (Ω), turbulent induction (α) and turbulent dissipation (β) can generate propagating *dynamo*

waves, leading to local reversals of magnetic polarity every half-wave period (Parker, 1955). In this shear-dominated regime the frequency of these so-called dynamo waves is given by

$$\mathrm{Im}(\lambda_+) \simeq \mathrm{sign}(\Omega\alpha\sin\vartheta)\,\sqrt{\frac{|\alpha\Omega\sin\vartheta|k}{2}}\ . \tag{A.12}$$

The sign of the product $\alpha\Omega$ thus sets the propagation direction along the $\langle\mathbf{U}\rangle$ isolines. This is known as the *Parker-Stix-Yoshimura* sign rule, and carries over to models in non-cartesian geometries with dynamo coefficients varying with position (see Stix, 1976; Yoshimura, 1975). Here if we associate z with the radial direction and $\langle\mathbf{U}\rangle$ with differential rotation ($y \equiv$longitude), this implies dynamo waves propagating in the latitudinal direction, consistent with the equatorward progression of activity belts evidenced by the sunspot butterfly diagram (see §2.1), provided the product $\alpha \times \Omega$ is negative.

In the opposite limit $\Omega \to 0$, the imaginary part of the eigenvalue vanishes (viz. Eq. (A.7)), Eq. (A.6) leads to a condition for exponential growth ($\lambda > 0$) identical to Eq. (1.60), as expected.

Bibliography

Augustson, K., Brun, A. S., Miesch, M., and Toomre, J. 2015. Grand Minima and Equatorward Propagation in a Cycling Stellar Convective Dynamo. *Astrophys. J.*, **809**(Aug.), 149.

Babcock, H.W. 1961. The Topology of the Sun's Magnetic Field and the 22-Year Cycle. *Astrophys. J.*, **133**, 572–589.

Baumann, I., Schmitt, D., Schüssler, M., and Solanki, S. 2004. Evolution of the large-scale magnetic field on the solar surface: a parameter study. *Astron. Astrophys.*, **426**, 1075–1091.

Beaudoin, P., Simard, C., Cossette, J.-F., and Charbonneau, P. 2016. Double Dynamo Signatures in a Global MHD Simulation and Mean-field Dynamos. *Astrophys. J.*, **826**(Aug.), 138.

Belvedere, Gaetano, Kuzanyan, Kirill M., and Sokoloff, Dmitry. 2000. A two-dimensional asymptotic solution for a dynamo wave in the light of the solar internal rotation. *Mon. Not. Roy. Astron. Soc.*, **315**(4), 778–790.

Berger, Mitchell A. 1999. Introduction to magnetic helicity. *Plasma Physics and Controlled Fusion*, **41**(12B), B167–B175.

Brandenburg, A. 2005. The Case for a Distributed Solar Dynamo Shaped by Near-Surface Shear. *Astrophys. J.*, **625**, 539–547.

Brandenburg, A., and Subramanian, K. 2005. Astrophysical magnetic fields and nonlinear dynamo theory. *Phys. Rep.*, **417**, 1–209.

Brandenburg, A., Rädler, K.-H., Rheinhardt, M., and Subramanian, K. 2008. Magnetic Quenching of α and Diffusivity Tensors in Helical Turbulence. *Astrophys. J. Lett.*, **687**, L49–L52.

Brandenburg, A., Candelaresi, S., and Chatterjee, P. 2009. Small-scale magnetic helicity losses from a mean-field dynamo. *Mon. Not. Roy. Astron. Soc.*, **398**(Sept.), 1414–1422.

Brandenburg, Axel, and Sokoloff, Dmitry. 2002. Local and Nonlocal Magnetic Diffusion and Alpha-Effect Tensors in Shear Flow Turbulence. *Geophysical and Astrophysical Fluid Dynamics*, **96**(4), 319–344.

Brown, T. M., Christensen-Dalsgaard, J., Dziembowski, W. A., Goode, P., Gough, D. O., and Morrow, C. A. 1989. Inferring the sun's internal angular velocity from observed p-mode frequency splittings. *Astrophys. J.*, **343**(Aug.), 526–546.

Browning, M.K., Miesch, M.S., Brun, A.S., and Toomre, J. 2006. Dynamo Action in the Solar Convection Zone and Tachocline: Pumping and Organization of Toroidal Fields. *Astrophys. J. Lett.*, **648**, L157–L160.

Bushby, P.J. 2006. Zonal flows and grand minima in a solar dynamo model. *Mon. Not. R. Astron. Soc.*, **371**, 772–780.

Caligari, P., Moreno-Insertis, F., and Schüssler, M. 1995. Emerging flux tubes in the solar convection zone. I. Asymmetry, tilt, and emergence latitudes. *Astrophys. J.*, **441**, 886–902.

Charbonneau, P. 2014. Solar Dynamo Theory. *Ann. Rev. Astron. Astrophys.*, **52**(Aug.), 251–290.

Charbonneau, P., and Barlet, G. 2011. The dynamo basis of solar cycle precursor schemes. *Journal of Atmospheric and Solar-Terrestrial Physics*, **73**(Feb.), 198–206.

Charbonneau, P., and Dikpati, M. 2000. Stochastic Fluctuations in a Babcock-Leighton Model of the Solar Cycle. *Astrophys. J.*, **543**(Nov.), 1027–1043.

Charbonneau, P., St-Jean, C., and Zacharias, P. 2005. Fluctuations in Babcock-Leighton Dynamos. I. Period Doubling and Transition to Chaos. *Astrophys. J.*, **619**(Jan.), 613–622.

Charbonneau, Paul. 2013 (Jan). *Solar and Stellar Dynamos*. Saas-Fee Advanced Course.

Charbonneau, Paul. 2020. Dynamo models of the solar cycle. *Living Reviews in Solar Physics*, **17**(1), 4.

Chatterjee, P., Nandy, D., and Choudhuri, A. R. 2004. Full-sphere simulations of a circulation-dominated solar dynamo: Exploring the parity issue. *Astron. Astrophys.*, **427**(Dec.), 1019–1030.

Chatterjee, P., Mitra, D., Rheinhardt, M., and Brandenburg, A. 2011. Alpha effect due to buoyancy instability of a magnetic layer. *Astron. Astrophys.*, **534**(Oct.), A46.

Chen, Feng, Rempel, Matthias, and Fan, Yuhong. 2017. Emergence of Magnetic Flux Generated in a Solar Convective Dynamo. I. The Formation of Sunspots and Active Regions, and The Origin of Their Asymmetries. *Astrophys. J.*, **846**(2), 149.

Choudhuri, A. R. 1992. Stochastic fluctuations of the solar dynamo. *Astron. Astrophys.*, **253**(Jan.), 277–285.

Choudhuri, A. R., and Gilman, P. A. 1987. The influence of the Coriolis force on flux tubes rising through the solar convection zone. *Astrophys. J.*, **316**(May), 788–800.

Choudhuri, A. R., and Karak, B. B. 2012. Origin of Grand Minima in Sunspot Cycles. *Physical Review Letters*, **109**(17), 171103.

Choudhuri, A. R., Schüssler, M., and Dikpati, M. 1995. The solar dynamo with meridional circulation. *Astron. Astrophys.*, **303**(Nov.), L29.

Choudhuri, Arnab Rai. 1998. *The physics of fluids and plasmas : an introduction for astrophysicists /*.

Christensen-Dalsgaard, J. 2002. Helioseismology. *Rev. Mod. Phys.*, **74**, 1073–1129.

Davidson, P.A. 2001. *An Introduction to Magnetohydrodynamics*. Cambridge Texts in Applied Mathematics. Cambridge; New York: Cambridge University Press.

DeVore, C. R., Boris, J. P., and Sheeley, N. R., Jr. 1984. The concentration of the large-scale solar magnetic field by a meridional surface flow. *Solar Phys.*, **92**(1-2), 1–14.

Dikpati, M., and Charbonneau, P. 1999. A Babcock-Leighton Flux Transport Dynamo with Solar-like Differential Rotation. *Astrophys. J.*, **518**(June), 508–520.

Dikpati, M., and Gilman, P.A. 2001. Flux-Transport Dynamos with α-Effect from Global Instability of Tachocline Differential Rotation: A Solution for Magnetic Parity Selection in the Sun. *Astrophys. J.*, **559**, 428–442.

Dikpati, Mausumi, and Gilman, Peter A. 2009. Flux-Transport Solar Dynamos. *Space Sci. Rev.*, **144**(1-4), 67–75.

Dikpati, Mausumi, Corbard, Thierry, Thompson, Michael J., and Gilman, Peter A. 2002. Flux Transport Solar Dynamos with Near-Surface Radial Shear. *Astrophys. J. Lett.*, **575**(1), L41–L45.

D'Silva, S., and Choudhuri, A.R. 1993. A theoretical model for tilts of bipolar magnetic regions. *Astron. Astrophys.*, **272**, 621–633.

Duarte, L. D. V., Wicht, J., Browning, M. K., and Gastine, T. 2016. Helicity inversion in spherical convection as a means for equatorward dynamo wave propagation. *Mon. Not. Roy. Astron. Soc.*, **456**(Feb.), 1708–1722.

Dubé, Caroline, and Charbonneau, Paul. 2013. Stellar Dynamos and Cycles from Numerical Simulations of Convection. *Astrophys. J.*, **775**(1), 69.

Durney, B. R. 1995. On a Babcock-Leighton dynamo model with a deep-seated generating layer for the toroidal magnetic field. *Solar Phys.*, **160**(Sept.), 213–235.

Durney, B. R. 1996. On a Babcock-Leighton Dynamo Model with a Deep-Seated Generating Layer for the Toroidal Magnetic Field, II. *Solar Phys.*, **166**(July), 231–260.

Durney, B. R. 1997. On a Babcock-Leighton Solar Dynamo Model with a Deep-seated Generating Layer for the Toroidal Magnetic Field. IV. *Astrophys. J.*, **486**(Sept.), 1065–1077.

Dziembowski, W. A., Goode, Philip R., and Libbrecht, K. G. 1989. The Radial Gradient in the Sun's Rotation. *Astrophys. J. Lett.*, **337**(Feb.), L53.

Fan, Y., and Fang, F. 2014. A Simulation of Convective Dynamo in the Solar Convective Envelope: Maintenance of the Solar-like Differential Rotation and Emerging Flux. *Astrophys. J.*, **789**(July), 35.

Fan, Y., and Fisher, G. H. 1996. Radiative Heating and the Buoyant Rise of Magnetic Flux Tubes in the Solar interior. *Solar Phys.*, **166**(1), 17–41.

Fan, Y., Fisher, G.H., and Deluca, E.E. 1993. The origin of morphological asymmetries in bipolar active regions. *Astrophys. J.*, **405**, 390–401.

Fan, Yuhong. 2021. Magnetic fields in the solar convection zone. *Living Reviews in Solar Physics*, **18**(1), 5.

Featherstone, N. A., and Miesch, M. S. 2015. Meridional Circulation in Solar and Stellar Convection Zones. *Astrophys. J.*, **804**(May), 67.

Ferriz-Mas, A., Schmitt, D., and Schüssler, M. 1994. A dynamo effect due to instability of magnetic flux tubes. *Astron. Astrophys.*, **289**, 949–956.

Fisher, G. H., Fan, Y., and Howard, R. F. 1995. Comparisons between Theory and Observation of Active Region Tilts. *Astrophys. J.*, **438**(Jan.), 463.

Gilman, P. A. 1983. Dynamically consistent nonlinear dynamos driven by convection in a rotating spherical shell. II - Dynamos with cycles and strong feedbacks. *Astrophys. J. Suppl.*, **53**(Oct.), 243–268.

Gizon, L. 2004. Helioseismology of Time-Varying Flows Through The Solar Cycle. *Solar Phys.*, **224**, 217–228.

Gizon, Laurent, Cameron, Robert H., Pourabdian, Majid, Liang, Zhi-Chao, Fournier, Damien, Birch, Aaron C., and Hanson, Chris S. 2020. Meridional flow in the Sun's convection zone is a single cell in each hemisphere. *Science*, **368**(6498), 1469–1472.

Glatzmaier, G. A. 1984. Numerical simulations of stellar convective dynamos. I - The model and method. *Journal of Computational Physics*, **55**(Sept.), 461–484.

Glatzmaier, G.A. 1985. Numerical simulations of stellar convective dynamos. II. Field propagation in the convection zone. *Astrophys. J.*, **291**, 300–307.

Goedbloed, J. P. Hans, and Poedts, Stefaan. 2004. *Principles of Magnetohydrodynamics*.

Guerrero, G., and de Gouveia Dal Pino, E. M. 2008. Turbulent magnetic pumping in a Babcock-Leighton solar dynamo model. *Astron. Astrophys.*, **485**(1), 267–273.

Guerrero, G., Smolarkiewicz, P. K., de Gouveia Dal Pino, E. M., Kosovichev, A. G., and Mansour, N. N. 2016. On the Role of Tachoclines in Solar and Stellar Dynamos. *Astrophys. J.*, **819**(Mar.), 104.

Guerrero, G., Zaire, B., Smolarkiewicz, P. K., de Gouveia Dal Pino, E. M., Kosovichev, A. G., and Mansour, N. N. 2019. What Sets the Magnetic Field Strength and Cycle Period in Solar-type Stars? *Astrophys. J.*, **880**(1), 6.

Hale, G. E., Ellerman, F., Nicholson, S. B., and Joy, A. H. 1919. The Magnetic Polarity of Sun-Spots. *Astrophys. J.*, **49**(Apr.), 153.

Hazra, G., Choudhuri, A. R., and Miesch, M. S. 2017. A Theoretical Study of the Build-up of the Suns Polar Magnetic Field by using a 3D Kinematic Dynamo Model. *Astrophys. J.*, **835**(Jan.), 39.

Hazra, Soumitra, and Nandy, Dibyendu. 2016. A Proposed Paradigm for Solar Cycle Dynamics Mediated via Turbulent Pumping of Magnetic Flux in Babcock-Leighton-type Solar Dynamos. *Astrophys. J.*, **832**(1), 9.

Hazra, Soumitra, and Nandy, Dibyendu. 2019. The origin of parity changes in the solar cycle. *Mon. Not. Roy. Astron. Soc.*, **489**(3), 4329–4337.

Hotta, H., and Iijima, H. 2020. On rising magnetic flux tube and formation of sunspots in a deep domain. *Mon. Not. Roy. Astron. Soc.*, **494**(2), 2523–2537.

Hotta, H., and Yokoyama, T. 2010. Importance of Surface Turbulent Diffusivity in the Solar Flux-Transport Dynamo. *Astrophys. J.*, **709**(Feb.), 1009–1017.

Hotta, H., Rempel, M., and Yokoyama, T. 2016. Large-scale magnetic fields at high Reynolds numbers in magnetohydrodynamic simulations. *Science*, **351**(Mar.), 1427–1430.

Howe, R. 2009. Solar Interior Rotation and its Variation. *Living Rev. Solar Phys.*, **6**.

Hoyng, P. 1988. Turbulent transport of magnetic fields. III. Stochastic excitation of global magnetic modes. *Astrophys. J.*, **332**, 857–871.

Hoyng, P. 1993. Helicity fluctuations in mean field theory: an explanation for the variability of the solar cycle? *Astron. Astrophys.*, **272**, 321–339.

Jha, Bibhuti Kumar, Karak, Bidya Binay, Mandal, Sudip, and Banerjee, Dipankar. 2020. Magnetic Field Dependence of Bipolar Magnetic Region Tilts on the Sun: Indication of Tilt Quenching. *Astrophys. J. Lett.*, **889**(1), L19.

Jiang, J., Chatterjee, P., and Choudhuri, A.R. 2007. Solar activity forecast with a dynamo model. *Mon. Not. R. Astron. Soc.*, **381**, 1527–1542.

Jiang, J., Cameron, R. H., Schmitt, D., and Işik, E. 2013. Modeling solar cycles 15 to 21 using a flux transport dynamo. *Astron. Astrophys.*, **553**(May), A128.

Jiang, J., Hathaway, D. H., Cameron, R. H., Solanki, S. K., Gizon, L., and Upton, L. 2014. Magnetic Flux Transport at the Solar Surface. *Space Sci. Rev.*, **186**(Dec.), 491–523.

Käpylä, P. J., Käpylä, M. J., Olspert, N., Warnecke, J., and Brandenburg, A. 2017. Convection-driven spherical shell dynamos at varying Prandtl numbers. *Astron. Astrophys.*, **599**(Mar.), A4.

Käpylä, P.J., Korpi, M.J., Ossendrijver, M., and Stix, M. 2006. Magnetoconvection and dynamo coefficients. III. α-effect and magnetic pumping in the rapid rotation regime. *Astron. Astrophys.*, **455**, 401–412.

Karak, B. B., and Choudhuri, A. R. 2012. Quenching of Meridional Circulation in Flux Transport Dynamo Models. *Solar Phys.*, **278**(May), 137–148.

Karak, B. B., and Nandy, D. 2012. Turbulent Pumping of Magnetic Flux Reduces Solar Cycle Memory and thus Impacts Predictability of the Sun's Activity. *Astrophys. J. Lett.*, **761**(Dec.), L13.

Karak, B. B., Rheinhardt, M., Brandenburg, A., Käpylä, P. J., and Käpylä, M. J. 2014. Quenching and Anisotropy of Hydromagnetic Turbulent Transport. *Astrophys. J.*, **795**(Nov.), 16.

Karak, Bidya Binay, and Cameron, Robert. 2016. Babcock-Leighton Solar Dynamo: The Role of Downward Pumping and the Equatorward Propagation of Activity. *Astrophys. J.*, **832**(1), 94.

Karak, Bidya Binay, and Miesch, Mark. 2017. Solar Cycle Variability Induced by Tilt Angle Scatter in a Babcock-Leighton Solar Dynamo Model. *Astrophys. J.*, **847**(1), 69.

Kitchatinov, L. L., and Olemskoy, S. V. 2012. Solar Dynamo Model with Diamagnetic Pumping and Nonlocal α-Effect. *Solar Phys.*, **276**(Feb.), 3–17.

Kitchatinov, L. L., Mordvinov, A. V., and Nepomnyashchikh, A. A. 2018. Modelling variability of solar activity cycles. *Astron. Astrophys.*, **615**(July), A38.

Kitchatinov, L.L., and Rüdiger, G. 1993. Λ-effect and differential rotation in stellar convection zones. *Astron. Astrophys.*, **276**, 96–102.

Kitchatinov, L.L., Mazur, M.V., and Jardine, M. 2000. Magnetic field escape from a stellar convection zone and the dynamo-cycle period. *Astron. Astrophys.*, **359**, 531–538.

Krause, F., and Rädler, K.-H. 1980. *Mean-Field Magnetohydrodynamics and Dynamo Theory*. Oxford; New York: Pergamon Press.

Küker, M., Arlt, R., and Rüdiger, R. 1999. The Maunder minimum as due to magnetic Λ-quenching. *Astron. Astrophys.*, **343**, 977–982.

Küker, M., Rüdiger, G., and Schulz, M. 2001. Circulation-dominated solar shell dynamo models with positive alpha effect. *Astron. Astrophys.*, **374**, 301–308.

Kumar, Rohit, Jouve, Laurène, and Nandy, Dibyendu. 2019. A 3D kinematic Babcock Leighton solar dynamo model sustained by dynamic magnetic buoyancy and flux transport processes. *Astron. Astrophys.*, **623**(Mar.), A54.

Leighton, R.B. 1964. Transport of magnetic fields on the sun. *Astrophys. J.*, **140**, 1547–1562.

Leighton, R.B. 1969. A magneto-kinematic model of the solar cycle. *Astrophys. J.*, **156**, 1–26.

Lemerle, A., and Charbonneau, P. 2017. A Coupled 2×2D Babcock-Leighton Solar Dynamo Model. II. Reference Dynamo Solutions. *Astrophys. J.*, **834**(Jan.), 133.

Lemerle, A., Charbonneau, P., and Carignan-Dugas, A. 2015. A Coupled 2×2D Babcock-Leighton Solar Dynamo Model. I. Surface Magnetic Flux Evolution. *Astrophys. J.*, **810**(Sept.), 78.

Lerche, I., and Parker, E.N. 1972. The Generation of Magnetic Fields in Astrophysical Bodies. IX. A Solar Dynamo Based on Horizontal Shear. *Astrophys. J.*, **176**, 213.

Mackay, Duncan H., and Yeates, Anthony R. 2012. The Sun's Global Photospheric and Coronal Magnetic Fields: Observations and Models. *Living Reviews in Solar Physics*, **9**(1), 6.

Masada, Y., Yamada, K., and Kageyama, A. 2013. Effects of Penetrative Convection on Solar Dynamo. *Astrophys. J.*, **778**(Nov.), 11.

McClintock, B. H., and Norton, A. A. 2013. Recovering Joy's Law as a Function of Solar Cycle, Hemisphere, and Longitude. *Solar Phys.*, **287**(Oct.), 215–227.

Miesch, M. S., and Dikpati, M. 2014. A Three-dimensional Babcock-Leighton Solar Dynamo Model. *Astrophys. J. Lett.*, **785**(Apr.), L8.

Miesch, M. S., and Teweldebirhan, K. 2016. A three-dimensional Babcock-Leighton solar dynamo model: Initial results with axisymmetric flows. *Advances in Space Research*, **58**(Oct.), 1571–1588.

Miesch, M.S., and Toomre, J. 2009. Turbulence, Magnetism, and Shear in Stellar Interiors. *Annual Review of Fluid Mechanics*, **41**, 317–345.

Mininni, P.D., and Gómez, D.O. 2002. Study of Stochastic Fluctuations in a Shell Dynamo. *Astrophys. J.*, **573**, 454–463.

Mininni, P.D., and Gómez, D.O. 2004. A new technique for comparing solar dynamo models and observations. *Astron. Astrophys.*, **426**, 1065–1073.

Moffatt, H.K. 1978. *Magnetic Field Generation in Electrically Conducting Fluids*. Cambridge Monographs on Mechanics and Applied Mathematics. Cambridge; New York: Cambridge University Press.

Moffatt, Keith, and Dormy, Emmanuel. 2019. *Self-Excited Fluid Dynamos*. Cambridge; New York: Cambridge University Press.

Moreno-Insertis, F. 1986. Nonlinear time-evolution of kink-unstable magnetic flux tubes in the convective zone of the sun. *Astrophys. J.*, **166**, 291–305.

Moss, D., Tuominen, I., and Brandenburg, A. 1990. Buoyancy-limited thin-shell dynamos. *Astron. Astrophys.*, **240**, 142–149.

Moss, D., Sokoloff, D., Usoskin, I., and Tutubalin, V. 2008. Solar Grand Minima and Random Fluctuations in Dynamo Parameters. *Solar Phys.*, **250**, 221–234.

Moss, David, and Brooke, John. 2000. Towards a model for the solar dynamo. *Mon. Not. Roy. Astron. Soc.*, **315**(3), 521–533.

Muñoz-Jaramillo, A., Nandy, D., Martens, P. C. H., and Yeates, A. R. 2010. A Double-ring Algorithm for Modeling Solar Active Regions: Unifying Kinematic Dynamo Models and Surface Flux-transport Simulations. *Astrophys. J. Lett.*, **720**(Sept.), L20–L25.

Nagy, M., Lemerle, A., Labonville, F., Petrovay, K., and Charbonneau, P. 2017. The Effect of "Rogue" Active Regions on the Solar Cycle. *Solar Phys.*, **292**(Nov.), 167.

Nandy, D., and Choudhuri, A.R. 2001. Toward a mean-field formulation of the Babcock–Leighton type solar dynamo. I. α-coefficient versus Durney's double-ring approach. *Astrophys. J.*, **551**, 576–585.

Nandy, D., and Choudhuri, A.R. 2002. Explaining the latitudinal distribution of sunspots with deep meridional flow. *Science*, **296**, 1671–1673.

Nelson, N. J., Brown, B. P., Brun, A. S., Miesch, M. S., and Toomre, J. 2013. Magnetic Wreaths and Cycles in Convective Dynamos. *Astrophys. J.*, **762**(Jan.), 73.

Nelson, N. J., Brown, B. P., Sacha Brun, A., Miesch, M. S., and Toomre, J. 2014. Buoyant Magnetic Loops Generated by Global Convective Dynamo Action. *Solar Phys.*, **289**(Feb.), 441–458.

Olemskoy, S. V., and Kitchatinov, L. L. 2013. Grand Minima and North-South Asymmetry of Solar Activity. *Astrophys. J.*, **777**(Nov.), 71.

Ossendrijver, A.J.H., Hoyng, P., and Schmitt, D. 1996. Stochastic excitation and memory of the solar dynamo. *Astron. Astrophys.*, **313**, 938–948.

Ossendrijver, M. 2003. The solar dynamo. *Astron. Astrophys. Rev.*, **11**, 287–367.

Ossendrijver, M.A.J.H. 2000. The dynamo effect of magnetic flux tubes. *Astron. Astrophys.*, **359**, 1205–1210.

Ossendrijver, M.A.J.H., and Hoyng, P. 1996. Stochastic and nonlinear fluctuations in a mean field dynamo. *Astron. Astrophys.*, **313**, 959–970.

Ossendrijver, M.A.J.H., Stix, M., and Brandenburg, A. 2001. Magnetoconvection and dynamo coefficients: dependence of the α-effect on rotation and magnetic fields. *Astron. Astrophys.*, **376**, 713–726.

Otmianowska-Mazur, K., Rüdiger, G., Elstner, D., and Arlt, R. 1997. The turbulent EMF as a time series and the 'quality' of dynamo cycles. *Geophys. Astrophys. Fluid Dyn.*, **86**, 229–247.

Parker, E. N. 1979. *Cosmical magnetic fields: Their origin and their activity.*

Parker, E.N. 1955. Hydromagnetic Dynamo Models. *Astrophys. J.*, **122**, 293–314.

Parker, E.N. 1975. The Generation of Magnetic Fields in Astrophysical Bodies. X. Magnetic Buoyancy and the Solar Dynamo. *Astrophys. J.*, **198**, 205–209.

Parker, Eugene N. 1955. The Formation of Sunspots from the Solar Toroidal Field. *Astrophys. J.*, **121**(Mar.), 491.

Passos, D., and Charbonneau, P. 2014. Characteristics of magnetic solar-like cycles in a 3D MHD simulation of solar convection. *Astron. Astrophys.*, **568**(Aug.), A113.

Petrovay, K., and Szakály, G. 1999. Transport effects in the evolution of the global solar magnetic field. *Solar Phys.*, **185**, 1–13.

Pevtsov, A. A., Berger, M. A., Nindos, A., Norton, A. A., and van Driel-Gesztelyi, L. 2014. Magnetic Helicity, Tilt, and Twist. *Space Sci. Rev.*, **186**(Dec.), 285–324.

Pipin, V. V., and Kosovichev, A. G. 2011a. Mean-field Solar Dynamo Models with a Strong Meridional Flow at the Bottom of the Convection Zone. *Astrophys. J.*, **738**(Sept.), 104.

Pipin, V. V., and Kosovichev, A. G. 2011b. The Subsurface-shear-shaped Solar $\alpha\Omega$ Dynamo. *Astrophys. J. Lett.*, **727**(2), L45.

Pipin, V. V., Sokoloff, D. D., and Usoskin, I. G. 2012. Variations of the solar cycle profile in a solar dynamo with fluctuating dynamo governing parameters. *Astron. Astrophys.*, **542**(June), A26.

Priest, Eric. 2014. *Magnetohydrodynamics of the Sun*.

Racine, É., Charbonneau, P., Ghizaru, M., Bouchat, A., and Smolarkiewicz, P. K. 2011. On the Mode of Dynamo Action in a Global Large-eddy Simulation of Solar Convection. *Astrophys. J.*, **735**(July), 46.

Rempel, Matthias. 2006. Flux-Transport Dynamos with Lorentz Force Feedback on Differential Rotation and Meridional Flow: Saturation Mechanism and Torsional Oscillations. *Astrophys. J.*, **647**(1), 662–675.

Roberts, P.H., and Stix, M. 1972. α-Effect Dynamos, by the Bullard-Gellman Formalism. *Astron. Astrophys.*, **18**, 453.

Rüdiger, G., and Hollerbach, R. 2004. *The magnetic universe : geophysical and astrophysical dynamo theory*.

Schrijver, C.J., and Siscoe, G.L. (eds). 2009. *Heliophysics: Plasma Physics of the Local Cosmos*. Cambridge: Cambridge University Press.

Schrijver, C.J., DeRosa, M.L., and Title, A.M. 2002. What Is Missing from Our Understanding of Long-Term Solar and Heliospheric Activity? *Astrophys. J.*, **577**, 1006–1012.

Schrinner, M., Rädler, K.-H., Schmitt, D., Rheinhardt, M., and Christensen, U. R. 2007. Mean-field concept and direct numerical simulations of rotating magnetoconvection and the geodynamo. *Geophysical and Astrophysical Fluid Dynamics*, **101**(Apr.), 81–116.

Sheeley Jr, N.R. 1991. Polar faculae: 1906–1990. *Astrophys. J.*, **374**, 386–389.

Simard, C., Charbonneau, P., and Dubé, C. 2016. Characterisation of the turbulent electromotive force and its magnetically-mediated quenching in a global EULAG-MHD simulation of solar convection. *Advances in Space Research*, **58**(Oct.), 1522–1537.

Simard, Corinne, and Charbonneau, Paul. 2020. Grand Minima in a spherical non-kinematic $\alpha^2\Omega$ mean-field dynamo model. *Journal of Space Weather and Space Climate*, **10**(Jan.), 9.

Simitev, R. D., Kosovichev, A. G., and Busse, F. H. 2015. Dynamo Effects Near the Transition from Solar to Anti-Solar Differential Rotation. *Astrophys. J.*, **810**(Sept.), 80.

Spiegel, E.A., and Zahn, J.-P. 1992. The solar tachocline. *Astron. Astrophys.*, **265**, 106–114.

Spruit, H.C. 1981. Equations for Thin Flux Tubes in Ideal MHD. *Astron. Astrophys.*, **102**, 129–133.

Stix, M. 1976. Differential Rotation and the Solar Dynamo. *Astron. Astrophys.*, **47**, 243–254.

Strugarek, A., Beaudoin, P., Charbonneau, P., and Brun, A. S. 2018. On the Sensitivity of Magnetic Cycles in Global Simulations of Solar-like Stars. *Astrophys. J.*, **863**(1), 35.

Thelen, J.-C. 2000. A mean electromotive force induced by magnetic buoyancy instabilities. *Mon. Not. R. Astron. Soc.*, **315**, 155–164.

Tobias, S. M., Weiss, N. O., and Kirk, V. 1995. Chaotically modulated stellar dynamos. *Mon. Not. Roy. Astron. Soc.*, **273**(Apr.), 1150–1166.

Ulrich, R. K., and Tran, Tham. 2013. The Global Solar Magnetic Field—Identification of Traveling, Long-lived Ripples. *Astrophys. J.*, **768**(2), 189.

Upton, L., and Hathaway, D. H. 2014. Predicting the Sun's Polar Magnetic Fields with a Surface Flux Transport Model. *Astrophys. J.*, **780**(Jan.), 5.

Upton, Lisa A., and Hathaway, David H. 2018. An Updated Solar Cycle 25 Prediction With AFT: The Modern Minimum. *Geophys. Res. Lett.*, **45**(16), 8091–8095.

van Ballegooijen, A.A., and Choudhuri, A.R. 1988. The possible role of meridional circulation in suppressing magnetic buoyancy. *Astrophys. J.*, **333**, 965–977.

Viviani, M., Käpylä, M. J., Warnecke, J., Käpylä, P. J., and Rheinhardt, M. 2019. Stellar Dynamos in the Transition Regime: Multiple Dynamo Modes and Antisolar Differential Rotation. *Astrophys. J.*, **886**(1), 21.

Wang, Y. M., and Sheeley, N. R., Jr. 1989. Average Properties of Bipolar Magnetic Regions during Sunspot CYCLE-21. *Solar Phys.*, **124**(1), 81–100.

Wang, Y.-M., and Sheeley Jr, N.R. 1991. Magnetic flux transport and the sun's dipole moment - New twists to the Babcock-Leighton model. *Astrophys. J.*, **375**, 761–770.

Wang, Y.-M., Nash, A.G., and Sheeley Jr, N.R. 1989. Magnetic flux transport on the sun. *Science*, **245**, 712–718.

Wang, Y.-M., Sheeley Jr, N.R., and Nash, A.G. 1991. A new cycle model including meridional circulation. *Astrophys. J.*, **383**, 431–442.

Warnecke, J., Käpylä, P. J., Käpylä, M. J., and Brandenburg, A. 2014. On The Cause of Solar-like Equatorward Migration in Global Convective Dynamo Simulations. *Astrophys. J. Lett.*, **796**(Nov.), L12.

Warnecke, J., Rheinhardt, M., Tuomisto, S., Käpylä, P. J., Käpylä, M. J., and Brand enburg, A. 2018. Turbulent transport coefficients in spherical wedge dynamo simulations of solar-like stars. *Astron. Astrophys.*, **609**(Jan), A51.

Weber, M. A., Fan, Y., and Miesch, M. S. 2013. Comparing Simulations of Rising Flux Tubes Through the Solar Convection Zone with Observations of Solar Active Regions: Constraining the Dynamo Field Strength. *Solar Phys.*, **287**(Oct.), 239–263.

Weber, Maria A., Fan, Yuhong, and Miesch, Mark S. 2011. The Rise of Active Region Flux Tubes in the Turbulent Solar Convective Envelope. *Astrophys. J.*, **741**(1), 11.

Weiss, N. O., and Tobias, S. M. 2016. Supermodulation of the Sun's magnetic activity: the effects of symmetry changes. *Mon. Not. Roy. Astron. Soc.*, **456**(Mar.), 2654–2661.

Whitbread, T., Yeates, A. R., and Muñoz-Jaramillo, A. 2019. The need for active region disconnection in 3D kinematic dynamo simulations. *Astron. Astrophys.*, **627**(July), A168.

Yeates, A. R., and Muñoz-Jaramillo, A. 2013. Kinematic active region formation in a three-dimensional solar dynamo model. *Mon. Not. Roy. Astron. Soc.*, **436**(Dec.), 3366–3379.

Yoshimura, H. 1975. Solar-cycle dynamo wave propagation. *Astrophys. J.*, **201**, 740–748.